UNIVERSIDADE DE LISBOA
FACULDADE DE CIÊNCIAS

Impact of the feeding cycle upon the neuronal membrane properties of rat hippocampal neurones: the involvement of voltage-gated sodium and calcium currents and the maintenance of plasma membrane organization.

"Documento Definitivo"

Doutoramento em Bioquímica

Especialidade de Biofísica Molecular

André Emanuel Pinheiro Bastos

Tese orientada por:

Doutor Pedro Afonso Lima
Doutor Rodrigo F.M. de Almeida
Doutora Ana Maria Sebastião

Documento especialmente elaborado para a obtenção do grau de doutor

2018

UNIVERSIDADE DE LISBOA

FACULDADE DE CIÊNCIAS

Impact of the feeding cycle upon the neuronal membrane properties of rat hippocampal neurones: the involvement of voltage-gated sodium and calcium currents and the maintenance of plasma membrane organization.

Doutoramento em Bioquímica

Especialidade de Biofísica Molecular

André Emanuel Pinheiro Bastos

Tese orientada por:

Doutor Pedro Afonso Lima
Doutor Rodrigo F.M. de Almeida
Doutora Ana Maria Sebastião

Júri:

Presidente:

- Doutora Amélia Pilar Grases dos Santos Silva Rauter, Professora Catedrática e Presidente do Departamento de Química e Bioquímica da Faculdade de Ciências da Universidade de Lisboa

Vogais:

- Doutor Euan Robert Brown, *Senior Lecture*
  School of Engineering and Physical Sciences da *Heriot Watt University* (Reino Unido);
- Doutor Albino Jorge Oliveira Maia, Professor Auxiliar Convidado
  Nova Medical School da Universidade Nova de Lisboa;
- Doutor Pedro Afonso dos Santos Baltazar de Lima
  Professor Auxiliar Convidado da Nova Medical School da Universidade Nova de Lisboa (Orientador);
- Doutora Ana Isabel Abrantes Coutinho, Professora Auxiliar
  Faculdade de Ciências da Universidade de Lisboa.

Documento especialmente elaborado para a obtenção do grau de doutor

Bolsa de doutoramento financiado pela Fundação para a Ciência e Tecnologia (FCT) com a referência SFRH/BD/881

2018

"If you're going to live life, you've got to be all in"

Professor Marian Diamond

"As long as our brain is a mystery, the universe, the reflection of the structure of the brain, will also be a mystery."

Santiago Ramón y Cajal

CONTENTS

Acknowledgments

Termina assim uma caminhada longa!... que começou a ser trilhada há quase 10 anos pelos protagonistas, Pedro e André. Decorria uma tarde do mês de Junho de 2008, terceiro semestre do 1º ano de mestrado em Bioquímica Médica, quando André recebeu um email de Pedro a confirmar a visita ao gabinete deste, a propósito de uma entrevista de estágio de mestrado. O tema do estágio era muito interessante, completamente fora dos conteúdos programáticos da FCUL naquela altura. Chegado ao gabinete de Pedro, André desde cedo percebeu que a dinâmica daquele professor era… diferente. O rumo formal que, pensara André, aquela entrevista tomaria, não passou de um momento ligeiro, de descontração, sem preconceitos, nem pretensiosismos. Com o tempo, André apercebeu-se que esta era uma capacidade inata de Pedro.

E foi assim que tudo começou!

Durante este longo trajecto de 10 anos conheci várias pessoas que me marcaram e me ajudaram muito para que hoje consiga estar a escrever a secção dos "agradecimentos" da minha tese de doutoramento. Chegou a hora de prestar louvores a quem os merece! A primeira palavra de gratidão é endereçada ao Pedro Lima. O respeito mútuo e a cumplicidade que se criou entre nós extravasa qualquer barreira profissional. Hoje sei que tenho um amigo no qual me posso apoiar e confiar. Pedro, obrigado por este caminho. Cresci muito durante este tempo. Tenho a plena noção que tu tiveste uma grande responsabilidade nisso. Obrigado!

A minha gratidão e reconhecimento estendem-se igualmente ao Rodrigo! Tenho bem presente a importância do teu papel na fase inicial da minha ainda curta carreira de investigador. Bem sei o que aquelas duas bolsas de investigação representaram no meu trajecto científico. Desde logo, foram preponderantes para ter conseguido uma bolsa de Doutoramento. Tenho plena consciência que tu foste essencial nessa fase pré-doutoramento. O teu contributo merece toda a minha consideração. Estas palavras são testemunhas disso mesmo!

Pedro e Rodrigo, evoluí muito convosco a nível técnico. Cada um de vocês, dentro das respectivas área de especialidade, soube passar-me conhecimentos que hoje ponho em

práctica no quotidiano da vida laboratorial. Se há dias em que trato a bancada do laboratório por 'tu', devo-os a vocês.

Seguidamente, o rol infindável de amigos e colegas de laboratório com os quais tive o prazer de aprender, ensinar e crescer. Joaquim Marquês!!!!! Este é para a vida! Já não escapa! Tem uma capacidade incrível; no laboratório consegue ser desconcertante e manter um elevado nível elevado de raciocínio, ao mesmo tempo. Fora do laboratório, continua a ser desconcertante… é um amigo, daqueles para a vida! IFI, caro Joaquim! IFI!

Inês Almeida, Ana, Andreia Giro, Filipa Santos, Catarina Antunes (!), Chico, Cordel, Telma, Eva, Ana Carreira, Telmo. A todos vocês um muito obrigado por, aqui e ali, me terem acompanhado neste projecto de doutoramento.

Ao pessoal da Sea4Us, a melhor empresa de biotecnologia do mundo e arredores! Tem sido fantástico acompanhar de perto o crescimento da empresa! O que suporta todo esse crescimento é a colaboração de cada uma das pessoas, que se identificam com a causa. Importa relevar a importância dos colegas com quem partilho ideias, experiências, gargalhadas, cafés, bebidas, jantares, conversas… é um prazer enorme ser testemunha do crescimento da Beatriz e da Rosa, por exemplo. Joaninha, Clarinha, Miguel, Gilberto, Sílvia, Marisa, Filipe, Nuno e, claro está, Pedro! A minha gratidão para com a Sea4Us também não será esquecida!

À minha noiva, minha companheira e confidente, Soraya! Esta grande realização pessoal ganha uma dimensão tendo-te por perto. Na verdade, se o caminho do meu projecto de doutoramento começou há 10 anos, o caminho do nosso projecto de vida começou há 14 anos! O Lourenço é a prova da vivacidade do nosso Amor. Tu tens sido uma companheira incrível, um apoio imprescindível! Tu, melhor que ninguém, sabes que o percurso até aqui foi duro, mas altamente recompensador. Só tu sabes todas as agruras por que passei, todos os percalços e desgaste de um percurso exigente e, muitas vezes, solitário. Estavas sempre lá para mais um beijo, para mais uma palavra de conforto e encorajamento. Pelo teu papel no meu doutoramento, e na minha vida em geral, muito obrigado!

List of abbreviations and symbols

a_f – amplitude coefficient of the fast component of inactivation

a_s amplitude coefficient of the slow component of inactivation

f_c – cut-off frequency

$\langle r \rangle$ -Fluorescence anisotropy

$\langle \tau \rangle$ -Fluorescence lifetime

$[Ca^{2+}_i]$ - intracellular calcium concentration

4-AP - 4-Aminopyridine

ACSF - chilled artificial cerebrospinal fluid

AGRP – Agouti-related protein

AIS – Initial Segmnt of Axons

AP – Action Potential

BCA - Bicinchoninic Acid

BDNF – Brain-Derived Neurotrophic Factor

C – current amplitude of the sustained component

CA - *cornu ammonis*

Ca^{2+} - Calcium

$CaCl_2$ – Calcium Chloride

Ca_v or VGCC- Voltage-Gated Calcium Channel

CCK – Cholecystokinin

$CHCl_3$ - chloroform

C_m - whole-cell capacitance (*Faraday, F*)

CNS – Central Nervous System

CO_2 – Carbone Dioxide

CsCl – Cesium Chloride

CsF – Cesium Fluoride

D.O.C – sodium deoxycholate

DHP - 1,4-dihydropyridine

DPH - 1,6-diphenyl-1,3,5-hexatriene

DPPE - 1,2-Dipalmitoyl-*sn*-glycero-3-phosphoethanolamine

DTT – dithiothreitol

E_{Na^+} - Reversal potential of Na^+ ions (mV)

$E_{Ca^{2+}}$ - Reversal potential of Ca^{2+} ions (mV)

FA – Fatty acid

G – Conductance (*Siemens, S*))

G/G_{max} - Conductance normalized to maximum conductance values

GI – Gastrointestinal

GLP-1 – Glucagon-like Peptide-1

GSL – glycosphingolipid

H.M. – patient Henry Molaison

h_∞ - steady-state of inactivation curves

HCl – chloride acid

H-H – Hodgkin and Huxley

HVA – High-threshold Voltage Activated

Hz – Heartz (frequency)

I/I_{max} – Current normalized to maximum value

I_{Ca} – Voltage-gated Ca^{2+} currents (*Ampere, A*)

IFM – Isoleucine; Phenylalanine; Methionine

I_{Na} – Voltage-gated Na^+ currents (*Ampere, A*)

I_p – Current flowing through the pipette

I_{peak} – Current amplitude taken at the peak of the current taces

$I_{sustained}$ - Current amplitude taken at the end of the voltage command pulse

I-V – Current to voltage relationship

K^+ - Potassium

KCl – Potassium chloride

KH_2PO_4 – Potassium Hydrogen Phosphate

l_d – liquid disordered phase

l_o – liquid ordered phase

LTD- Long-Term Depression

LTP – Long-Term Potentiation

LVA – Low-threshold Voltage Activated

MeOH - methanol

$MgCl_2$ – Magnesium Chloride

Na^+ - Sodium

NaCl – Sodium Chloride

$NaHCO_3$ – Sodium Hydrogen Carbonate

NaOH – Sodium Hydroxide

NP-40 - nonidet P

NPY – Neuropeptide Y

O_2 – Oxygen

PA - phosphatidic acid

pA/pF – Current amplitude normalized to cell capacitance

PC – Phosphatidylcholine

PE – Phosphatidylethanolamine

PI – Phosphatidylinositol

PIP – Phosphatidyl Inositol Phosphate

PIPES – 1,4-Piperazinediethanesulfonic acid

PL - Phospholipid

PM – Plasma Membrane

POMC – Pro-Opiomelanocortin

POPC - 1-Palmitoyl-2-oleoyl-*sn*-glycero-3-phosphocholine

ppIMI – postprandial intermeal interval

PS – Phosphatidylserine

PSM - N-palmitoyl-sphingomyelin

PVDF – Polyvinylidene difluoride (western blotting membrane)

PYY – Peptide YY (gut hormone)

R_f – Feedback resistor (*Ohm, Ω*)

R_s - Series resistance (*Ohm, Ω*)

SDS – Sodium Sodecyl Sulphate

SL – Sphingolipid

SM – Sphingomyelin

s_o – solid ordered

STX – Saxitoxin

TBS – Tris-buffered saline

TEA-Cl - Tetraethylammonium chloride

TLC – Thin-Layer Chromatography

Tm- Phase transition temperature

t-PnA - *Trans*-parinaric acid

t_r – Rise time

TTX – Tetrodotoxin

VC – voltage clamp

$V_{command}$ or V_{ref} – Voltage command

VGSC or Na_v – Voltage-Gated Sodium Channel

V_h – Half-maximal activation (or inactivation) potential (mV)

vHPC – Ventral hippocampus

V_m – Step command potential (mV).

V_{out} – Output voltage

V_p – Pipette voltage

V_s – Slope factor (mV/*e*-fold)

WC – Whole-cell

WD – Western diets

τ_h - Time-constant of inactivation (ms)

τ_{hfast} - Time-constant of the fast component of inactivation

τ_{hslow} – time-constant of the slow component of inactivation

Abstract

Feeding behaviour and energy balance is regulated by the central nervous system, through a concerted endeavour of different brain areas. The hippocampus, historically regarded as a substrate for learning and memory processes, has also been implicated in such energy regulation. In recent years, researchers have established that hippocampal neurones form a memory of a meal and act to delay meal initiation during the postprandial period. However, more experiments are needed to identify the processes involved in such control. The present thesis starts to fill this gap, by identifying possible neuronal mechanisms by which the hippocampus processes satiety and meal termination. By assessing the functioning of ion currents/channels and the lipid composition and organization of the plasma membrane throughout the feeding cycle, this study furnishes a global perspective of the effect of post-prandial and fasting conditions upon intrinsic neuronal plasma membrane (PM) properties.

The involvement of ion channels of rat hippocampal CA1 neurones in a feeding cycle context has already been studied. Indeed, the feeding cycle was found to impact the excitability of these neurones by modulating the activity of voltage-gated potassium currents. This finding has urged further investigation to evaluate the broadness of the effect of feeding cycle on the activity of other ion channels. Hence, it was critical to address the involvement of a) voltage-gated sodium (Na^+) currents/channels, given their importance in the initiation and propagation of action potentials, and b) voltage-gated calcium (Ca^{2+}) currents/channels, as they mediate the influx of this ubiquitous second messenger, with wide-ranging physiological roles, into the interior of the neurones.

The influence of feeding cycle on the biophysics of Na^+ and Ca^{2+} channels was undertaken in neurones acutely isolated from the CA1 subfield of the rat hippocampus. Two classes of neurones were used: those obtained from animals that fasted overnight (‘fasted neurones’) and those from animals that, after such period, were fed (‘fed neurones’).

Voltage-gated Na^+ currents were recorded by applying electrophysiological voltage clamp techniques - namely whole-cell (WC) and excised inside-out patches. Fed neurones, in comparison to fasted neurones, showed increased mean maximum macroscopic Na^+ current density ($1.5 \pm 0.12 mA.cm^{-2}$ *vs.* $1 \pm 0.10 mA.cm^{-2}$) and a greater

single-channel conductance (16.7 ± 0.76pS *vs.* 12.6 ± 1.30pS). Furthermore, the larger amplitude of the 'window current' obtained in fed neurones, derived from hyperpolarized activation curves and depolarized steady-state of inactivation curves (h_∞), indicates a greater Na^+ channel availability to respond to activation. Such variation is supported by a higher concentration of $Na_v1.2$ isoform at the plasma membrane-enriched fractions of hippocampus of fed animals. Overall, the results indicate a variation in the biophysics and expression of voltage gated Na^+ channels of rat hippocampal CA1 neurones, pointing out that feeding cycle changes the neuronal excitability.

Voltage-gated Ca^{2+} currents were analysed with whole-cell recordings. It was observed heterogeneity in whole-cell Ca^{2+} currents, here sorted into three categories – 'A', 'B', and 'C' currents. The differential distribution of these currents between fed and fasted neurones determined significant alterations on the inactivation properties of Ca^{2+} currents. The increased values of the time-constant of inactivation - τ_h -, observed upon feeding, can be ascribed to a conspicuous slowly-inactivating current mainly assigned to fed neurones (current 'A'), as oppose to the fastest kinetics of inactivation, solely seen in fasted neurones (current 'C'). Furthermore, in fed neurones, a depolarizing shift of the most depolarized component (V_{h2}) of the voltage-dependence of h_∞ was observed, which indicates that fasted neurones inactivate at more negative membrane potentials. Altogether, these observations point to a facilitated entry of Ca^{2+} into the soma of fed neurones, which, ultimately, potentiates the Ca^{2+}-dependent intracellular events.

The observed influence of feeding cycle on the biophysical and molecular expression of voltage-gated Na^+ and Ca^{2+} channels did not have repercussions on the lipid environment of the PM. The plasma membrane-enriched fractions of rat hippocampus were labeled with molecular probes: 1,6-diphenyl-1,3,5-hexatriene (DPH) and *trans*-parinaric acid (*t*-PnA). By assessing the fluorescence properties of these probes, it was possible to study the molecular organization and lateral heterogeneity (in the membrane plane) of the lipid domains. Specifically, two types of fluorescence spectroscopy measurements were used, either in steady-state (anisotropy measurements) and time-resolved domains (fluorescence intensity decay). The molecular biophysics analysis indicated that the order and rigidity of the acyl chains of the phospholipids constituents of the PM is not altered during the feeding cycle. Furthermore, the proportion of the different lipid domains at the surface of the neuronal PM is identical between conditions, which clearly indicates that the lateral heterogeneity of such domains is similar throughout the feeding cycle. This

observation must be interpreted at a hydrophobic core level, where the *t*-Pna and DPH preferentially locate within the PM.

The lipid content of the plasma membrane of rat hippocampus also did not endure any variation during the feeding cycle. The ratios calculated for the total lipid, phospholipid and cholesterol content were identical between the membranes of fed and fasted animals.

The results concerning the molecular biophysics and biochemical characterization of the lipids imbedded in the neuronal plasma membrane indicate that neurones must have a shield mechanism to preserve their functional viability, regardless of the peripheral metabolic state.

In summary, the greater levels of neuronal excitability and the promotion of Ca^{2+} entry into the neurones upon feeding may imply a subsequent increase on neuronal synaptic performance. A positive relationship between feeding and higher levels of synaptic plasticity-related phenomena (formation and consolidation of memories) is suggested, which could help to explain the role of hippocampus on the regulation of energy intake, mainly due to its role on meal-related episodic memories. This work gives new insights into the function of hippocampus on energy homeostasis, by adding new elements to the equation, namely, voltage-gated Na^{+} and Ca^{2+} channels.

Keywords:
Feeding cycle; CA1 neurones; hippocampus; voltage-gated ion channels; Plasma membrane

Resumo

A regulação do comportamento alimentar e do balanço energético, isto é, a relação entre a energia consumida e despendida, por parte do sistema nervoso central tem por base uma acção concertada de diferentes áreas do cérebro. O hipocampo, classicamente considerado um substrato para os processos de aprendizagem e memória, tem vindo a ser implicado em fenómenos de homeostasia energética. O crescente interesse da comunidade científica em aprofundar o conhecimento acerca dos processos celulares subjacentes a esta nova função do hipocampo reflecte a importância do tema. Nos últimos anos, vários investigadores têm estudado a influência dos neurónios do hipocampo na formação de memórias relacionadas com a ingestão de alimentos. Os resultados apontam para uma relação directa entre a consciencialização da ingestão de alimentos durante uma refeição e o prolongamento do subsequente período pós-prandial, retardando o início da refeição seguinte. No entanto, mais investigação é necessária para identificar os processos envolvidos neste mecanismo. A presente tese contribui no sentido de começar a preencher esta lacuna, identificando possíveis mecanismos pelos quais os neurónios do hipocampo processam a saciedade após uma refeição. Os estudos do funcionamento dos canais iónicos dependentes da voltagem, e da composição e organização lipídica da membrana plasmática, fornecem uma perspectiva global do efeito do ciclo alimentar (períodos pós-prandal/jejum) nas propriedades biofísicas da membrana plasmática dos neurónios.

O envolvimento de canais iónicos num contexto de ciclo alimentar foi previamente estudado na região CA1 dos neurónios do hipocampo de rato. Na sequência deste estudo, descobriu-se que o ciclo alimentar tem impacto na excitabilidade dos neurónios, através da modulação da actividade das correntes de potássio dependentes da voltagem. Surgiu então a necessidade de avaliar a amplitude do efeito do ciclo alimentar sobre o funcionamento de outros canais iónicos, nomeadamente canais/correntes de sódio (Na^+) dependentes da voltagem e canais/correntes de cálcio (Ca^{2+}) dependentes da voltagem. Os primeiros, dada a sua importância no início e propagação dos potenciais de ação, e os segundos, uma vez que medeiam o fluxo do mensageiro intracelular, Ca^{2+}, com amplas funções fisiológicas, para o interior dos neurónios.

A influência do ciclo alimentar nas propriedades biofísicas das correntes de Na^+ e Ca^{2+} foi abordada em neurónios isolados da região CA1 do hipocampo de ratos. Duas classes

de neurónios foram utilizadas: os obtidos a partir de animais que jejuaram durante a noite (‘neurónios em jejum’) e os provenientes de animais que, após esse período, foram alimentados ('neurónios alimentados").

As correntes de sódio dependentes da voltagem foram medidas com recurso a técnicas de electrofisiologia de voltagem controlada. Duas configurações foram utilizadas: *whole-cell voltage clamp* e *inside-out patch*. Os neurónios alimentados mostraram, relativamente aos neurónios em jejum, um aumento na densidade de corrente máxima ($1.5 \pm 0.12 mA.cm^{-2}$ versus $1 \pm 0.10\ mA.cm^{-2}$) e uma maior condutância de cada canal iónico *single channel* ($16.7 \pm 0.76 pS$ vs $12.6 \pm 1.30 pS$). Além disso, a maior amplitude da *window current* dos neurónios alimentados, resultante de uma hiperpolarização das curvas de activação e de uma despolarização das curvas de inactivação em estado estacionário (h_∞), indica uma maior disponibilidade de canais para responder ao processo de activação. Essa variação é corroborada por uma maior concentração da isoforma $Na_v1.2$ ao nível da membrana plasmática de hipocampo de animais alimentados. Genericamente, os resultados indicam uma variação nas propriedades biofísicas e na expressão molecular das correntes/canais de Na^+ da região CA1 dos neurónios do hipocampo de rato, apontando para a existência de consequências do ciclo alimentar ao nível da excitabilidade neuronal.

As correntes de Ca^{2+} dependentes da voltagem foram analisadas através da técnica *whole-cell voltage clamp*. Observou-se heterogeneidade ao nível das correntes, aqui classificadas em três categorias - 'A', 'B' e 'C. A distribuição diferencial destas correntes entre os neurónios alimentados e em jejum determinou alterações significativas sobre as respectivas propriedades de inactivação. Os valores mais elevados da constante de tempo de inativação - τ_h -, observada em neurónios alimentados, podem ser fundamentalmente atribuídos à expressão de uma componente de inactivação lenta, principalmente detectada nos neurónios alimentados (corrente "A"). Por oposição, a ocorrência de uma componente com uma cinética de inactivação rápida cingiu-se a observações em neurónios em jejum (corrente 'C'), contribuindo largamente para valores de constante de tempo de inactivação mais reduzidos. Além disso, as curvas de inactivação em estado estacionário dos neurónios alimentados apresentam um desvio despolarizante da segunda componente (V_{h2}), o que indica que os neurónios em jejum inactivam a potenciais de membrana mais negativos. Em conjunto, estas observações apontam para uma promoção da entrada de

Ca^{2+} no corpo celular dos neurónios alimentados, o que, inevitavelmente, potencia os eventos bioquímicos intracelulares dependentes de Ca^{2+}.

A influência do ciclo alimentar sobre a expressão molecular e biofísica dos canais de Na^{+} e Ca^{2+} não mostraram ter repercussões sobre o ambiente lipídico da membrana plasmática. As fracções de hipocampo de rato enriquecidas com membrana plasmática foram marcadas com sondas moleculares: *1,6-difenil-hexatriene-1,3,5 (DPH)* e ácido *trans*-parinárico (*t*-Pna). Através da análise das propriedades de fluorescência destas sondas, foi possível estudar a organização molecular e heterogeneidade lateral (no plano da membrana) dos domínios lipídicos da membrana plasmática. Especificamente, dois tipos de medidas de espectroscopia de fluorescência foram utilizados, quer em estado estacionário (medições de anisotropia), quer resolvidas no tempo (medições de decaimento de intensidade de fluorescência). A análise da biofísica molecular indicou que a ordem e a rigidez das cadeias acilo dos fosfolípidos componentes da membrana plasmática não são alteradas durante o ciclo alimentar. Além disso, a proporção dos diferentes domínios lipídicos na superfície da membrana plasmática dos neurónios é idêntica entre as condições pós-prandial e jejum, o que indica claramente que a heterogeneidade lateral de tais domínios é semelhante durante todo o ciclo alimentar. Esta observação deve ter em conta a localização das sondas utilizadas no interior das membranas, isto é, na região hidrofóbica da bicamada lipídica. Portanto, os resultados aqui apresentados não permitem qualquer tipo de considerações acerca da influência do ciclo alimentar a um nível mais superficial da membrana.

O teor de lípidos da membrana plasmática do hipocampo de rato também não sofreu qualquer variação durante o ciclo alimentar. Os índices calculados para os lipídios totais, teor de colesterol e fosfolípidos foram idênticos entre as membranas de animais alimentados e animais em jejum.

Os resultados referentes à caracterização bioquímica e biofísica molecular dos lípidos constituintes da membrana plasmática indicam que os neurónios do hipocampo devem possuir um mecanismo de protecção para preservarem a sua viabilidade funcional, independentemente do estado metabólico periférico.

Em conclusão, os maiores níveis de excitabilidade neuronal e a promoção da entrada de Ca^{2+} nos neurónios após a ingestão de alimentos pode implicar um melhor desempenho das sinapses neuronais. É, portanto, sugerida uma relação positiva entre a alimentação e

níveis mais elevados de plasticidade sináptica (fenómenos relacionados a formação e consolidação de memórias), o que poderia ajudar a explicar o papel do hipocampo na regulação do comportamento alimentar, principalmente devido ao seu papel no processo de formação de memórias das refeições ingeridas. Este trabalho fornece novos dados acerca sobre a função do hipocampo na homeostase energética, adicionando novos elementos à equação, no caso, canais de Na^+ e Ca^{2+} dependentes da voltagem.

Os resultados ilustrados nesta tese ganham uma relevância translacional quando inseridos num contexto de doenças epidémicas relacionadas com distúrbios alimentares, tais como obesidade e diabetes. Estas condições patológicas são fruto de hábitos alimentares pouco saudáveis, associados a um estilo de vida sedentário. Numa sociedade altamente susceptível a desenvolver este tipo de doenças impõe-se o a identificação e estudo de determinantes moleculares que possam ajudar a inverter esta tendência.

Palavras-chave:

Comportamento alimentar; neurónios da região CA1; hipocampo; canais iónicos dependentes da voltagem; membrana plasmática

1 General Introduction

1.1 Brain and energy homeostasis: crosstalk brain *vs.* peripheral organs (brain-gut axis)

The act of eating is an everyday part of the human experience and represents an obvious component of energy homeostasis, whose modulation and balance are ensured by energy intake and energy expenditure. The tight regulation of these processes is of the utmost importance given that it enables us to keep body weight stable over the adult life, preventing diseases like obesity and diabetes that are becoming epidemic with contemporary life habits.

The brain acts as the main orchestrator of this homeostatic process, as the constant bidirectional communication between the brain and peripheral organs, such as the gastrointestinal (GI) tract and other relevant tissues (*i.e.*, adipose tissue, pancreas, and liver), ensures that the brain constantly perceives and responds accordingly to the energy status/needs of the body (Faulconbridge & Hayes, 2011; Rui, 2013).

The involvement of the brain as key player in the homeostatic regulation of feeding behavior was initially established by a series of degeneration studies performed in different regions of the hypothalamus. The destruction of the ventromedial hypothalamic nuclei (known as 'satiety' centres) induces hyperphagia, resulting in obesity, decreased activity, and neuroendocrine abnormalities (Hetherington & Ranson, 1940, 1942; Brobeck, 1946; Anand & Brobeck, 1951), whereas lesions in the lateral hypothalamus (known as 'feeding' centres) reduce food intake and eventually lead to starvation and death (Anand & Brobeck, 1951).

These studies established the anatomical basis for modern research of energy regulation and set the start of an era in which the hypothalamus has been regarded as the headquarters of the central nervous system homeostatic mechanism of feeding behaviour. Indeed, the discovery of a complex intrahypothalamic neuronal network and the interplay with peripheral organs endows the hypothalamus the energy balance regulation (Williams *et al.*, 2000; Leibowitz & Wortley, 2004; Stanley *et al.*, 2005; Morton *et al.*, 2006; Lutter & Nestler, 2009; Pang & Han, 2012; Coll & Yeo, 2013; Dietrich & Horvath, 2013).

The action of neuropeptides together with circulating hormones and nutrients upon different subsets of hypothalamic neurones contributes to the process of energy

homeostasis (see Figure 1.1). Briefly, the entry of nutrients in the small intestine stimulates the release of peptides (e.g., cholecystokinin (CCK)) which act as negative feedback signals ("satiety" signals) to reduce meal size and terminate feeding. The effectiveness of these signals is thought to be modulated by circulating adiposity hormones (e.g., leptin and insulin), which relay information about long-term peripheral energy levels to the brain. Thus, in a post-prandial/absorptive state, leptin suppresses food intake and stimulates metabolic processes to dissipate excessive energy stores (Williams *et al.*, 2000, 2001, 2004; Leibowitz & Wortley, 2004; Stanley *et al.*, 2005). In addition, ghrelin has been identified as a gastric peptide that functions as a physiological meal initiation or "hunger" cue. Hence, during fasting, in response to negative energy balance, ghrelin stimulates food intake and, subsequently, promotes energy storage (Berthoud, 2002; Stanley *et al.*, 2005; Lutter & Nestler, 2009).

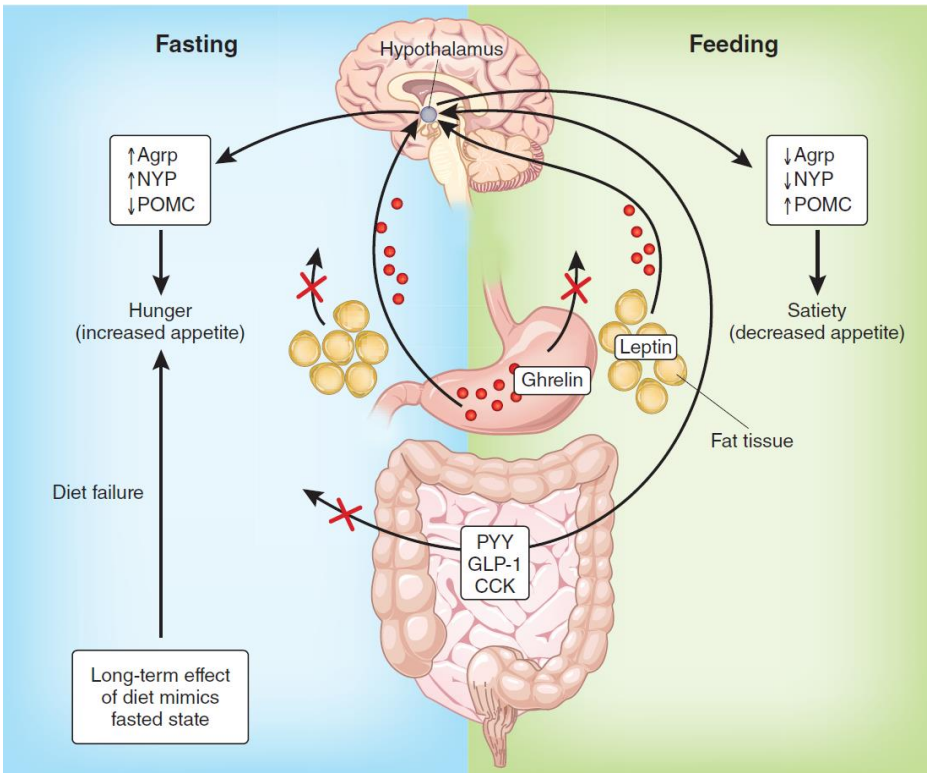

Figure 1.1- ***Hypothalamic control of food intake. The role of hormones and neuropeptides during feeding and fasting periods****. During and after regular feeding, there is a reduction in the production of ghrelin by the stomach. In contrast, production of Peptide YY (PYY), Glucagon Like Peptide-1(GLP-1) and CCK from the gut is increased, and serum leptin levels also rise. These changes are detected by the hypothalamus, resulting in modulation of gene expression of orexigenic (Agouti-related protein (AGRP) and neuropeptide Y (NPY)) and anorexigenic (pro-opiomelanocortin (POMC)) proteins, which result in decreased appetite and a feeling of satiety such that caloric intake is stopped. During fasting, decreased food intake suppresses the release of PYY, GLP-1 and CCK from the gut while stimulating the secretion of ghrelin by the stomach. Fasting also decreases serum leptin levels. These changes are detected by the hypothalamus, resulting in upregulation of orexigenic and downregulation of anorexigenic gene expression within the hypothalamus, leading to hunger. Taken from (Larder & O'Rahilly, 2012).*

Currently, it is established that extrahypothalamic central nervous system structures may play a previously unappreciated role in the control of ingestive behaviour, highlighting the broad reach of the hypothalamus in regulating energy balance. The hypothalamic 'center' hypothesis has dominated research on food intake during much of the last half century. However, with the advent of neuronal tracing, it became clear that the hypothalamus is well connected to most other areas of the brain and does not work in isolation (Berthoud, 2003). In addition, increasing evidence has shown that mammalian organisms rely on a much broader diversity and distribution of neuronal network, to regulate both energy intake and expenditure (Shin *et al.*, 2009; Grill & Hayes, 2012; Waterson & Horvath, 2015). Hence, it has become clear that the responsibility for controlling energy homeostasis is shared between several brain regions, spanning the range of 'higher' and 'lower' centres (from cortex to brainstem). Among them, the hippocampus, a forebrain structure historically conceived as an important substrate for memory storage and retrieval, has gained relevance as a hub of energy balance. A search in the literature reveals that hippocampus is neuroanatomically linked to hypothalamic nuclei and other brain circuits thought to underlie energy regulation (Atasoy *et al.*, 2012; Kanoski, 2012; Zeltser *et al.*, 2012; Davidson *et al.*, 2013; Sweeney & Yang, 2015, 2017; Berthoud *et al.*, 2017; Kanoski & Grill, 2017). Furthermore, hippocampal neurones integrate previous learned experience (episodic memories) with the external sensory context (visuospatial, olfactory, gustatory cues) and the internal context (interoceptive energy status cues – hunger, satiety, thirst) to influence decisions about when, where, what, and how much to eat (Davidson & Jarrard, 1993; Tracy *et al.*, 2001; Higgs, 2008; Davidson *et al.*, 2013; Parent *et al.*, 2014; Higgs, 2015).

1.2 Hippocampus and energy balance

The first glimpse of hippocampus as a possible regulator of food intake occurred in the early 1950s when neurosurgeons removed the hippocampus and other parts of the medial temporal region on both sides of the brain of an epileptic patient, known as H.M. (Henry Molaison) (Scoville & Milner, 1957). This experimental operation constitutes one of the most extensively studied human cases of the effects of hippocampal lesions. Accordingly, although the procedure brought H.M.'s seizures under control, it also produced a near complete loss of his ability to form new memories (Scoville & Milner, 1957). This was a major breakthrough in neuroscience as it helped to acknowledge the importance of the

hippocampus in brain activity, namely its role in memory and learning processes. Surprisingly, in addition to this memory impairment, it was noted by researchers (Hebben *et al.*, 1985) that H.M. rarely made any references to interoceptive states, such as hunger and thirst. This was the first time that hippocampus was thought to be interrelated with appetite. Since then, several reports were undertaken in patients with clinical cases disclosing hippocampal-dependent episodic memory deficits, like those of patient H.M. Likewise, they had difficulties determining whether they were sated, did not remember eating, and ate an additional meal when presented with food, even if they have just eaten to satiety (Hebben *et al.*, 1985; Higgs *et al.*, 2008; Francis & Stevenson, 2011; Parent *et al.*, 2014).

The cognitive regulation of food intake has gained momentum with the patient H.M. During the past 25 years, the scientific community has deepened the knowledge of the involvement of hippocampus in energy balance. In this context, one has to consider a number of evidence pinpointing the hippocampus as a structure responsible for energy regulation: a) throughout the hippocampus there is a multitude of receptors for preprandial and postprandial signals, such as leptin, insulin, ghrelin, glucose, cholecystokinin and feeding neuropeptides (Lathe, 2001; Beck & Pourié, 2013; Hsu *et al.*, 2015; Kanoski & Grill, 2017); b) It is known that hippocampal leptin negatively regulates feeding behaviour, ghrelin increases appetite (Volkow *et al.*, 2011; Beck & Pourié, 2013; Higgs, 2015; Kanoski & Grill, 2017), and both exert a direct action on hippocampal plasticity, contributing to learning and memory consolidation (Diano *et al.*, 2006; Beck & Pourié, 2013; Parent *et al.*, 2014); c) Accordingly, rats with selective lesions of the hippocampus exhibit reduced ability to use energy state cues (stomach distention, changes in circulating nutrient and hormone concentrations, etc.) as inhibitory signals (Davidson & Jarrard, 1993; Davidson *et al.*, 2005), resulting in increased appetitive response for food and weight gain (Davidson & Jarrard, 1993; Schmelzeis & Mittleman, 1996; Clifton *et al.*, 1998); d) hippocampal neurones are anatomically poised to monitor energy status and influence energy intake, as hippocampus integrates a neuronal circuitry that involves several regions of the brain (*e.g.*, hypothalamus) responsible for ingestive and appetitive behaviours. For example, the ventral hippocampus (vHPC), a medial temporal lobe structure with a prominent role in cognitive and emotional behaviours (Moser & Moser, 1998; Fanselow & Dong, 2010), is directly linked to hypothalamus (Cenquizca & Swanson, 2006); e) Human and rodent imaging studies show that the hippocampus is activated following food consumption (DelParigi *et*

al., 2004, 2005) and by experimental manipulations that mimic aspects of nutrient intake, including gastric distention and gastric electrical stimulation of the vagus nerve, the primary sensory channel of information communicated from the gastrointestinal tract to the brain (Wang *et al.*, 2006; Min *et al.*, 2011; Kanoski, 2012); f) hippocampal neurones may inhibit meal onset by extending the postprandial intermeal interval (ppIMI) (Henderson *et al.*, 2013; Parent *et al.*, 2014; Parent, 2016*a*; Hannapel *et al.*, 2017). This hypothesis is supported by the finding that increasing memory encoding during eating (brought by attention and awareness on eating) has a bigger effect on intake at the next eating episode than on current food intake (Higgs, 2002, 2008, 2015), and by the finding that episodic memory of the size of a previous meal, rather than the actual amount ingested, predicts hunger hours after the end of a meal (Parent, 2016*b*).

As a whole, these observations account for an influence of hippocampus in the adaptation of feeding behaviour to external (food-related stimuli) and internal (interoceptive signals) cues. Hence, in addition to its role in learning and memory, the hippocampus also performs multiple functions involved with the regulatory control of food intake. In this context, memory serves as a powerful mechanism for influencing eating behavior. In support of this idea, there is evidence that overweight and obesity are associated with learning and memory problems (Kanoski, 2012; Coppin *et al.*, 2014; Higgs, 2015; Prickett *et al.*, 2015). Concomitantly, understanding how cognitive processes, such as memory, control intake is vital important in nowadays society because it will provide a more complete explanation of how the brain controls eating and will likely provide insights regarding the brain mechanisms that contribute to eating disorders and diet-induced obesity.

In summary, the act of eating is directly influenced by the brain. The hippocampus is now viewed as a major player in this context. The opposite, *i*.e., the influence of feeding on hippocampal activity is equally important, as it is known that the hippocampal-dependent modulatory control of feeding behavior is compromised by consumption of foods common to 'Western diets' (WD), including saturated fats and simple carbohydrates.

Accordingly, the effects of nutrition upon hippocampal function is an emerging research area in the field of food-related diseases that affect several million people around the world (World Health Organization, 2018). Malfunctioning of hippocampus is linked to devastating consequences in energy intake, which, ultimately, contributes to complications in body weight regulation (Kanoski *et al.*, 2010; Kanoski & Davidson, 2011; Jacka *et al.*, 2015).

Hence, due to its fundamental importance, a historical perspective of the hippocampus, along with a description of the hippocampal circuitry and a characterization of the pyramidal neurones, can be found at the end of this thesis (Annex I).

1.3 Effect of nutrition on cognition

Diet, exercise and other aspects of our daily interaction with the environment have the potential to alter our brain health and mental function. Brain networks that are associated with the control of feeding are intimately associated with those that are involved in processing emotions, reward and cognition. In this respect, given its exquisite plasticity in response to multiple lifestyle factors or events, the hippocampus is a pivotal target to show effects of nutritional intervention (Monti *et al.*, 2014).

Several dietary components have been identified as having effects on cognitive abilities. Dietary factors can affect multiple brain processes by regulating neurotransmitter pathways, synaptic transmission, membrane fluidity and signal-transduction pathways (Gómez-pinilla, 2008). For example, Omega-3 polyunsaturated fatty acids, seminal constituents of cell membranes and essential for normal brain function, are involved in improvement and maintenance of mental health. A deficiency of omega-3 fatty acids results in impaired learning and memory (Gómez-pinilla, 2008; Stangl & Thuret, 2009; Francis & Stevenson, 2011; Kanoski & Davidson, 2011; Martin & Davidson, 2014; Monti *et al.*, 2014), and in humans has been associated with increased risk of several mental disorders, including attention-deficit disorder, dyslexia, dementia, depression, bipolar disorder and schizophrenia (Freeman *et al.*, 2006; Gómez-pinilla, 2008; Matsuoka *et al.*, 2017). On the other hand, dietary supplementation of omega-3 fatty acids has been found to elevate levels of hippocampal brain-derived neurotrophic factor (BDNF) (Wu *et al.*, 2004; Stangl & Thuret, 2009; Peters, 2011; Yeomans, 2017), a protein that serves to promote neurogenesis, synaptic transmission and memory performance.

In contrast to the health-promoting effects of diets rich in omega-3 fatty acids, epidemiological studies indicate that diets with high contents of saturated fats – 'western diet' (WD) - adversely affect cognition. This type of diet, common in societies with high obesity rates, is associated with the so-called "junk food" and its consumption can induce cognitive deficits and perturb hippocampal function (Kanoski *et al.*, 2010). The extended maintenance on a WD leads to neuroinflammation (Kanoski & Davidson, 2011; Hargrave

et al., 2016), reduced hippocampal and hypothalamic levels of BDNF, and smaller hippocampal volume (Jacka *et al.*, 2015). Overall, the pernicious effects of WD upon brain lead, directly or indirectly, to a hippocampal malfunction, which contributes to the commence or development of a vicious circle of hippocampal dysfunction and impaired inhibitory cognitive control of responding to environmental food cues, resulting in excess intake, obesity, and further hippocampal dysfunction (Figure 1.2) (Hargrave *et al.*, 2016; Berthoud *et al.*, 2017).

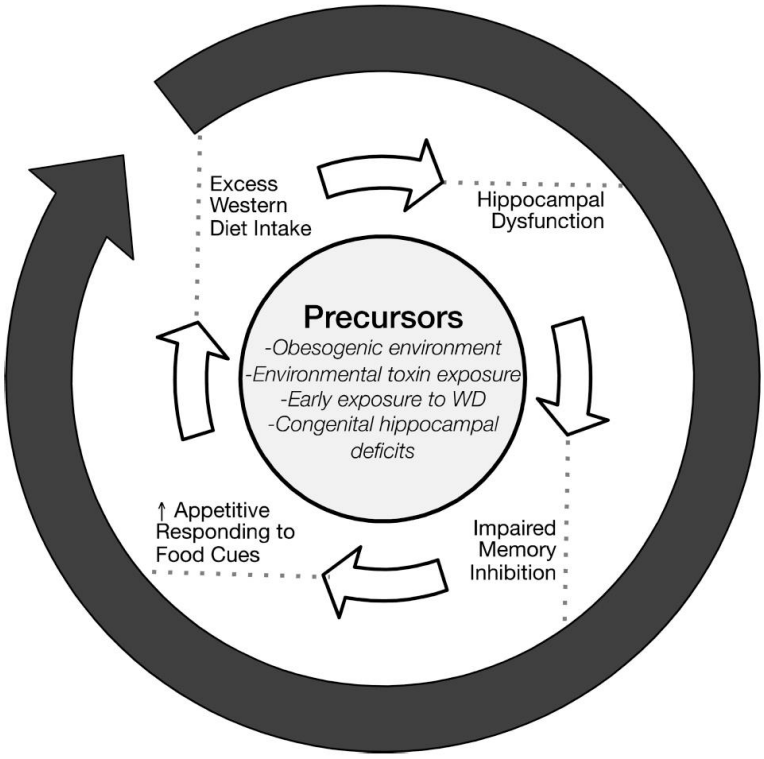

Figure 1.2- ***Vicious circle of overeating and hippocampal-based memory declined, induced by WD****. Taken from (Hargrave et al., 2016)*

The caloric intake, *per se*, also exerts a vital influence on cognition. Excess calories can increase the vulnerability of cells to damage (Mattson, 2005*a*) by causing free-radical formation, that decreases BDNF-mediated synaptic plasticity and cognitive function (Wu *et al.*, 2004). Moderate caloric restriction could thus protect the brain by reducing oxidative damage to cellular proteins, lipids and nucleic acids (Mattson, 2008). The number of calories seems to be a crucial factor for the physiological effects on human mental health, such that there are several nutritional studies that point a variety of low-calorie diets (e.g., fasting diets) as therapeutic applications to treat several neurological disorders, like Alzheimer´s disease and epilepsy (Mattson, 2005*a*; Bough & Rho, 2007; McNally & Hartman, 2012; Fond *et al.*, 2013; Longo & Mattson, 2014). Consequently,

the excessive food intake in wealthy nations seems to be almost as harmful as the lack of it in poor countries. It is intriguing that several countries with limited resources, such as India, have a reduced prevalence of neurological disorders that have been associated with diet, such as Alzheimer's disease (Gómez-pinilla, 2008).

The challenge now is to ameliorate our knowledge of the molecular mechanisms by which peripheral signals can modulate mental processes. Specifically, understanding the molecular basis of the effects of feeding on hippocampal neurones will help us to determine its consequence on cognition and subsequently on appetite.

1.4 Feeding cycle on hippocampal neurones - excitability and plasma membrane lipid composition and organization

Changes in metabolism – variations in glycogen content, as well as in levels of glycerol, free fatty acids and acetoacetate - will affect internal cellular biochemistry and one should therefore expect differences in the effects of preparations on isolated cells, tissues or organs removed from animals that have, or have not, been fasted (Smith, 2009). By all accounts, feeding cycle – postprandial and fasting periods - is characterized by tidal variations of biochemical processes, either in peripheral organs and in the brain, mainly due to glucose repletion or scarcity. For instance, the effect of fasting on brain metabolism and function is well described, namely its role in treating and preventing disease: the increased levels of glycerol and free fatty acids account for improvements in mood and cognition (Cunnane *et al.*, 2002; Fond *et al.*, 2013; Bazinet & Layé, 2014) and higher concentration of ketone bodies are thought to be involved in neuroprotection, as in mitigating the frequency of epilepsy seizures (Likhodii *et al.*, 2003; Bough & Rho, 2007; McNally & Hartman, 2012; Rho, 2017). In the hippocampus, fasting positively affects the production of BDNF, which itself promotes neurogenesis and consolidation of memory (Longo & Mattson, 2014).

To date, the extent of the effect of feeding cycle at a neuronal level is barely understood, especially in the hippocampus. A thorough literature search within this scope led to a study undertaken in rat dorsal hippocampal CA1 neurones, indicating that *Arc* expression, a marker of synaptic plasticity necessary for memory consolidation, was significantly higher in animals that consumed sucrose, than in control rats that had been given

comparable handling and transportation (Henderson *et al.*, 2016). This result suggests that consuming a meal should change the induction of synaptic plasticity in the dorsal hippocampal neurones responsible for the memory formation of a meal.

Synaptic plasticity is linked to intrinsic neuronal excitability, whose regulation is mediated by molecules present at the plasma membrane of neurones – the voltage-gated ion channels. For example, certain potassium (K^+) channels can change the induction thresholds and maintenance of Long-Term Potentiation (LTP) phenomena (Narasimhan, 2005; Kim & Hoffman, 2008). Thus, it is reasonable to expect that feeding may influence the behavior of the ion channels present at the surface of hippocampal CA1 neurones. Accordingly, there is a study showing that feeding cycle influences excitability in rat hippocampal CA1 neurones, by an indirect modulation of K^+ currents (Lima *et al.*, 2008). The effect of insulin on these ion channels is only detectable in fed animals, contrasting with the lack of response in fasted ones (Lima *et al.*, 2012). This clearly suggests a marked impact of feeding cycle periods over the activity of central nervous system neurones, particularly in protein ion channels involved in excitability (Figure 1.3).

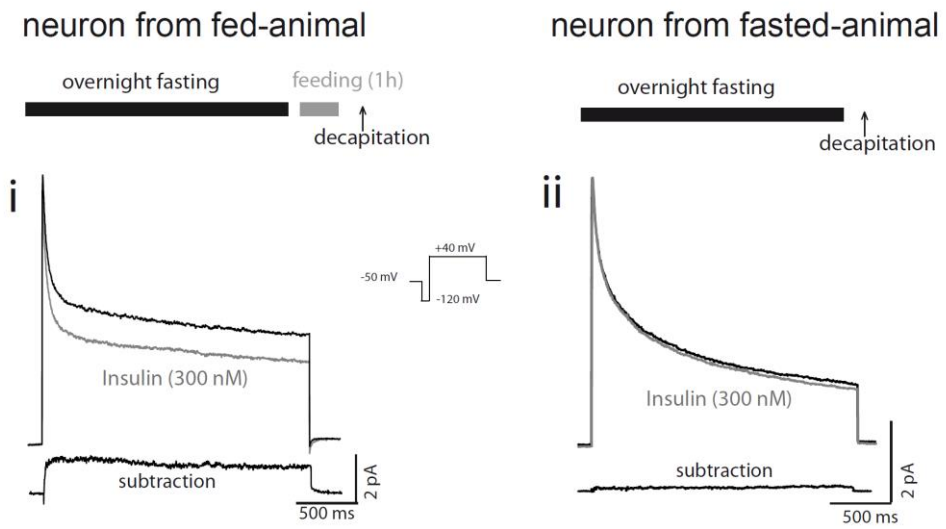

Figure 1.3 - ***Influence of feeding upon excitability of rat hippocampal CA1 neurones by mediating the effect of insulin over K^+ currents****. Adapted from (Lima et al., 2012).*

The excitability of the neurones also relies on the composition and organization of the lipid domains present in the plasma membrane. The ion channels, embedded in the phospholipid bilayer (Figure 1.4A), are mainly located in lipid microdomains known as 'lipid rafts', essentially constituted by cholesterol and sphingolipids. These lipid species

exert effects on channel activity either through direct protein–lipid interactions or by influencing the physical properties of the bilayer (Dart, 2010; Levitan *et al.*, 2010). Indeed, the regulation of the ion channels by the host bilayer lipid composition has been a subject of intense research. Currently, it is widely accepted that the ion channel function is most likely regulated by the bilayer elasticity, since the transition between the closed and the open states of an ion channel are accompanied by a deformation of the lipid bilayer in the vicinity of the membrane (Figure 1.4B) (Lundbæk *et al.*, 1996, 2004; Andersen & Koeppe, 2007; Lundbaek *et al.*, 2010).

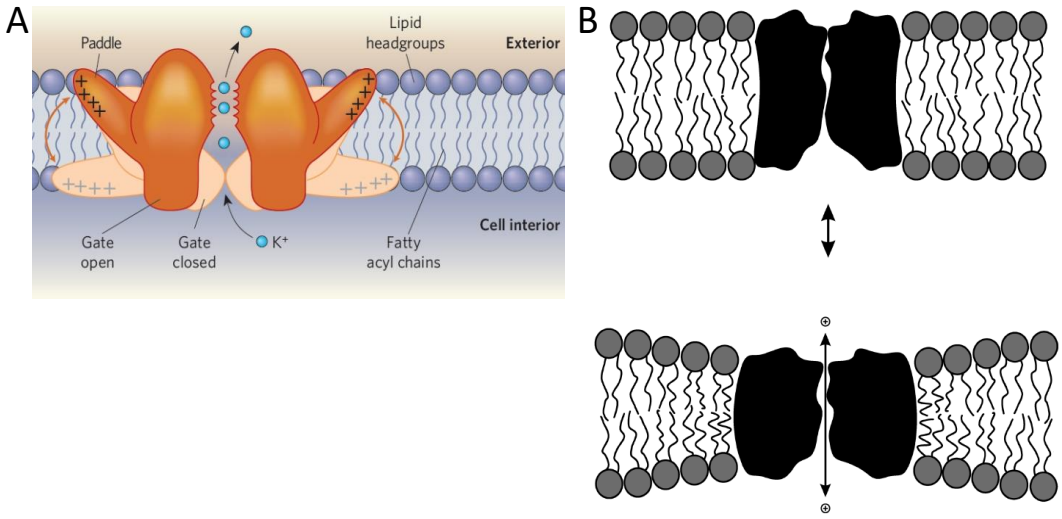

Figure 1.4- ***Interactions between ion channels and lipid composition of the plasma membrane****. A) Functioning of a voltage-gated potassium channel within the lipid bilayer, showing the transition between open and closed states. Taken from (Lee, 2006). B) The hydrophobic coupling between an ion channel and the surrounding bilayer means that a protein conformational change will be associated with a deformation of the surrounding bilayer. Adapted from (Lundbæk et al., 2004).*

The effects of peripheral metabolism and physiological feeding cycles upon the membrane-lipid dynamics are poorly understood, though. There is evidence that point to an influence of diet on the rigidity and organization of cellular membranes: dietary lipids, as cholesterol and Ω-3 polyunsaturated fatty acids, mediate variations on membrane fluidity, mainly by their effects over the lipid rafts (Mattson, 2005; Gómez-pinilla, 2008; Yaqoob, 2009).

Understanding the involvement of ion channels and membrane lipids composition and organization within the impact of feeding over the neuronal plasma membrane of hippocampus will 1) disclose new molecular clues into the involvement of hippocampus in the regulation of food intake and 2) leverage the state-of-the-art currently available

regarding the treatment and prevention of the food-related neurological diseases with marked impact on cognition. The present dissertation aims to contribute to this matter.

1.5 References

Anand BK & Brobeck JR (1951). Localization of a "Feeding Center" in the Hypothalamus of the Rat. *Proc Soc Exp Biol Med* **77,** 323–324.

Andersen OS & Koeppe RE (2007). Bilayer Thickness and Membrane Protein Function: An Energetic Perspective. *Annu Rev Biophys Biomol Struct* **36,** 107–130.

Bazinet RP & Layé S (2014). Polyunsaturated fatty acids and their metabolites in brain function and disease. *Nat Rev Neurosci* **15,** 771–785.

Beck B & Pourié G (2013). Ghrelin, neuropeptide Y, and other feeding-regulatory peptides active in the Hippocampus: Role in learning and memory. *Nutr Rev* **71,** 541–561.

Berthoud H-R (2002). Multiple neural systems controlling food intake and body weight. *Neurosci Biobehav Rev* **26,** 393–428.

Berthoud HR (2003). Neural systems controlling food intake and energy balance in the modern world. *Curr Opin Clin Nutr Metab Care* **6,** 615–620.

Berthoud HR, Münzberg H & Morrison CD (2017). Blaming the Brain for Obesity: Integration of Hedonic and Homeostatic Mechanisms. *Gastroenterology* **152,** 1728–1738.

Bough KJ & Rho JM (2007). Anticonvulsant mechanisms of the ketogenic diet. *Epilepsia* **48,** 43–58.

Brobeck JR (1946). Mechanism of the development of obesity in animals with hypothalamic lesions. *Physiol Rev* **26,** 541–559.

Cenquizca LA & Swanson LW (2006). Analysis of Direct Hippocampal Cortical Field CA1 Axonal Projections to Diencephalon in the Rat. *J Comp Neurol* **497,** 101–114.

Clifton PG, Vickers SP & Somerville EM (1998). Little and often: Ingestive behavior patterns following hippocampal lesions in rats. *Behav Neurosci* **112,** 502–511.

Coll AP & Yeo GSH (2013). The hypothalamus and metabolism: Integrating signals to control energy and glucose homeostasis. *Curr Opin Pharmacol* **13,** 970–976.

Coppin G, Nolan-Poupart S, Jones-Gotman M & Small DM (2014). Working memory

and reward association learning impairments in obesity. *Neuropsychologia* **65,** 146–155.

Cunnane SC, Musa K, Ryan M a, Whiting S & Fraser DD (2002). Potential role of polyunsaturates in seizure protection achieved with the ketogenic diet. *Prostaglandins Leukot Essent Fatty Acids* **67,** 131–135.

Dart C (2010). Lipid microdomains and the regulation of ion channel function. *J Physiol* **588,** 3169–3178.

Davidson T, Kanoski S, Walls E & Jarrard L (2005). Memory inhibition and energy regulation. *Physiol Behav* **86,** 731–746.

Davidson TL & Jarrard LE (1993). A role for hippocampus in the utilization of hunger signals. *Behav Neural Biol* **59,** 167–171.

Davidson TL, Kanoski SE, Schier LA, Clegg DJ & Benoit SC (2007). A Potential Role for the Hippocampus in Energy Intake and Body Weight Regulation. *Curr Opin Pharmacol* **7,** 613–616.

DelParigi A, Chen K, Salbe AD, Hill JO, Wing RR, Reiman EM & Tataranni PA (2004). Persistence of abnormal neural responses to a meal in postobese individuals. *Int J Obes* **28,** 370–377.

DelParigi A, Chen K, Salbe AD, Reiman EM & Tataranni PA (2005). Sensory experience of food and obesity: A positron emission tomography study of the brain regions affected by tasting a liquid meal after a prolonged fast. *Neuroimage* **24,** 436–443.

Fanselow M & Dong H-W (2010). Are the Dorsal and Ventral Hippocampus functionally distinct structures. *Neuron* **65,** 1–25.

Faulconbridge LF & Hayes MR (2011). Regulation of energy balance and body weight by the brain: A distributed system prone to disruption. *Psychiatr Clin North Am* **34,** 733–745.

Fond G, Macgregor A, Leboyer M & Michalsen A (2013). Fasting in mood disorders: Neurobiology and effectiveness. A review of the literature. *Psychiatry Res* **209,** 253–258.

Francis HM & Stevenson RJ (2011). Higher reported saturated fat and refined sugar

intake is associated with reduced hippocampal-dependent memory and sensitivity to interoceptive signals. *Behav Neurosci* **125,** 943–955.

Freeman MP, Davis JM, Keck PE, Mischoulon D, Hibbeln JR, Wisner KL, Richardson AJ, Peet M & Marangell LB (2006). Omega-3 fatty acids: evidence basis for treatment and future research in psychiatry. *J Clin Psychiatry* **67,** 1954–1967.

Gómez-pinilla F (2008). Brain foods: the effects of nutrients on brain function. *Nat Rev Neurosci*.

Grill HJ & Hayes MR (2012). Hindbrain neurones as an essential hub in the neuroanatomically distributed control of energy balance. *Cell Metab* **16,** 296–309.

Hannapel RC, Henderson YH, Nalloor R, Vazdarjanova A & Parent MB (2017). Ventral hippocampal neurones inhibit postprandial energy intake. *Hippocampus* **27,** 274–284.

Hargrave SL, Jones S & Davidson TL (2016). The Outward Spiral: A vicious cycle model of obesity and cognitive dysfunction. *Curr Opin Behav Sci* **9,** 40–46.

Hebben N, Corkin S, Eichenbaum H & Shedlack K (1985). Diminished ability to interpret and report internal states after bilateral medial temporal resection: case H.M. *Behav Neurosci* **99,** 1031–1039.

Henderson YO, Nalloor R, Vazdarjanova A & Parent MB (2016). Sweet orosensation induces Arc expression in dorsal hippocampal CA1 neurones in an Experience-dependent manner. *Hippocampus* **26,** 405–413.

Henderson YO, Smith GP & Parent MB (2013). Hippocampal neurones inhibit meal onset. *Hippocampus* **23,** 100–107.

Hetherington AW & Ranson SW (1940). Hypothalamic lesions and adiposity in the rat. *Anat Rec* **78,** 149–172.

Hetherington AW & Ranson SW (1942). The relation of various hypothalamic lesions to adiposity in the rat. *J Comp Neurol* **76,** 475–499.

Higgs S (2002). Memory for recent eating and its influence on subsequent food intake. *Appetite* **39,** 159–166.

Higgs S (2008). Cognitive influences on food intake: The effects of manipulating memory

for recent eating. *Physiol Behav* **94,** 734–739.

Higgs S (2015). Cognitive processing of food rewards. *Appetite* **104,** 10–17.

Higgs S, Williamson AC, Rotshtein P & Humphreys GW (2008). Sensory-Specific Satiety Is Intact in Amnesics Who Eat Multiple Meals. *Psychol Sci* **19,** 623–628.

Hsu TM, Hahn JD, Konanur VR, Noble EE, Suarez AN, Thai J, Nakamoto EM & Kanoski SE (2015). Hippocampus ghrelin signaling mediates appetite through lateral hypothalamic orexin pathways. *Elife* **4,** 1–20.

Jacka FN, Cherbuin N, Anstey KJ, Sachdev P & Butterworth P (2015). Western diet is associated with a smaller hippocampus: a longitudinal investigation. *BMC Med* **13,** 215.

Kanoski SE (2012). Cognitive and neuronal systems underlying obesity. *Physiol Behav* **106,** 337–344.

Kanoski SE & Davidson TL (2011). Western Diet Consumption and Cognitive Impairment: Links to Hippocampal Dysfunction and Obesity. *Physiol Behav* **103,** 59–68.

Kanoski SE & Grill HJ (2017). Hippocampus Contributions to Food Intake Control: Mnemonic, Neuroanatomical, and Endocrine Mechanisms. *Biol Psychiatry* **81,** 748–756.

Kanoski SE, Zhang Y, Zheng W & Davidson TL (2010). The Effects of a High-Energy Diet on Hippocampal Function and Blood-Brain Barrier Integrity in the Rat. *J Alzheimer´s Dis* **21,** 207–219.

Kim J & Hoffman DA (2008). Potassium Channels: Newly Found Players in Synaptic Plasticity. *Neuroscientist* **14,** 276–286.

Larder R & O'Rahilly S (2012). Shedding pounds after going under the knife: Guts over glory—why diets fail. *Nat Med* **18,** 666–667.

Lathe R (2001). Hormones and the hippocampus. *J Endocrinol* **169,** 205–231.

Lee AG (2006). Ion channels: A paddle in oil. *Nature* **444,** 697.

Leibowitz SF & Wortley KE (2004). *Hypothalamic control of energy balance: Different peptides, different functions*.

Levitan I, Fang Y, Rosenhouse-Dantsker A & Romanenko V (2010). Cholesterol and Ion Channels. *Subcell Biochem* **51,** 509–549.

Likhodii SS, Serbanescu I, Cortez MA, Murphy P, Snead OC & Burnham WM (2003). Anticonvulsant properties of acetone, a brain ketone elevated by the ketogenic diet. *Ann Neurol* **54,** 219–226.

Lima PA, Costa PC, Mondragão M, Alves FM, Costa G, Hardy D, Jalil A, Ogden D & Auger. C (2012). Metabolic states induced by feeding/fasting influence insulin-induced excitability and levels of insulin receptor in hippocampal but not cerebellar neurones. In *8 th FENS Forum of Neuroscience*.

Lima PA, Vicente MI, Alves FM, Dionísio JC & Costa PF (2008). Insulin increases excitability via a dose-dependent dual inhibition of voltage-activated K+ currents in differentiated N1E-115 neuroblastoma cells. *Eur J Neurosci* **27,** 2019–2032.

Longo VD & Mattson MP (2014). Fasting: Molecular Mechanisms and Clinical Applications. *Cell Metab* **19,** 181–192.

Lundbæk JA, Birn P, Girshman J, Hansen AJ & Andersen OS (1996). Membrane stiffness and channel function. *Biochemistry* **35,** 3825–3830.

Lundbæk JA, Birn P, Hansen AJ, Søgaard R, Nielsen C, Girshman J, Bruno MJ, Tape SE, Egebjerg J, Greathouse D V., Mattice GL, Koeppe RE & Andersen OS (2004). Regulation of Sodium Channel Function by Bilayer Elasticity. *J Gen Physiol* **123,** 599–621.

Lundbaek JA, Collingwood SA, Ingolfsson HI, Kapoor R & Andersen OS (2010). Lipid bilayer regulation of membrane protein function: gramicidin channels as molecular force probes. *J R Soc Interface* **7,** 373–395.

Lutter M & Nestler EJ (2009). Homeostatic and Hedonic Signals Interact in the Regulation of Food Intake. *J Nutr* **139,** 629–632.

Martin AA & Davidson TL (2014). Human cognitive function and the obesogenic environment. *Physiol Behav* **136,** 185–193.

Matsuoka YJ, Sawada N, Mimura M, Shikimoto R, Nozaki S, Hamazaki K, Uchitomi Y & Tsugane S (2017). Dietary fish, n-3 polyunsaturated fatty acid consumption, and depression risk in Japan: a population-based prospective cohort study. *Transl*

Psychiatry **7,** e1242.

Mattson MP (2005*a*). ENERGY INTAKE, MEAL FREQUENCY, AND HEALTH: A Neurobiological Perspective. *Annu Rev Nutr* **25,** 237–260.

Mattson MP (2005*b*). Dietary Modulation of Lipid Rafts. Implications for Disease Prevention and Treatment. In *Membrane Microdomain Signaling. Lipid Rafts in Biology and Medicine*, ed. Mattson MP, pp. 191–201. Humana Press.

Mattson MP (2008). Dietary factors, hormesis and health. *Ageing Res Rev* **7,** 43–48.

McNally MA & Hartman AL (2012). Ketone Bodies in Epilepsy. *J Neurochem* **121,** 28–35.

Min DK, Tuor UI & Chelikani PK (2011). Gastric distention induced functional magnetic resonance signal changes in the rodent brain. *Neuroscience* **179,** 151–158.

Monti JM, Baym CL & Cohen NJ (2014). Identifying and characterizing the effects of nutrition on hippocampal memory. *Adv Nutr* **5,** 337S–43S.

Moser MB & Moser EI (1998). Functional differentiation in the hippocampus. *Hippocampus* **8,** 608–619.

Narasimhan K (2005). SK channels: a new twist to synaptic plasticity. *Nat Neurosci* **8,** 550–550.

Parent MB (2016*a*). Dorsal Hippocampal–Dependent Episodic Memory Inhibits Eating. *Curr Dir Psychol Sci* **25,** 461–466.

Parent MB (2016*b*). Cognitive control of meal onset and meal size: Role of dorsal hippocampal-dependent episodic memory. *Physiol Behav* **162,** 112–119.

Parent MB, Darling JN & Henderson YO (2014). Remembering to eat: hippocampal regulation of meal onset. *Am J Physiol Regul Integr Comp Physiol* **306,** R701–R713.

Prickett C, Brennan L & Stolwyk R (2015). Examining the relationship between obesity and cognitive function: A systematic literature review. *Obes Res Clin Pract* **9,** 93–113.

Rho JM (2017). How does the ketogenic diet induce anti-seizure effects? *Neurosci Lett* **637,** 4–10.

Rui L (2013). Brain regulation of energy balance and body weight. *Rev Endocr Metab Disord* **14,** 387–407

Schmelzeis MC & Mittleman G (1996). The hippocampus and reward: effects of hippocampal lesions on progressive-ratio responding. *Behav Neurosci* **110,** 1049–1066.

Scoville WB & Milner B (1957). Loss of Recent Memory After Bilateral Hippocampal Lesions. *J Neurol Neurosurg Psychiatry* **20,** 11–21.

Shin AC, Zheng H & Berthoud H-R (2009). An expanded view of energy homeostasis: Neural integration of metabolic, cognitive, and emotional drives to eat. *Physiol Behav* **97,** 572–580.

Smith A (2009). *Fasting in rodents*.

Stangl D & Thuret S (2009). Impact of diet on adult hippocampal neurogenesis. *Genes Nutr* **4,** 271–282.

Stanley S, Wynne K, McGowan B & Bloom S (2005). Hormonal Regulation of Food Intake. *Physiol Rev* **85,** 1131–1158.

Sweeney P & Yang Y (2015). An excitatory ventral hippocampus to lateral septum circuit that suppresses feeding. *Nat Commun* **6,** 10188.

Sweeney P & Yang Y (2017). Neural Circuit Mechanisms Underlying Emotional Regulation of Homeostatic Feeding. *Trends Endocrinol Metab* **28,** 437–448.

Tracy AL, Jarrard LE & Davidson TL (2001). The hippocampus and motivation revisited: Appetite and activity. *Behav Brain Res* **127,** 13–23.

Volkow ND, Wang GJ & Baler RD (2011). Reward, dopamine and the control of food intake: implications for Obesity. *Trends Cogn Sci* **15,** 37–46.

Wang G-J, Yang J, Volkow ND, Telang F, Ma Y, Zhu W, Wong CT, Tomasi D, Thanos PK & Fowler JS (2006). Gastric stimulation in obese subjects activates the hippocampus and other regions involved in brain reward circuitry. *Proc Natl Acad Sci* **103,** 15641–15645.

Waterson MJ & Horvath TL (2015). Neuronal Regulation of Energy Homeostasis: Beyond the Hypothalamus and Feeding. *Cell Metab* **22,** 962–970.

Williams G, Bing C, Cai XJ, Harrold J a, King PJ & Liu XH (2001). The hypothalamus and the control of energy homeostasis. *Physiol Behav* **74,** 683–701.

Williams G, Cai XJ, Elliott JC & Harrold JA (2004). Anabolic neuropeptides. *Physiol Behav* **81,** 211–222.

Williams G, Harrold JA & Cutler DJ (2000). The hypothalamus and the regulation of energy homeostasis: lifting the lid on a black box. *Proc Nutr Soc* **59,** 385–396.

World Health Organization (2018). Obesity and overweight. *World Heal Organ*.

Wu A, Ying Z & Gomez-Pinilla F (2004). The interplay between oxidative stress and brain-derived neurotrophic factor modulates the outcome of a saturated fat diet on synaptic plasticity and cognition. *Eur J Neurosci* **19,** 1699–1707.

Yeomans MR (2017). Adverse effects of consuming high fat–sugar diets on cognition: implications for understanding obesity. *Proc Nutr Soc*1–11.

2 Objectives

The involvement of hippocampal neurones on the regulation of food intake has received close attention as evidence has been emerging for a key role of the hippocampus apart from the traditional function of supporting memory and learning processes. However, the molecular mechanisms by which hippocampal neurones play this new role is unclear. This thesis aimed at providing evidence on this regard, by studying the influence of feeding cycle over the neuronal activity. The lipid and protein alterations were established as benchmarks for the influence of peripheral metabolism in the hippocampal neurones. For such, rat hippocampal CA1 neurones and plasma membrane-enriched fractions of rat hippocampus were obtained from animals during fasting or during the post-prandial period.

Specifically, it was intended to:

1. Address the impact of feeding cycle on neuronal excitability, by recording the sodium (Na^+) and calcium (Ca^{2+}) currents mediated by voltage-gated Na^+ and Ca^{2+} channels at the plasma membrane of rat hippocampal CA1 neurones. Whole-cell voltage clamp and inside-out excised patch-clamp were used to study the behaviour of the ion channels. By investigating important biophysical properties, such as voltage-dependence of activation and inactivation, time-constant of inactivation and single-channel conductance, it was possible to report the influence of feeding cycle upon the activity of pyramidal CA1 neurones.
2. Identify whether feeding cycle influences the ion channel expression levels (Na^+ and/or Ca^{2+} channels) at the neuronal plasma membrane through western blotting experiments. The molecular expression of currents with significantly different whole-cell current density between fed and fasted neurones prioritized the choice of channel isoform studied in this task.
3. Establish differences in lipid composition of brain neuronal-membranes in the different conditioned rats (lipidomic studies). This allowed determining lipid level modifications in fed and fasting conditions.
4. Evaluate the implications of lipid alterations on the biophysical properties of the neuronal membrane, particularly in the amount and organization of lipid rafts.

2.1 Outline of the thesis

The following flowchart aims at guiding the readers throughout the thesis to facilitate the comprehension of the objectives outlined above. One can find a visual resume of the experimental design used as well as the organization of the results within the structure of the thesis.

INFLUENCE OF FEEDING CYCLE ON RAT HIPPOCAMPAL NEURONES

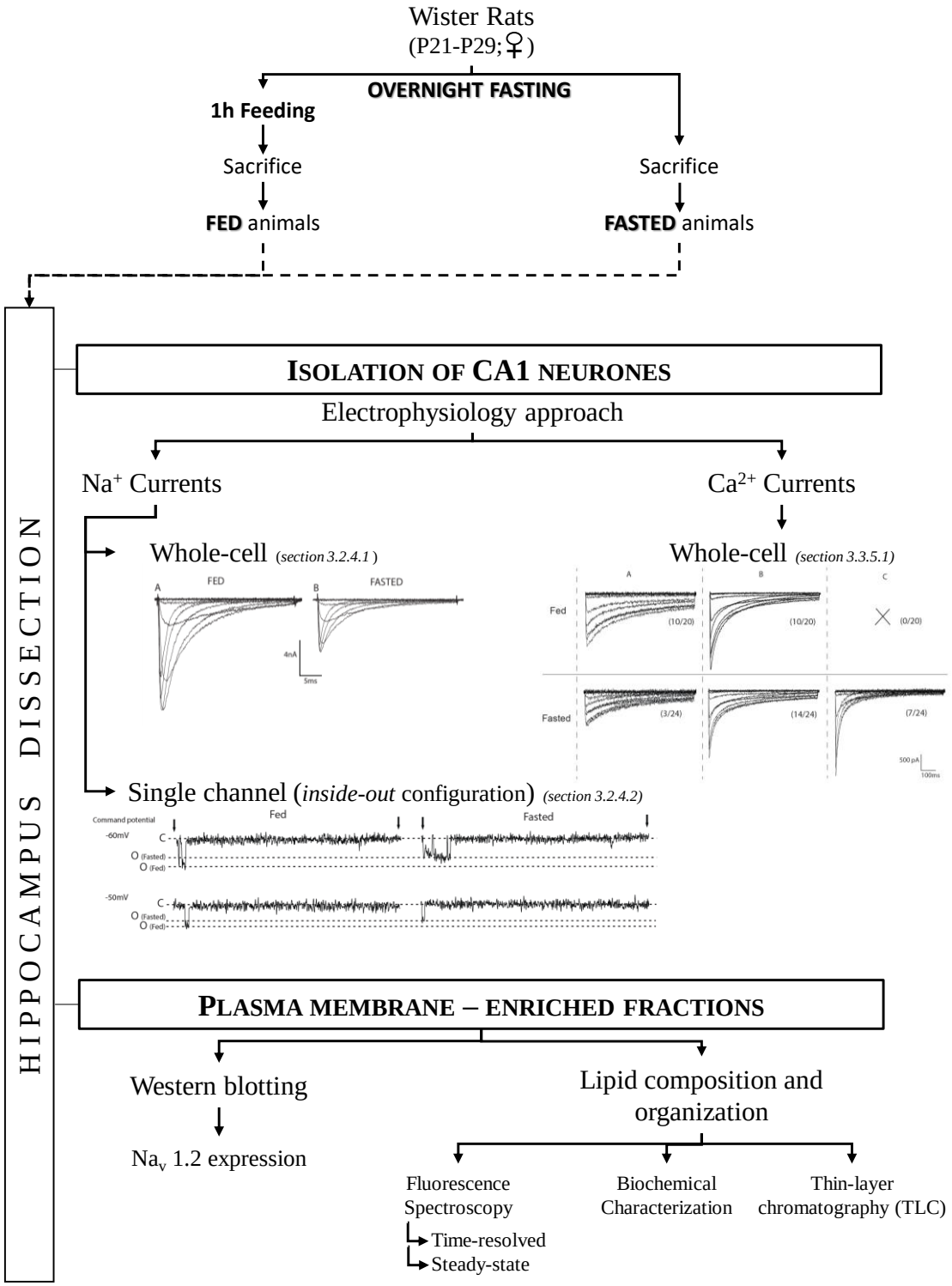

3 Feeding cycle on Ion channels

Feeding cycle was found to modulate the functioning of protein ion channels present at the surface of rat hippocampal CA1 neurones. This chapter discloses a thorough biophysical analysis of voltage-gated sodium (Na^+) and calcium (Ca^{2+}) currents. For a fully comprehension of the results depicted here, one may find, at the end of this thesis, an annex with the fundamentals of the electrophysiology techniques used (Annex II). The general methods applied to study the Na^+ and Ca^{2+} currents are firstly presented.

3.1 Material and Methods

3.1.1 Animal monitorization

Twenty-one- to twenty-nine-day old female Wistar rats (P21-29), purchased from Charles River Laboratories, were used according to Afonso and co-workers (Afonso *et al.*, 2012). Briefly, animals were maintained under a 12:12 h light⁄dark cycle with free access to food and water. On the day before the experiment, animals were subjected to an overnight fasting period, period in which the effect of food deprivation is greatest (Palou *et al.*, 1981), with the free access to water maintained. At the day of the experiment, animals were either fed during a period of 1 hour to ensure that they had eaten by the time the experiment started (here termed fed animals or 'fed neurones') or not fed (here termed fasted animals or 'fasted neurones').

The establishment of different metabolic conditions were ensured upon the measurement of glycaemia levels (mg/dL) using a glucose meter (Freestyle Lite, Blood Glucose Test, Abbot®), as follows: 121.17 ± 5.73 and 44.091 ± 2.46, for fed and fasted animals, respectively.

3.1.2 Dissection of hippocampus and preparation of CA1 hippocampal sub-slices

The animals were sacrificed by cervical dislocation. The brain was rapidly removed as follows: the dorsal skin of the head was cut and pulled back to expose the skull surface.

The skull overlying the brain was removed by cutting longitudinally along the sutures from the occipital bone until above the olfactory lobes and cutting transversely at the frontal suture. Care was taken to cut the dura mater. The exposed brain was lifted from the skull after sectioning out the olfactory bulb and the underlying cranial nerves and placed in chilled artificial cerebrospinal fluid (ACSF) containing (in mM): 125 NaCl, 25 $NaHCO_3$, 1.25 KCl, 1.25 KH_2PO_4, 1 $CaCl_2$, 1.5 $MgCl_2$ and 16 D-glucose, saturated with 95% O2 and 5% CO_2 (pH 7.4). Throughout the dissection, the brain tissue was maintained wet in the cold bicarbonate solution to minimise the damage from anoxia and improve the texture of the tissue for slicing (Schwartzkroin, 1981; Sakmann & Stuart, 1995).

Subsequently, the brain was placed over a cold damp surface and bisected along the longitudinal fissure to separate the hemispheres (Figure 3.1A). Each hemisphere was held down on its lateral convex side, and the thalamus and surrounding tissue overlying the hippocampus dissected aside (Figure 3.1B and 3.1C). The hippocampus was exposed and isolated (Figure 3.1D). From this point forward, two procedures were applied: dissociation of CA1 neurones (section 3.1.3) or fractionation of hippocampus tissue to obtain plasma membrane-enriched fractions (section 3.1.7).

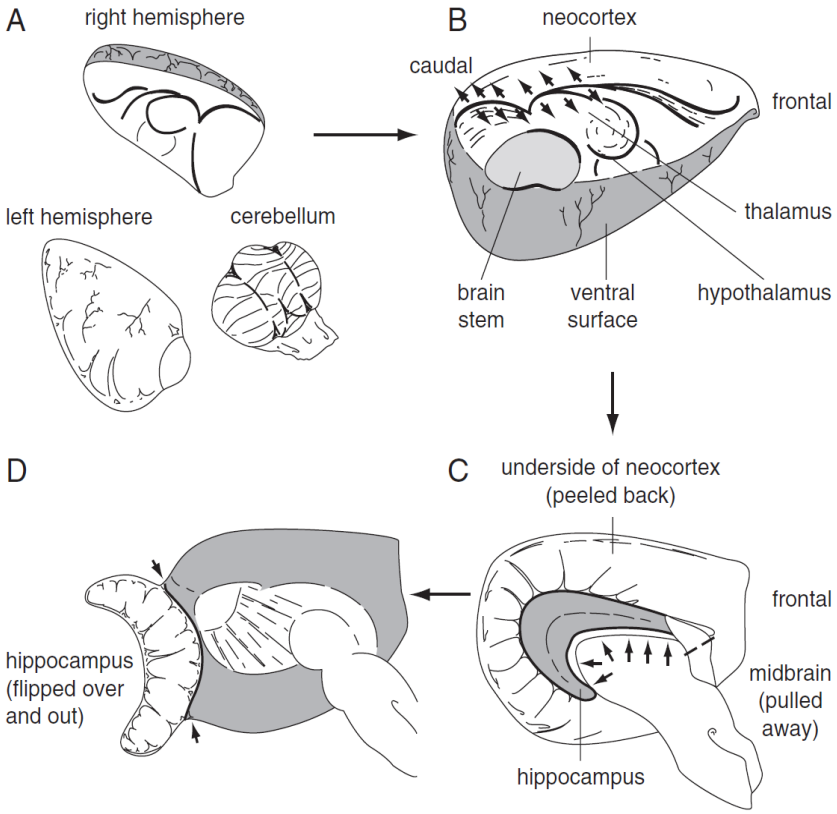

Figure 3.1- ***Dissection of the hippocampus****. (A) The cerebellum/brain stem is cut off and discarded. The cerebrum is bisected along the midline, separating the two hemispheres. (B) The left hemisphere is illustrated with the medial surface facing up. The neocortex is peeled off toward the caudal surface, and the midbrain is pulled ventrally by pulling in opposite directions at the location marked by the arrows using small Teflon-coated weighing spatulas. (C) The dentate surface of the hippocampus is revealed. Care should be taken not to touch the hippocampus with the spatulas. The fornix is cut by pushing the point of the spatula into the brain at the point indicated by the dotted line. Next, one spatula is inserted gently under the fimbria and further under the hippocampus (area of insertion indicated by the large arrows). This works best if the spatula is inserted starting at the caudal (temporal) end of the hippocampus and worked toward the septal end. (D) The hippocampus is flipped out of the brain by lifting and pushing on the spatula, and then rotating the spatula tip around the long axis of the hippocampus. Once the hippocampus is flipped out, it is trimmed at the line indicated by the two arrows, and the rest of the brain is pulled away from the isolated hippocampus. Taken from (Madison & Edson, 2001)*

3.1.3 Enzymatic and mechanical dissociation of CA1 neurones

The dissected hippocampi were placed on a soft rubber, on a drop of cold ACSF with the lateral face comprising the CA1 area upwards. The hippocampi were cut perpendicular to their longitudinal axis in the middle third region to obtain transverse slices, 300µM thick (Figure 3.2A). The slices were transferred with a brush to a petri dish with cold oxygenated ACSF. Sub-slices from the CA1 area were obtained by carefully making 3 incisions around the CA1 subfield. The cutting lines are indicated by dashes in Figure

3.2B. The viability of cells is highly dependent on the rapidity and accuracy of the dissection procedure.

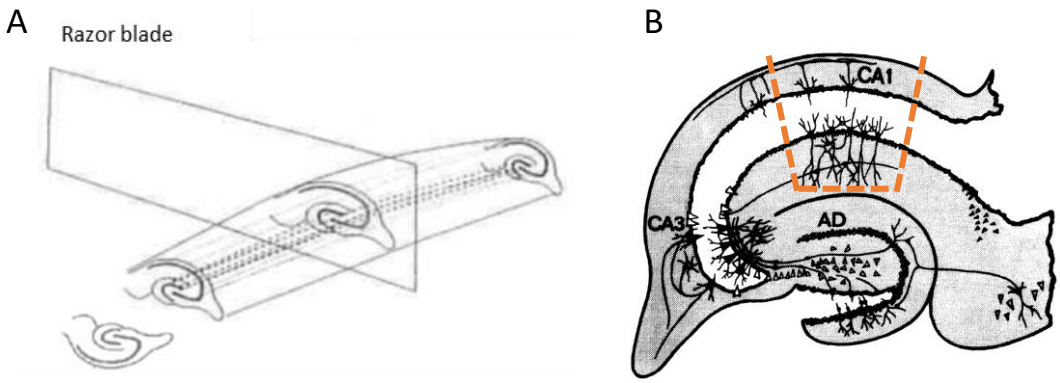

Figure 3.2- ***Preparation of rat hippocampal CA1 neurones****. A) The hippocampus lying with the CA1 area upwards is cut perpendicular to its long axis to yield transverse slices. Taken from (Chad* et al.*, 1991). B) Transversal axis of the rat hippocampus exposing the somata and proximal processes of the major cell body layers. The cutting lines performed around the CA1 subfield are highlighted. Taken from(Fisher et al., 1990).*

Sub-slices of the CA1 region were incubated at 32 °C in an oxygen saturated solution under moderate stirring; the composition of the incubating solution was as follows (in mM): NaCl 120, KCl 5, $CaCl_2$ 1, $MgCl_2$ 1, 1,4-Piperazinediethanesulfonic acid (PIPES) 20, D-Glucose 25, adjusted to pH 7 with 1 mM NaOH. Trypsin (Sigma Type XI, 0.9 mg/ml) was added to this solution shortly after the preparation of the sub-slices; incubation period was 30–50 min, depending on rat's age. Figure 3.3 shows a schematic diagram of the enzyme incubation system used.

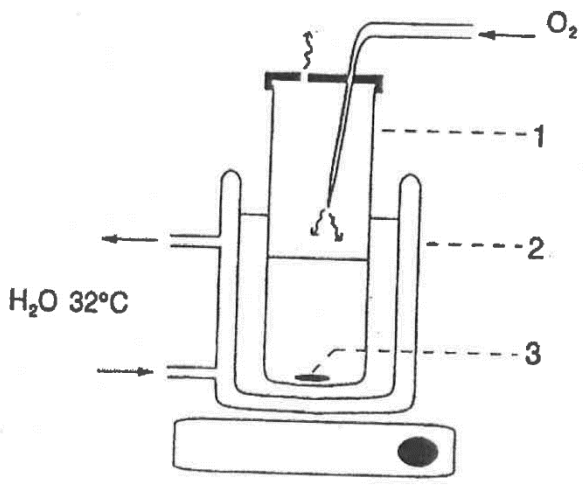

Figure 3.3- ***Schematic diagram of the enzyme incubation system****. The incubation beaker (1) contains the hippocampal tissue in a trypsin-dissociation solution. A circulating hot water heat-exchanger (2) keeps the temperature at 32ºC. The tissue is constantly agitated using a magnetic stirrer (3) and oxygenated through a tube blowing air to the surface of the solution. Taken from (Fernandes, 2002).*

The sub-slices were placed in an incubation beaker containing the dissociation solution and trypsin. They were agitated with a magnetic stirrer and oxygenated by blowing O_2 (medicinal grade) through a fine catheter tubing, adjusted above the liquid surface to avoid air bubbles. Temperature was maintained at 32ºC by a circulating hot water bath, heat-exchanging system. After digestion, sub-slices were transferred to an oxygen saturated enzyme-free solution after a brief wash with this solution and kept at room temperature at moderate stirring. The preparation remained viable for about 5–6 h. Enzyme activity was particularly critical for patch activity: too little enzyme activity often lead to the production of very few isolated neurones (clumping), whilst too many tended to produce many rounded, damaged neurones.

The mechanical dissociation involved gentle trituration of the enzyme-treated sub-slices using 4 flame-polished Pasteur pipettes, with gradual narrower tips (*i.e.*, tissue repeatedly washed back and forth through the pipette tip). The first trituration with a wider tip pipette achieved splitting of the tissue into two. Further trituration with narrower tips produced dispersion of individual neurones. The technique of mechanical dissociation involved some skill; too vigorous trituration often resulted in very few intact neurones or neurones with short dendrites. Freshly dissociated neurones were experimentally viable for up to two hours in the recording chamber at room temperature. In subsequent experiments further away from the digestion, the dissociated neurones were viable for a shorter time. The 35mm plastic Petri dishes were used as recording chambers for acutely isolated neurones. The recording chamber was placed on a metal platform set on the stage of an inverted microscope. The microscope was standing on an anti-vibration table and enclosed by a Faraday cage.

3.1.4 Selection of neurones/criteria of exclusion

Patch pipettes were positioned over the soma of cells, whose selection was based on their shape and appearance: pyramidal or fusiform cell shapes (cell body length about 20-40microns) attached to the floor of the petri dish with shinny smooth surfaces and no visible nucleus under ordinary inverted microscope optics (Olympus CK2 microscope) were preferred, the latter conditions being an indication of viability (Kay & Wong, 1986). Criteria to accept a well voltage-clamped cell were based on the pattern of current arousal (Sah *et al.*, 1988; Costa *et al.*, 1994): on applying depolarizing series of command pulses

to the membrane, currents were evoked progressively; current records showed no delay in respect to the beginning of the command pulse and rose smoothly; current breakthrough or discontinuities were not apparent in the current to voltage (*I-V)* curves. Cells that did not comply with the above criteria were discarded.

3.1.5 Whole-cell recordings

Cells were superfused (2-3 mL/min) with an extracellular solution adequate for the recording of whole-cell inward currents. The composition of external and internal solutions used to record sodium and calcium currents are disclosed in Table 3.1, along with notes explaining the rationale behind the use of some constituents.

Table 3.1- Composition of solutions used for recording whole-cell sodium and calcium currents of rat hippocampal CA1 neurones

Composition of solutions used in Whole-cell voltage clamp recordings							
	I_{Na}				I_{Ca}		
	External (bath solution)	mM	Internal (filling solution)	mM	External (bath solution)	mM	Internal (filling solution)	mM
	NaCl	100	NaCl	10	$CaCl_2$	5	$CaCl_2$	0,5
	KCl	5	CsF[d]	140	CsCl	5	CsF[d]	100
	HEPES	10	HEPES	10	HEPES	10	HEPES	10
	$CaCl_2$	1,8	EGTA	5	TEA-Cl[a]	135	TEA-Cl[a]	20
	$MgCl_2$	1			$MgCl_2$	1	$MgCl_2$	2
	Tetraethylammonium chloride (TEA-Cl)[a]	30			Glucose	25	EGTA	10
	4-amino-pyridine (4-AP)[b]	3			4-AP[a]	5	MgATP[f]	2
	$CoCl_2$[c]	2			Tetrodotoxin (TTX)[e]	0.3µM	NaGTP[g]	0,1
	Glucose	25					Phosphocreatine (PC)[h]	20
							Phosphocreatine kinase (PCK)[i]	50Units/mL
							Leupeptin[j]	0,1
pH	7.4 (NaOH)		7.2 (CsOH)		7.4 (CsOH)		7.1 (CsOH)	
mOsm/Kg	300-310		285-295		290-300		270-280	
Junction potential (mV)[k]	9.5				11.6			

Notes

Composition of I_{Na} solutions according to Costa, P. F. (1995)

Composition of I_{Ca} solutions according to Ribeiro, M. A. and Costa, P. F. (2000)

[a,b] Blocks K^+ currents

[c] Blocks Ca^{2+} currents

[d] Cs^+ as a substitute of K^+ ions and F^- as the counter anion known to estabilize the patch

[e] Blocks Na^+ currents

[f, g, h, i, j] Used to retard current run-down

[k] Liquid junction potential between bath and filling solutions, calculated with JPCalc (Barry, 1994).

Currents were recorded with an Axopatch1D electrometer (Axon Instruments) and a pCLAMP 6.0 software (Axon Instruments). Signal was digitized using a DigiData 1200 interface and a 20 µs sampling interval. The holding potential was -70mV. Series resistance (Rs) was compensated to about 80%-90%. Rs values bellow 1MΩ enabled me to reduce the errors associated with the voltage drop introduced by series resistance. The currents were sampled with a low-pass 4-pole Bessel filter at a frequency of 5 kHz. Electrode and cell membrane capacitances were compensated, and membrane surface area was estimated from the reading of the cell capacitance compensation dial, assuming a specific membrane capacitance of 1 $\mu F.cm^{-2}$. Leak subtraction was digitally applied to raw data using a P/4 protocol (Bezanilla & Armstrong, 1977). Holding current (I_p) was used as an indirect measure of leakage current. Patches with I_p values more negative than -60pA were not considered for analysis.

Recordings were allowed to stabilize for 5 min before current recording started, remaining stable for at least 30min. After attaining whole cell configuration, cells were lifted from the bottom of the chamber, brought near the surface and remained under continuous bath perfusion. Experiments were carried out at room temperature (about 20 °C). Data in the present report were not corrected for the junction potential.

3.1.6 Inside-out excised patch clamp recordings

Unitary Na^+ channel current traces were recorded using an inside-out excised patch configuration (Hamill *et al.*, 1981). Composition of filling and bath solutions is showed in table 3.2.

Table 3.2- Composition of bath and filling solutions used to record single-Na^+ channel currents

Composition of solutions used in inside-out patch clamp recordings				
	I_{Na}			
	External (filling solution)	mM	Internal (bath solution)	mM
	NaCl	150	NaCl	1
	KCl	5	CsF	145
	HEPES	10	HEPES	10
	$CaCl_2$	1,8	EGTA	5
	$MgCl_2$	0,9	CsCl	20
pH	7.4 (CsOH)		7.2 (CsOH)	
mOsm/Kg	305		320	
Junction potential (mV)[k]	8.7			
Notes	Composition of solutions according to Fernandes, J. et al. (2001)			

The signal-to-noise output was a major concern, for the currents were recorded in the pA range. Thus, in order to null the stray currents (capacitive currents, leak currents), several technical requisites were considered: 1) the usage of small patch pipettes (~3cm length), designed for low-noise single channel recordings, with an outside/inside diameter of 1.5mm/0.86mm and coated with a hydrophobic agent in the shank (ex: sylgard) to reduce pipette capacitance and background noise; 2) routine cleaning of the pipette holder (also of small dimensions), electrode wires and pipette itself (the glass of the pipette was cleaned by boiling in diluted HCl acid for 5min, washed and oven-dried); 3) the tip of the pipette had reduced dimensions and was fire-polished to further reduce the tip diameter to a final resistance of 15 to 25 MΩ. All the background procedure aimed at reaching an adequate seal in a tiny area of the membrane (‘patch’). In the present study, seals resistance ranged from 20 to 100 GΩ, being often greater than 50 GΩ. The electronics was also adequate for the exigency of this technique. The amplifier used in the experiments provided a 4) high input resistance to permit recordings of subpicoampere input currents (for further details, see annex II, Figure 7.2). Additionally, prior to a patch recording, 5) a pipette was filled with pipette solution up to the shank, and back-filled with liquid paraffin. During the recordings, 6) the location of the pipette (tip near the surface of the bath) was also found critical for relatively low noise (Fernandes *et al.*,

2001). These requisites, enabled to reach noise levels as low as 0.15 pA r.m.s. Unstable and noisy (>0.40pA) patches were discarded.

Single-channel currents were recorded at 20ºC with an Axopatch-200B electrometer and pClamp 6.0 software (Axon Instruments). The acquisition was made through an interface TL-1 DMA (Axon Instruments) with a sampling interval of 25 µs and analog filtering of filter f_a= 5 kHz (-3 dB, 4 pole Bessel). Holding potential was -70mV. Currents were evoked with 40ms depolarizing command pulses ranging from -60 to +20 mV (in 10 mV steps), preceded by pre-pulses to-110mV. Typically, patches were stable for about 30 min, occasionally for 1 h. Capacitance transients were averaged from blank traces and subtracted to sweeps with channel openings.

The signal processing was carried out under the operator´s constant surveillance, to reduce the introduction of artifacts and to allow for event detection interpretation. Unitary Na^+ current amplitude measurements were performed using the 50% crossing method (Ogden, 1994). The rise time (t_r) is described as the time taken for the signal to rise from 10% to 90% of its final amplitude:

$$t_r = \frac{0.3321}{f_c} \qquad \textit{(Equation 3.1)},$$

Where f_c is the cut-off frequency (Hz), here only characterized by the analog filter of the recording system, 5 kHz, as no digital filtering has been used. To assure the detection of fully resolved openings, an open time resolution, which is thought as the shortest time interval that can be measured, was imposed prior to histogram binning. To obtain reliable amplitude measurements, the imposed time resolution was 2 t_r. Thus, the maximum time resolution used in the present study was 132.8µs.

All-point amplitude histograms were constructed. The peak current of the openings was determined from Gaussian fits to the distributions (Sakmann & Neher, 1995). Channel conductance was estimated by averaging the slope of the regression line of the current to voltage (*I-V)* plots obtained for each patch, either in fed and fasted animals.

3.1.7 Plasma membrane-enriched fractions preparation

Hippocampal plasma membrane fractions were prepared as described previously (Sun *et al.*, 1988) with some modifications. Hippocampi from fed and fasted rats were homogenized in ice-cold homogenization buffer - 0.32M sucrose, 50mM Tris HCl (pH7.4), 1mM EDTA, 2mM EGTA, 1x protease inhibitor cocktail from Roche® Diagnostics -, using a glass tissue homogenizer pestle, and centrifuged for 10min at 500g to sediment nucleus and cell debris. The supernatant was centrifuged at 18800g, for 20min, to obtain a crude mitochondrial pellet. The post-mitochondrial supernatant was centrifuged at 43500g for 30min, which resulted in the sedimentation of a white-colored pellet. This pellet, constituted by the crude plasma membranes, was resuspended in lysis buffer – 150mM NaCl, 1mM EGTA, 50mM Tris HCl (pH7.4), 1% (w/v) sodium deoxycholate (D.O.C), 1% (w/v) nonidet P (NP-40), 0.1% (w/v) sodium dodecyl sulphate (SDS), 1x protease inhibitor cocktail– and placed on ice for 30min. The protein concentration was determined by the bicinchoninic acid (BCA) protein assay kit (Micro BCA Pierce Thermo®) using BSA as a standard. Plasma membrane-enriched fractions were then used immediately or stored at -80ºC until use. All steps were performed on ice and centrifugations at 4ºC.

3.1.8 Western blotting

20 µg proteins were denaturated in Laemmli sample buffer containing (in %w/v): dithiothreitol (DTT) 0.77, bromophenol blue 0.01, glycerol 5, SDS 1.5 and Tris-HCl 0.5M (pH6.8); applied in a 7% SDS-Polyacrylamide gel electrophoresis and wet transferred to a Polyvinylidene difluoride (PVDF) membrane. Blots were blocked for 2 hours at room temperature in 5% skimmed milk in Tris-buffered saline (TBS) with 0.1% of Tween 20 detergent (TBS-T 0.1%) prior to the incubation with primary antibody overnight at 4ºC. The antibodies used were polyclonal anti-$Na_V1.2$ (1:1000, Alomone labs ®, ASC-002) and as a loading control, the polyclonal anti N-cadherin (1:1000, Alomone labs ®, ANR-082). Blots were washed several times in TBS-T 0.1% and incubated with the secondary antibody polyclonal goat anti-rabbit IgG (H&L) peroxidase conjugated (1:3000, Rockland®, 611-1302) for 120min at room temperature. Membranes were washed in TBS-T 0.1% and incubated with enhanced luminol chemiluminescence

reagents (Clarity ECL Bio-rad®) according to the manufacturer instructions. The density of the signals was detected in a Chemidoc Molecular Imager (Chemidoc, Biorad®) and densitometry was performed using the ImageLab software (Biorad®).

3.1.9 Statistical analysis

Statistical analyses were performed using SigmaStat 4.0 (Systat Software, Inc., San Jose, CA, USA). The significance of the differences between the data of the two groups studied – fed and fasted animals – was calculated as follows: Samples size $n \geq 10$ were subjected to a two-tailed unpaired *t*-student test; samples in which $n < 10$ or that failed normality test, the non-parametric Mann-Whitney U-test was used for statistical procedures. Values given in the text are means ± S.E.M, unless otherwise stated. Differences for experimental data were considered statistically significant for $P < 0.05$. Exact *P*-values are presented in the tables along the thesis.

Off-line analysis of electrophysiological data was carried out using Clampfit 10 (Molecular Devices, USA), Origin 8.0 (Originlab, USA) and Microsoft Excel® (Microsoft, USA).

3.2 Voltage-gated Na^+ channels

Physiologists have many reasons to admire the Na^+ channel (Marban et al., 1998).

3.2.1 Brief introduction on behaviour and functioning

Voltage-gated sodium (Na^+) channels (hereafter termed VGSCs or Na_v) are major key players in initiation and propagation of action potentials in excitable cells. They were firstly introduced to the scientific community by Hodgkin and Huxley in the 50´s of last century with their voltage clamp experiments in the giant squid axon (Hodgkin & Huxley, 1952*a*). They have noticed that *when the membrane potential is suddenly reduced (depolarization), the initial pulse of current through the capacity of the membrane is followed by large currents carried by ions (chiefly sodium and potassium), moving down their own electrochemical gradients. The current carried by sodium ions rises rapidly to a peak and then decays to a low value.*

In a series of five papers (Hodgkin & Huxley, 1952*a*, 1952*b*, 1952*c*; Hodgkin & Huxley A.F., 1952; Hodgkin *et al.*, 1952), they have developed a thorough biophysical and mathematical description of Na^+ currents, with two distinct and independent processes; a first, rising phase, which they called activation, and a second, decaying phase, developed with an exponential time course – inactivation. Furthermore, they show that activation is related to the existence of 3 charge particles present in the structure of the channel – *m* particles – and that inactivation results from the movement of another particle – *h* particle. The product of these particles (m^3h) illustrated the better description of the Na^+ conductance through VGSCs. The Hodgkin and Huxley (H-H) model, in which they have assumed a diphasic model with a first order reaction (two states in equilibrium, open and closed), enabled them to derive the mathematical equations and functions (rate constants, time constants) that furnished a reliable description of the VGSCs functioning.

Later work, revealed that H-H model is no longer the most adequate to describe the behaviour of such channels (Bezanilla, 1977; Horn & Vandenberg, 1984; Aldrich & Stevens, 1987; Patlak, 1991; Vandenberg & Bezanilla, 1991). These authors demonstrated inactivation as coupled to activation (the coupling model), for the inactivation to occur it is necessary that the mechanism of activation must have happened at least at some extent (Bezanilla & Armstrong, 1977; Goldman, 1995; Armstrong, 2006). Currently, it is known that inactivation can occur from open and closed states (Figure

3.4), as long as the latter contains some degree of activation (gating mechanisms related to voltage sensor).

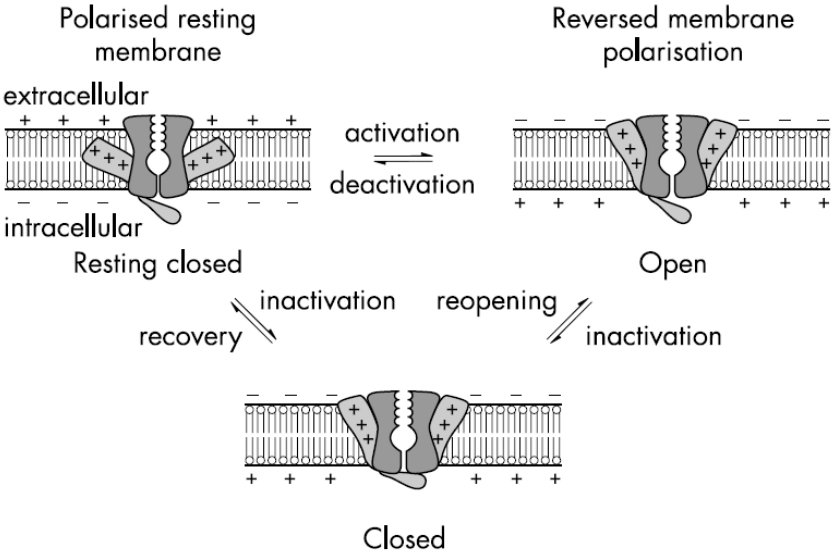

Figure 3.4- ***Scheme of three potential states of voltage gated ion channels such as those for sodium ions****. The resting closed channel state (upper left panel) is activated by membrane depolarisation which causes a fast transition to the open state (upper right). Owing to an intrinsic inactivation, the channel closes (lower panel) and reopens very rarely. Repolarisation of the membrane leads to recovery from the inactivated (refractory) state back to the resting state (upper left) from which activation is again possible. There are probably more than one open and at least two inactivated (fast and slow) states (not shown). Note that transition from the resting to the inactivated state is also possible without channel opening, particularly during slow depolarisation (so called accommodation). Note also that the amphipathic voltage sensor helices (here depicted with positive charges) move within the lipid bilayer when the membrane polarity changes. Taken from (Lehmann-Horn & Jurkat-Rott, 2003).*

3.2.2 VGSCs subunits in mammalian brain - structure and background biophysics

The discovery of the channel protein structure (Catterall *et al.*, 1979; Hartshorne & Catterall, 1984; Noda *et al.*, 1984, 1986) was a breakthrough towards the comprehension of functioning of these channels. The sodium channel α-subunit is 260kDa and consists of four domains, each with six membrane-spanning regions (S1-S6) which give fully functional expression (Figure 3.5). Nine genes encode VGSC α subunits in mammals ($Na_V1.1$ to$Na_V1.9$), and four are expressed primarily in the Central Nervous System (CNS) ($Na_V1.1$, $Na_V1.2$, $Na_V1.3$, and $Na_V1.6$). Other structures, β-subunits (β1-β4, 33–36 kDa), provide support to the α-subunit of channels, being required for the normal kinetics and voltage dependence of channel gating (Isom, 2001). For instance, β1 and β2 subunits potentiate the fast kinetics properties of $Na_v1.2$ (Nguyen & Goldin, 2010), the major α-subunit in brain (Gordon *et al.*, 1987; Westenbroek *et al.*, 1989). Furthermore,

they are also involved in channel localization and interaction with cell adhesion molecules, extracellular matrix, and intracellular cytoskeleton (Isom, 2001).

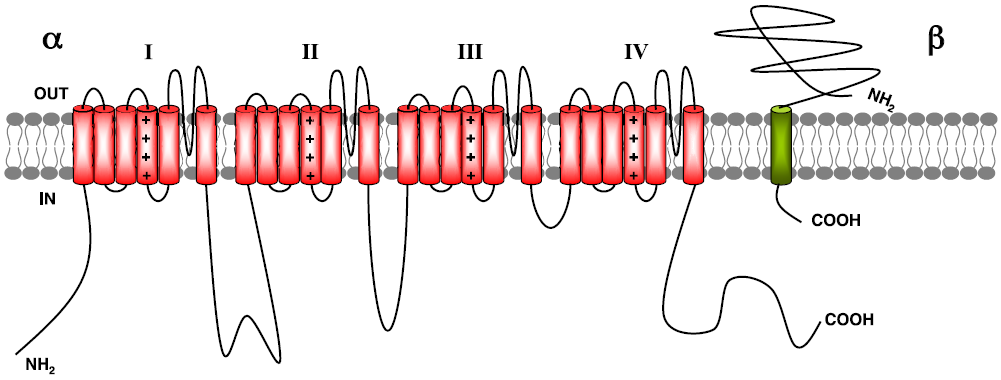

Principal Subunits

Name	Gene	Subcellular Localization
$Na_v1.1$	*SCN1A*	soma, dendrites, some axon
$Na_v1.2$	*SCN2A*	axon
$Na_v1.3$	*SCN3A*	soma, dendrites
$Na_v1.6$	*SCN8A*	axon, some somatodendritic

Auxiliary Subunits

Name	Effects on α function
β_1	trafficking, gating
β_2	gating
β_3	trafficking, gating
β_4	gating

Figure 3.5- ***Subunit composition and subcellular localization of Na_v channel principal and auxiliary subunits in mammalian central neurones****. Schematic representation of a single $Na_v\alpha$ subunit that forms macromolecular complexes with auxiliary Na_v β subunits. Bottom left box: classification, genetic nomenclature, and subcellular localization of mammalian brain Nav channel principal α subunits. Bottom right box: classification of Na_v β auxiliary subunits expressed in mammalian central neurones and their functional effects on coexpressed Na_v α subunits. Taken from (Vacher* et al.*, 2008)*

The unveiling of the primary structure preceded a wide range of site-directed mutagenesis experiments (Stühmer *et al.*, 1989; O'Leary *et al.*, 1995; Hirschberg *et al.*, 1995; Kontis & Goldin, 1997; Vedantham & Cannon, 1998; Kühn & Greeff, 1999; Goldin, 2003*a*; Ulbricht, 2005). The introduction of mutations into mammalian Na^+ channels and analysis of their functional effects by electrophysiological recordings have yielded a remarkably detailed view of the components of the Na^+ channel that are required for its physiological activity. The era of structure-function analysis has begun. It brought important insights into the understanding of the molecular determinants of Na^+ channels, with special attention given to the α-pore forming subunit (Figure 3.6).

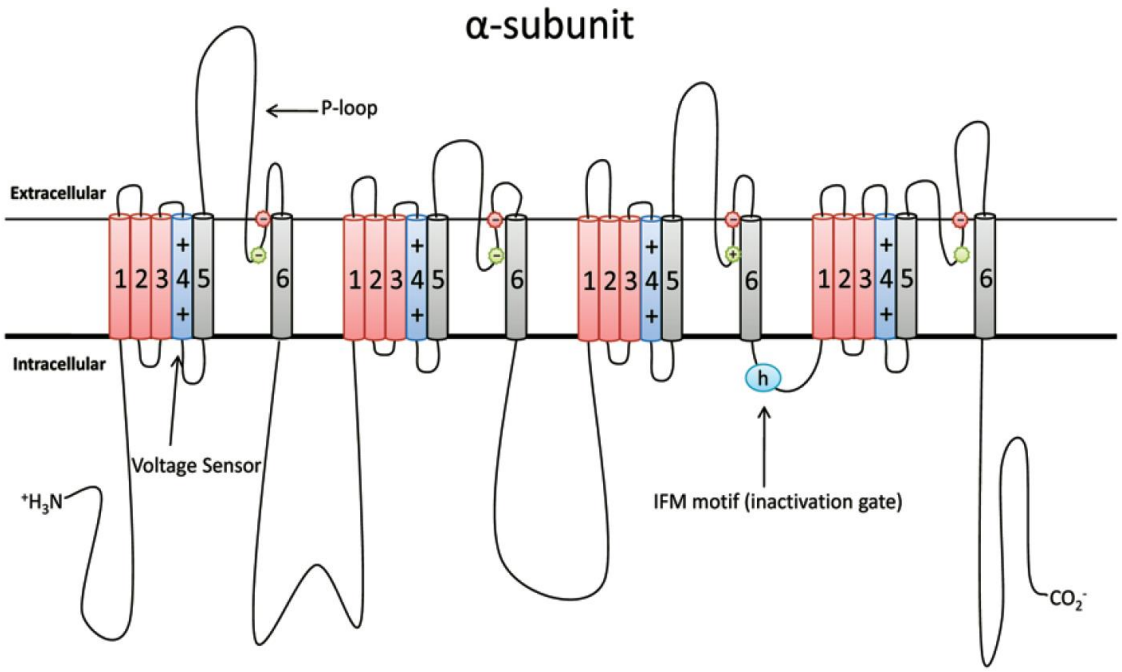

Figure 3.6- ***Molecular determinants of α-subunit of VGSC.*** *S4 segments (in blue) are voltage sensors and IFM motif in intracellular loop between DIII and DIV act as inactivation gate. P-loops of all four domains and S6 segments forms extracellular and intracellular ends of the pore. Taken from (Chong & Ruben, 2008)*

The positively charged amino acid residues, usually arginine, embedded within the S4 segments, presumably convey the channel´s characteristic sensitivity to membrane potential. The movements of such charged groups, prompted by changes in transmembrane potential, constitute the fundamental mechanisms of gating – voltage sensing processes (Armstrong & Bezanilla, 1977*a*; Bezanilla & Armstrong, 1977; Almers, 1978; Patlak & Horn, 1982). Another important region of the channel is the existing extracellular loop between S5 and S6 (S5-S6 linkers in each domain) indicating the selective pore region of the channel (Catterall, 1992). Besides this, there is another intracellular loop between domains III and IV where one can find a hydrophobic motif – IFM (Ile-Phe-Met) – that blocks the channel pore like a hinged lid, holding the gate closed – ball and chain mechanism, proposed by Armstrong and Bezanilla (Bezanilla & Armstrong, 1977). This structure is the molecular basis of fast inactivation. In addition to fast inactivation, during periods of prolonged membrane depolarization channels can also enter into longer non-conducting states collectively termed ‘slow inactivation’ (Webb, 2007). This mechanism is not fully understood, however many lines of evidence point the collapse of the outer pore of the channel as the underpinning phenomenon, by all means

similar to the 'C-type' inactivation of K^+ channels (Vedantham & Cannon, 1998; Vilin & Ruben, 2001; Goldin, 2003*a*; Ulbricht, 2005; Webb, 2007).

3.2.3 VGSCs distribution in rat hippocampal CA1 neurones

Biochemical and immunocytochemical studies indicate that $Na_v1.2$ is the predominant Na^+ channel subtype in most regions of the rat brain including the forebrain, midbrain, dentate, cerebellum, and hippocampus (Gordon *et al.*, 1987; Westenbroek *et al.*, 1989). Specifically, Gordon and co-workers showed that the predominance of $Na_v1.2$ subtype goes as follows: whole brain (81%), cerebral cortex (79%), cerebellum (84%), midbrain (56%) and hippocampus (97%).

In rat hippocampal CA1 neurones, the subcellular distributions of all neuronal subtypes of voltage-gated Na^+ channels ($Na_v1.1$, 1.2, 1.3 and 1.6) have been investigated by using physiological approaches, as well as antibody binding, in some cases combined with electron microscopy. Physiological studies fall into two categories: direct measurement of ion channel function using cell-attached or cell-excised patches from the soma, axon, and dendrites and indirect assessment of ion channel distribution using whole-cell recording in combination with ion-channel pharmacology (Andersen *et al.*, 2007).

Direct recordings of Na^+ channel activity in patches up to about 300 µm from the soma on the primary apical dendrite in CA1 neurones (see Annex I for a visual comprehension of this region) have revealed that Na^+ channels are distributed at an approximately constant density along this region of the dendrite (Magee & Johnston, 1995*a*). The presence of these channels confers very active properties to the dendrites, by allowing for the propagation of Na^+-dependent action potentials into the dendrites from their initiation site in the axon, a mechanism known as 'back-propagation' (Figure 3.7). This activation mechanism also limits the attenuation of the action potential as it propagates distally (Spruston, 2008).

Despite the relatively uniform channel density, the properties of the channels change with distance from the soma. For example, patches obtained at increasing distances from the soma exhibited more prolonged inactivation (Mickus *et al.*, 1999*a*). Such variation in the biophysical output found along the length of the neurones may rely either on a modal gating of a specific channel subtype (Alzheimer *et al.*, 1993; Taylor, 1993; Fernandes *et*

al., 2001) (the same channel reveals different degrees of inactivation, ranging from a short single opening to periods of long-lasting openings and re-openings), and/or on a distinct distribution of channel subtypes. Regarding the second consideration, it has been established that $Na_v1.1$ and $Na_v1.2$ have a complementary distribution in rat CA1 pyramidal cells: $Na_v1.1$ (and $Na_v1.3$, in immature neurones) are preferentially localized in the cell bodies and proximal dendrites, where they control neuronal excitability through integration of synaptic impulses (Gordon *et al.*, 1987; Westenbroek *et al.*, 1989; Gong *et al.*, 1999). In contrast, $Na_v1.2$ is predominantly expressed in unmyelinated fibers in the mossy fiber pathway and in the other fiber layers of the hippocampus with a high density of axons (Gordon *et al.*, 1987; Gong *et al.*, 1999). In the CA1 neurones, $Na_v1.2$ can be encountered in the proximal part of the initial segment of axons (AIS) (Vacher *et al.*, 2008; Hu *et al.*, 2009; Qiao *et al.*, 2013; Wang *et al.*, 2017), whereas the distal AIS is mostly populated by $Na_v1.6$ channels (Hu *et al.*, 2009; Grubb *et al.*, 2011; Qiao *et al.*, 2013) (Figure 3.7).

This segregation of Na^+ channel subtypes at the AIS sets a biophysical model, in which the low-threshold $Na_v1.6$ channels are responsible for the initiation and propagation of action potentials along axon and the high-threshold $Na_v1.2$ channels support action potential backpropagation to the soma and dendrites (Hu *et al.*, 2009; Grubb *et al.*, 2011).

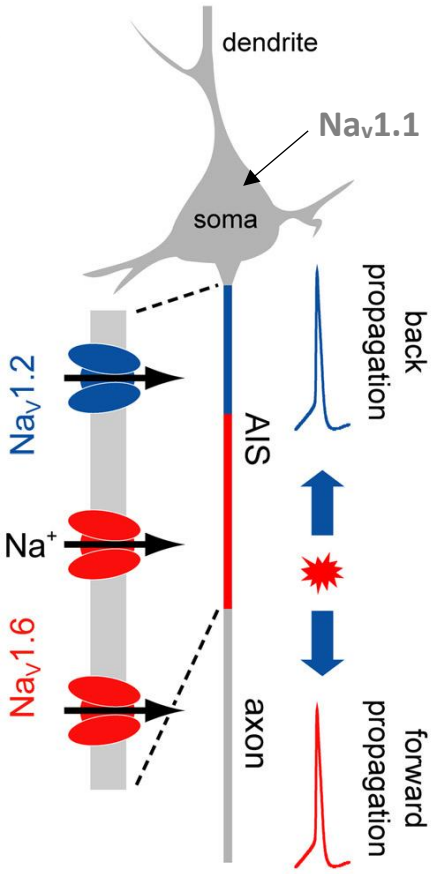

Figure 3.7- ***Function and modulation of AIS ion channels.*** *A, Schematic detailing roles of Na^+ channel subtypes in AP initiation and backpropagation in pyramidal neurones. Accumulation of the low-threshold $Na_v1.6$ channels at the distal AIS determines the lowest threshold for AP initiation, whereas accumulation of the high-threshold $Na_v1.2$ channels at the proximal AIS promotes AP backpropagation to the soma and dendrites. The neuronal location of $Na_v1.1$ is also illustrated. Adapted from (Grubb et al., 2011)*

3.2.4 Influence of Feeding cycle on neuronal Na^+ currents

The influence of feeding cycle upon the biophysics and expression of voltage gated Na^+ currents (I_{Na}) is addressed in this section. The results here illustrated provide information regarding the effects of feeding cycle on the excitability of rat hippocampal CA1 neurones.

3.2.4.1 Whole-cell voltage clamp recordings

Voltage dependence of activation

Recordings from CA1 hippocampal neurones showed the common behaviour of Na^+ currents (Figure 3.8), with a fast activation and a spontaneously rapid decay (Sah *et al.*, 1988; Costa, 1996; Vreugdenhil *et al.*, 1998; Ketelaars *et al.*, 2001*b*; Bruehl & Witte, 2003), reaching a peak within 0.6ms at -10mV. Na^+ currents were evoked with a step of depolarized voltages from -60mV up to +30mV, following a conditioning pulse of -110mV, with a duration of 25ms, to remove inactivation. Holding potential was set at -70mV.

The effect of feeding on sodium currents is depicted in Figure 3.8. Upon feeding, the amplitude of Na^+ current increased: mean peak current amplitude was -14.2 ± 0.76 nA (n=18), as opposed to - 8.7 ± 0.74nA (n=28) in neurones from fasted animals. The nature of the currents was confirmed by the blockade of the macroscopic currents upon the application of 1 µM TTX (see inset in figure 3.8). The blocking of TTX was not complete, which indicates the presence of TTX-resistant voltage gated Na^+ channels.

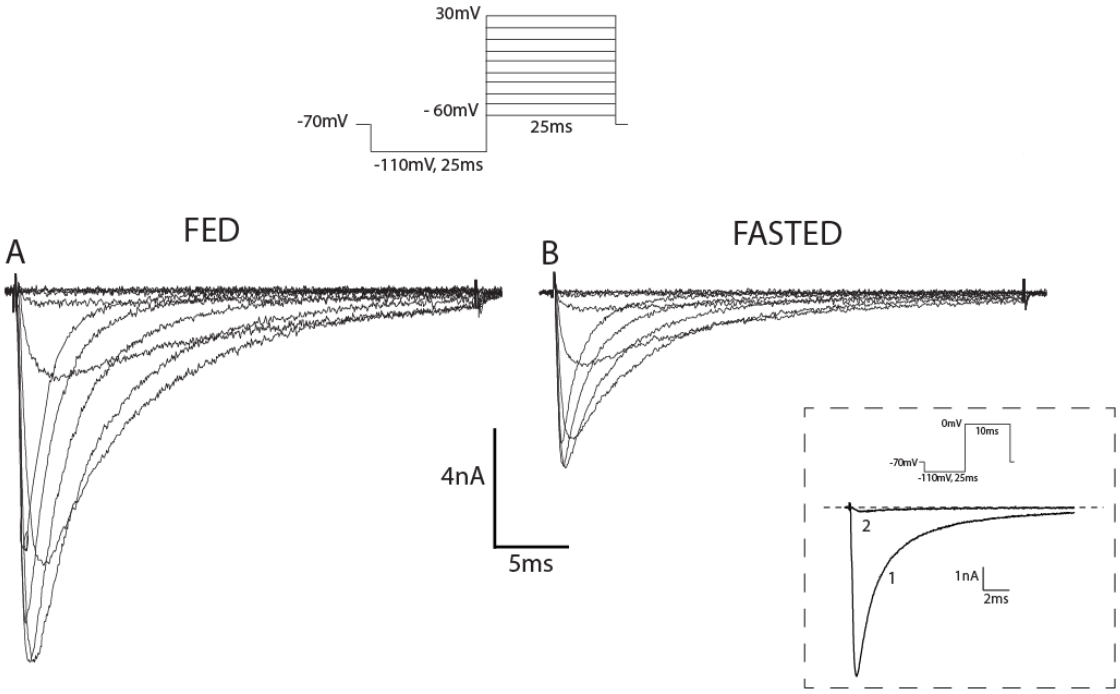

Figure 3.8- ***Effect of feeding cycle over the Na^+ currents of acutely isolated rat CA1 hippocampal neurones****. Whole-cell voltage clamp Na^+ currents, recorded in neurones from fed (A) and fasted (B) animals, were evoked in series of depolarization command pulses (25ms in duration), in steps of 10mV, from -60mV to +30mV, following a hyperpolarizing conditioning pulse at -110mV (25ms in duration). Holding potential was set at -70mV. Traces depict increased Na^+ current amplitudes in fed animals. The inset confirms the nature of the currents, as trace 1 (control current) was blocked by 1μM TTX application (trace 2); currents evoked with a command potential to 0mV from a -110mV prepulse, with a holding potential of -70mV.*

The conspicuous difference in the amplitude is also depicted in the current to voltage (*I-V*) relationship, whose data comprises the mean peak Na current values obtained in the voltage range studied (-60mV to +30mV) (Figure 3.9). Peak current values, I (pA), were normalized to cell capacitance (pA/pF) (Figure 3.9A).

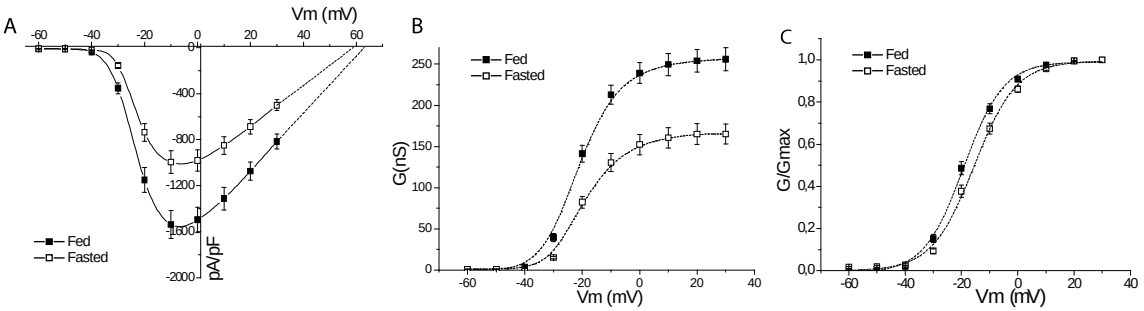

Figure 3.9- ***Influence of feeding cycle on the voltage dependence of activation of Na^+ currents****. Activation curves relate to Na^+ currents like those depicted in figure 3.8. A) I-V curves related to mean Na^+ peak current normalized to cell capacitance (pA/pF); B) Mean conductance (G(nS)) of Na^+ peak currents and C) mean conductance normalized to the maximum value (G/G_{max}), obtained from freshly isolated rat hippocampal CA1 neurones of fed (filled squares; n=18) and fasted (open squares; n=28) animals. Dashed lines in are the solution of Equation 3.3 (in C, V_h= -19.2mV and V_s= 7.1mV/e-fold, for fed neurones; V_h= -15.5mV and V_s= 7.5mV/e-fold, for fasted neurones). Error bars are ±S.E.M. values.*

One might estimate that the average maximum current density (assuming 1µF corresponds to 1cm^{-2}, Hodgkin and Huxley) for fed and fasted neurones, at -10mV, are 1.5$mA.cm^{-2}$±0.12 and 1.0$mA.cm^{-2}$±0.10, respectively. The difference is statistically significant (P < 0.001). Furthermore, the reversal potential measured by linear extrapolation (see Figure3.9A) was close to the theoretical equilibrium potential for Na^+ ions of +57.6 mV, predicted by the ionic conditions. This result, together with the blockade of Na^+ currents by TTX, accounts for the involvement of Na^+ currents towards the influence of feeding cycle on rat hippocampal CA1 neurones activity.

The voltage dependence of Na^+ currents activation was studied in both conditions. Current peak values were converted to conductance, G(nS) (Figure 3.9B), as follows:

$$G = I/(V_m - E_{Na^+}) \qquad \text{(}\textit{Equation 3.2}\text{)},$$

where I is the current amplitude, V_m is the step command potential and E_{Na^+} is the estimated equilibrium potential for Na^+.

Fed neurones present higher values of conductance nearly in all studied voltage range, with a mean maximum conductance values, at 40mV, of 255.9 ± 13.95nS, compared to 165.2 ± 11.98nS calculated for fasted neurones. The results are statistically significant (P < 0.001). Taken together, figures 3.9A and 3.9B show that fed neurones exhibit larger whole-cell conductance, which is associated with higher Na^+ current density.

The voltage dependence of activation was studied normalizing G (nS) for its maximal value (G/G_{max}) and plotting the mean values against step command potential (Figure 3.9C). The analysis of the fraction of open channels was carried out by fitting a Boltzmann

distribution to the resulting data, whose parameters quantify the influence of feeding cycle in the activation of Na^+ channels:

$$G/G_{max} = 1/\{1 + exp[(V_h - V_m)/V_s]\} \quad \textit{(Equation 3.3)},$$

Where V_h is the half-activation potential (mV), V_s is a slope factor (mV/*e*-fold) and V_m is the step command potential (mV).

The average fitting parameters values of activation curves – V_h and V_s - are presented in table1. V_h values were as follows: -15.2 ± 0.89mV and -19.1 ± 0.87mV, for fed and fasted neurones, respectively. This result is statistically significant ($0.001 < P < 0.01$), supporting the shift towards hyperpolarizing potentials (roughly 4mV) of the activation of Na^+ currents, observed in fed neurones (Figure 3.9C). V_s values were similar in both conditions: 6.7 ± 0.35 mV/e-fold and 6.8 ± 0.25 mV/e-fold, for fed and fasted neurones, respectively.

Steady-state inactivation (h_∞)

The steady state of inactivation was studied with a conditioning double-pulse protocol (Hodgkin & Huxley, 1952*b*), by which Na^+ currents were evoked with pre-pulses ranging from - 120 mV to 0 mV, 40ms in duration, from a holding potential of -70mV, in conjunction with a depolarizing command step to a fixed voltage (0mV, 30ms). Currents evoked with such voltage-clamp protocol are depicted in Figures 3.10A and 3.10B.

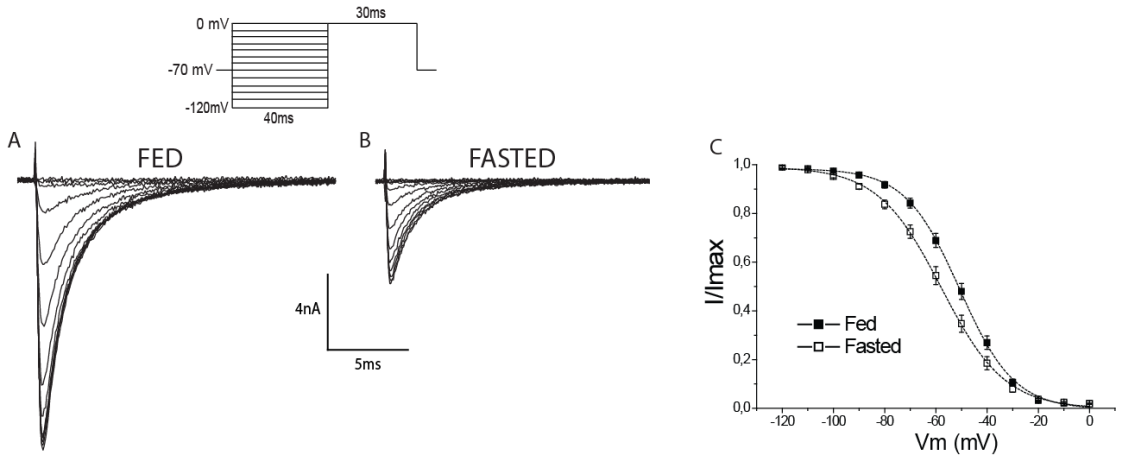

Figure 3.10- ***Influence of feeding cycle on steady-state inactivation (h_∞) of Na^+ currents****. Whole-cell voltage clamp Na^+ currents were evoked by a command step to 0 mV (30ms) following a set of pre-pulses (40ms) ranging from −120 mV to 0 mV in steps of 10 mV; holding potential of −70 mV (inset). Records were obtained from a neuron of a fed (A) and (B) fasted animal. C) Mean peak Na^+ current obtained in the test pulse normalized to the maximum value (I/I_{max}) as a function of pre-pulse potentials, from neurones of fed (filled squares; n=24) and fasted (open squares; n=27) animals. The steady-state inactivation curves (h_∞) were fitted with equation 3.3 (V_h= -50.7mV and V_s= 10.7mV/e-fold, for fed neurones; V_h= -57.8mV and V_s= 12.4mV/e-fold, for fasted neurones). Error bars are ±S.E.M. values.*

Peak current values were normalized to the maximal response (I/Imax) and plotted against pre-pulse potential to obtain steady-state inactivation curves (Figure 3.10C). Data points were fitted with a Boltzmann distribution (*equation 3.3*) and the results can be directly compared with the h_∞ curve obtained by Hodgkin and Huxley (Hodgkin & Huxley, 1952*b*), giving us information about the steady state availability of sodium channels to respond to activation.

Here, we can also quantify the effect of feeding cycle over the steady state properties of inactivation (see Table 3.3). The average fitting parameters were as follows: Vh = -51.2 ± 1.50mV, Vs = -9.8 ± 0.45 mV/e-fold in fed neurones (n=24) and Vh = -58.4 ± 1.81 mV, Vs = -10.9 ± 0.35 mV/e-fold in fasted neurones (n=27). The results demonstrate that Na^+ currents in CA1 neurones showed a significant voltage shift during the feeding cycle ($0.001 < P < 0.01$). As presented in Figure 3C, from -90mV to -40mV, the Na^+ currents of fed animals display comparatively higher I/Imax values due to a shift towards depolarized potentials by 7mV. Thus, the voltage profile observed in inactivation curves of fed neurones showed a significant depolarization in comparison with that obtained in fasted neurones. This demonstrates that Na^+ currents in fasted neurones begin to inactivate at more negative potentials. Once again, the voltage dependence, given by the steepness of the h_∞ curves, was similar in both feeding conditions.

Table 3.3- Activation and steady-state inactivation (h_∞) fitting parameters V_h (mV) and V_s (mV/e-fold) (Eq. 3.3) for neurones of fed and fasted animals. Statistical analysis performed with a t-test; 0.001<P-value<0.01

	Voltage dependence of activation (mV)			**Voltage dependence of inactivation (mV)**		
	V_h	V_s	*n*	V_h	V_s	*n*
Fed	-19.1 ± 0.87	6.7 ± 0.35	18	-51.2 ± 1.50	9.8 ± 0.45	24
Fasted	-15.2 ± 0.89	6.8 ± 0.25	28	-58.4 ± 1.81	10.9 ± 0.35	27
P-value	0.005	*n.s.*	-	0.004	*n.s.*	-

Na^+ channel availability

To a better visualization of the effect of feeding cycle on the steady state properties of activation and inactivation, we have addressed the fraction of permanently activated channels. Overlapping the activation and inactivation of Na^+ channels, it is possible to define a range of voltages (*i.e.*, 'window') where the channels are partially activated but not fully inactivated (Figure 3.11).

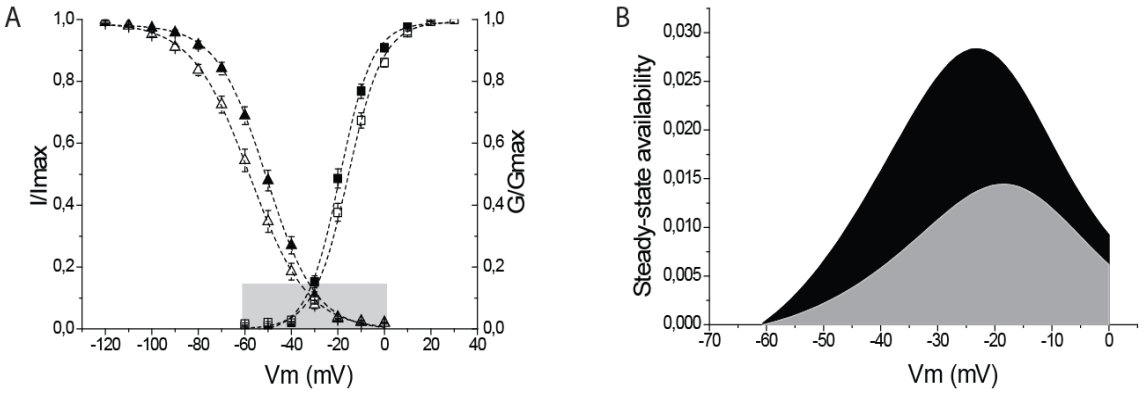

*Figure 3.11- **Window current of voltage gated Na^+ currents obtained from neurones of fed and fasted animals**. A) Voltage dependence of activation and steady-state inactivation curves as depicted in Figures 3.9C and 3.10C. The area highlighted by a grey area relates to a voltage range (´window´) in which Na^+ currents are partially activated although not fully inactivated. B) The product of the activation and h_∞ curves give the probability of channels being present in this region (Huang et al., 2011). Na^+ channels in fed animals (black area) depict a larger availability when compared to the Na^+ channels in fasted animals (grey area).*

The probability of being within this 'window', highlighted in Figure 3.11A as a grey area, was calculated from the product of the activation and steady-state inactivation curves (Huang *et al.*, 2011). The feeding enlarged the window, shifted the peak toward negative potentials and produced a twofold increase in amplitude (3%, Figure 3.11B). The sustained 'window' current presented here is, thus, the result of an increase in the

"window current" of fed neurones caused by a positive shift of the steady-state inactivation and a negative shift of the activation curve (Figure 3.11A).

Time-constant of inactivation (τ_h)

The decay phase of the Na^+ currents, obtained with activation protocols (Figure 3.8), was described with an exponential time course, using an equation of the form

$$I = a_f e^{-t/\tau_{hf}} + a_s e^{-t/\tau_{hs}} + C \qquad \textit{(Equation 3.4)},$$

where τ_{hf} and τ_{hs} are the time-constants of the fast and slow inactivating components, respectively; a_f and a_s are the amplitude coefficients and C is a constant.

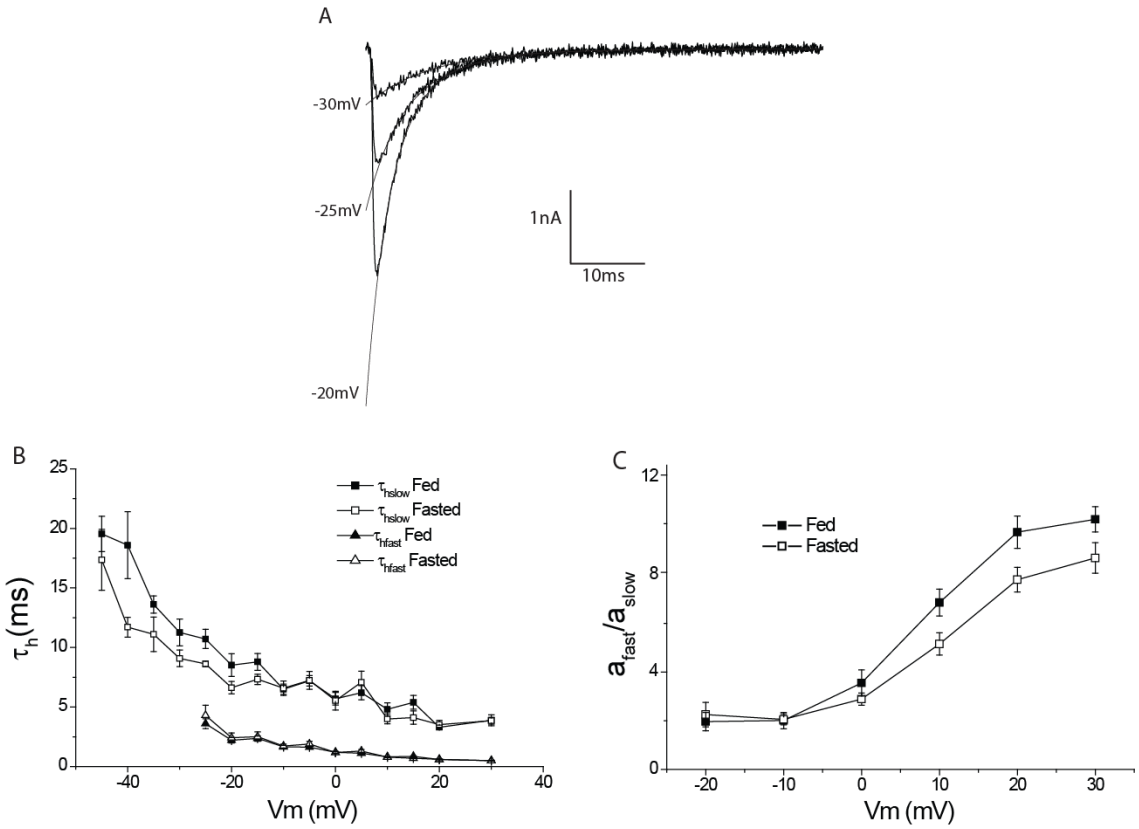

Figure 3.12- ***Effect of feeding cycle on the kinetics of inactivation of Na^+ channels****. A) Fitting of the decay phase of Na^+ currents evoked by an activation protocol. The inactivation could be described by a single (-30mV command pulse) or a by double exponential (-25mV and -20mV command pulses), equation 3.4. B) Voltage-dependence of the time-constant of inactivation (τ_h(ms)) measured in activation protocols, in which Na^+ currents were evoked in series of depolarization command pulses, in steps of 5mV, from -45mV to +30mV; slow (squares) and fast (triangles) inactivation components in neurones of fed (filled symbols; n=18) and fasted (open symbols; n=28) animals. C) Voltage-dependence of the fast/slow ratio of the two exponential components of inactivation in fed (filled squares, n= 18) and fasted (open squares, n= 28) neurones. Error bars are ±S.E.M.*

Figure 3.12A illustrates exponential fits to the decay phase of currents evoked in command steps to -30, -25 and -20 mV from -70 mV holding potential. At -30 mV, the current decayed monoexponentially with a time constant of 8.1 ms; at -25 and -20 mV,

the inactivating phase was best described by two exponentials, with time constants of 7.6; 3.8 ms and 6.8; 2.5 ms, respectively. Figure 3.12B shows the mean inactivation time constants values measured in activation protocols. At a hyperpolarized V_m range (from -45mV to -30mV), we could only determine a single exponential with slow kinetics (τ_{hslow}); at -40mV, we have obtained τ_{hslow} 18.6 ± 2.81ms and τ_{hslow} 11.7 ± 0.83ms for fed and fasted neurones, respectively. Results are statistically significant ($0.001 < P < 0.01$). For voltage command steps more depolarized than -25mV, two exponentials were ascribed to the time course of inactivation, revealing the existence of two inactivating components, with slow (τ_{hslow}) and fast kinetics (τ_{hfast}). In command steps to -20mV, the mean inactivation time constants measured in fed neurones were as follows: τ_{hslow} 8.5 ± 0.95ms and τ_{hfast} 2.2 ± 0.24ms. In fasted neurones, the mean inactivation time constants were: τ_{hslow} 6.6 ± 0.52ms and τ_{hfast} 2.4 ± 0.39ms. Overall, the effect of feeding cycle over the voltage dependence of the time-constant of inactivation is evident at more hyperpolarized potentials, between -45mV and -20mV.

Furthermore, as previously observed by P. F. Costa (Costa, 1996), the proportion of fast and slow inactivating components - a_{fast} and a_{slow} - changed with depolarization. The faster inactivating component dominated at values less negative than -20mV, attaining ~92% of total current amplitude at large depolarizations up to +30 mV, in fed neurones. Figure 3.12C depicts the voltage-dependence of the ratios calculated from the coefficients in *Equation 3.4* (a_f/a_s). At 30mV, the mean ratio values were: 10.3 ± 2.26 and 8.7 ± 3.25 for fed (n=18) and fasted (n=28) neurones, respectively. Ratio values obtained from fed and fasted neurones, in the voltage range between 10mV and 30mV, were statistically significant ($0.01 < P < 0.05$). The higher contribution of fast components in fed neurones suggests a difference in protein expression levels at the surface of neuronal plasma membrane between animals subjected to fed and fasting conditions.

3.2.4.2 Single-channel analysis – inside-out excised patch configuration

The macroscopic Na^+ currents showed distinct characteristics whether the animals were fed or kept in fasting conditions. To further understand the underlying mechanisms of such outcome, it was critical to address the effect of feeding cycle on the Na^+ channel functioning at a microscopic level.

The information obtained with single-channel experiments is mostly valuable. Here, the equilibrium considerations, exclusive of macroscopic currents obtained in WC experiments, give place to microscopic transitions between states/conformations of the Na^+ channels. The scope of my PhD urged me to study the amplitude of the currents to establish a current-to-voltage (*I-V*) relationship, and thus, obtain the unitary conductance of single- Na^+ channels.

Unitary Na^+ channel currents

Figure 3.13 illustrates single Na^+ channel records in several patches of fed and fasted neurones, using an excised inside-out patch configuration.

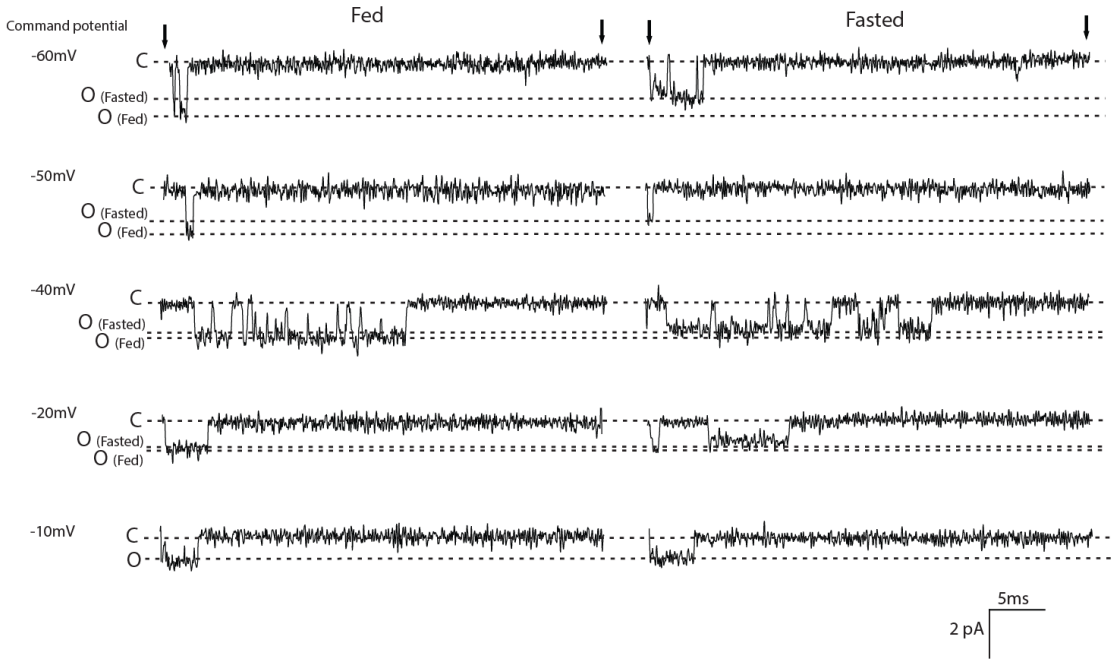

Figure 3.13- ***Influence of the feeding cycle on single Na^+ channel currents of acutely isolated rat hippocampal CA1 neurones****. Single-channel current traces, obtained in inside-out excised configuration, in different patches from neurones of fed and fasted animals, at voltage command steps shown on the left of each record and from a holding potential of -110mV. Arrows (↓) indicate the onset and the end of the voltage command pulses. The horizontal dashed lines represent the closed (C) and open (O) states of channels in preparations from either fasted or fed rats.*

Fed neurones comprised patches with higher current amplitudes. In the patches illustrated in Figure 3.13 it is shown that the observed delta in current amplitude between feeding conditions was obvious at hyperpolarized V_m values, becoming negligible as the command potential steps are depolarized; at -60mV, we could observe a clear difference in current amplitude, which was not observed at -10mV.

Amplitude measurements

The analysis of the single channel records followed the 50% threshold method (Sakmann & Neher, 1995). All point histograms were constructed from the detected events. Figure 3.14 depicts all-point amplitude histograms obtained in patches from fed and fasted neurones, at a pulse command step of -60mV.

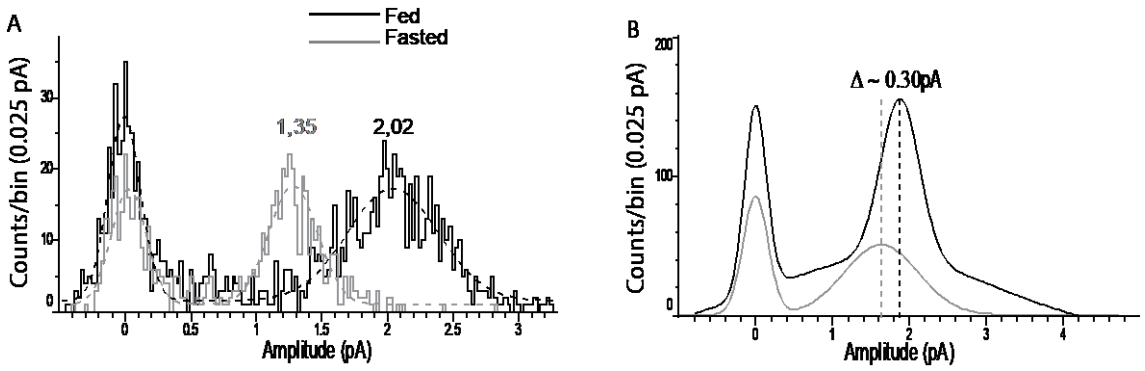

Figure 3.14- ***All-point amplitude histograms (APAH) of unitary Na⁺ currents and corresponding Gaussian fits in patches from fed and fasted animals, at -60mV****. Single Na⁺ channel events obtained by the 50% threshold method (details in materials and methods). (A) APAH of two different experiments in patches from fed (black traces) and fasted (grey traces) animals. The dashed lines were obtained by fitting Equation 3.5 (Gaussian distribution). The humps corresponding to open events are located at peak values of 1.35pA (fasted condition) and at 2.02pA (fed condition). B) Fitting Gaussian curves of pooled data from patches of fed (black line, n=8) and fasted (grey line, n=8) animals. The difference between the two peaks is indicated (~0.3pA; 0.01 < P < 0.05).*

Each amplitude histogram was best described by two Gaussian distributions corresponding to the baseline current (around 0pA, closed states) and the open-channel current, and fitted with a sum of two gaussian curves (presented as dashed lines in Figure 3.14A and lines in Figure 3.14B):

$$f(I) = \sum_{i=1}^{n} A_i \frac{e^{-(x-\mu_i)^2/\left(2\sigma_i^2\right)}}{\sigma_i\sqrt{2\pi}} + C \qquad \textit{(Equation 3.5),}$$

Where μ_i is the mean value, $\sigma_i$is the standard deviation (SD), and A_i is the amplitude of the corresponding curves.

The mean amplitude (μ ± SD) of patches represented in figure 3.14A were estimated as -1.4 ± 0.20pA for a fasted neuron, and -2.0 ± 0.23pA for a fed neuron. In this example, the observed current amplitude in fasted condition was remarkably reduced. Figure 3.14B shows the Gaussian fitting curves related to the average of all-point histograms at -60mV. At this V_m, the unitary Na^+ current amplitudes (± S.E.M.) were -1.9 ± 0.03pA and -1.7 ± 0.09pA for fed (n=8) and fasted (n=8) neurones, respectively. This result is statistically significant ($0.01 < P < 0.05$) suggesting an influence of feeding cycle over the unitary conductance (see Figure 3.15A).

Following this rationale for all patches, we managed to analyze the amplitude of fully resolved openings obtained in voltage steps ranging from -60mV to +20mV. Figure 3.15A depicts Na^+ channel unitary current as a function of step command voltage (*I-V* plots) in

patches from fed and fasted neurones. Points in the plots are mean values and concern measurements obtained in a total of 18 patches, 9 in fed and 9 in fasted conditions.

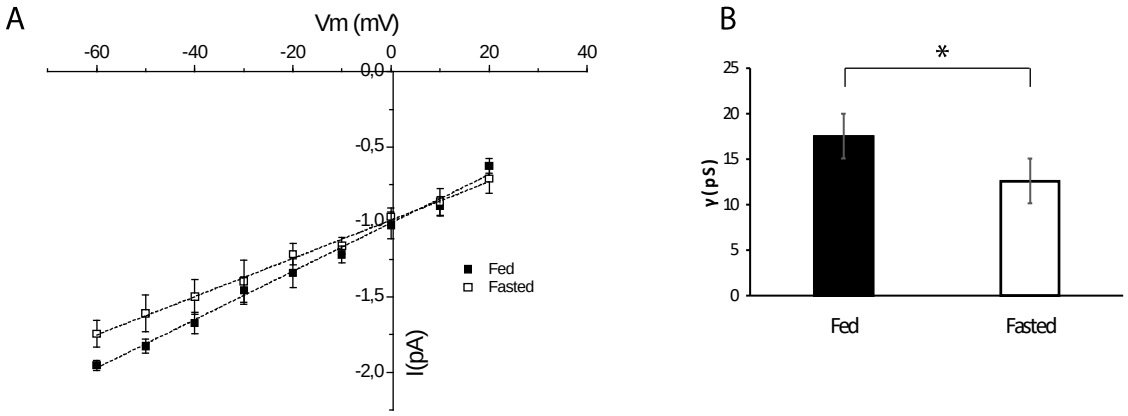

*Figure 3.15- **Single Na^+ channel current as a function of voltage command step (I–V plots)**. A) Mean single channel current amplitude was accessed in fully resolved openings and determined by fitting all-points histograms (see figure 3.14) in patches from fed (n=9 patches) and fasted (n=9 patches) neurones, in voltage command steps from -60 to +20 mV. Dashed lines are linear regression of the average data. B) The mean single-channel conductance, γ(pS), was determined by means of the average of the slope conductance calculated for each I-V plot of patches from fed (~16.7 ±0.76pS, n=8) and fasted (~12.6 ±1.30pS, n=8) conditions. Error bars are ±S.E.M (t-student analysis *0.01<P<0.05).*

The unitary Na^+ channel conductance was estimated from the slope of the regression lines calculated in all patches studied. To obtain reliable slope results, we only used patches where at least 4 voltage commands were applied. The bars represented in Figure 3.15B are mean values. The calculated slope conductance for fed neurones determined between −60mV and +20 mV was 16.1 ± 0.76pS (n=8). Fasted neurones disclosed a smaller mean slope conductance of 12.6 ± 1.30pS (n=8). These conductance results are statistically significant ($0.01 < P < 0.05$), confirming that each Na^+ channel present in the surface of CA1 neurones of fed animals conduct more Na^+ ions, than every single Na^+ channel located in neurones of fasted animals.

Ensemble averages

In order to establish a comparison between the single channel and whole-cell recordings, ensemble averages were obtained by averaging all the current traces with channel openings, produced at a single voltage step, at each time point. The time constant of inactivation for the mean currents was determined by fitting one or two exponentials (*Equation 3.4*; whole-cell currents section) to the decaying phase of the ensemble signal (Figure 3.16).

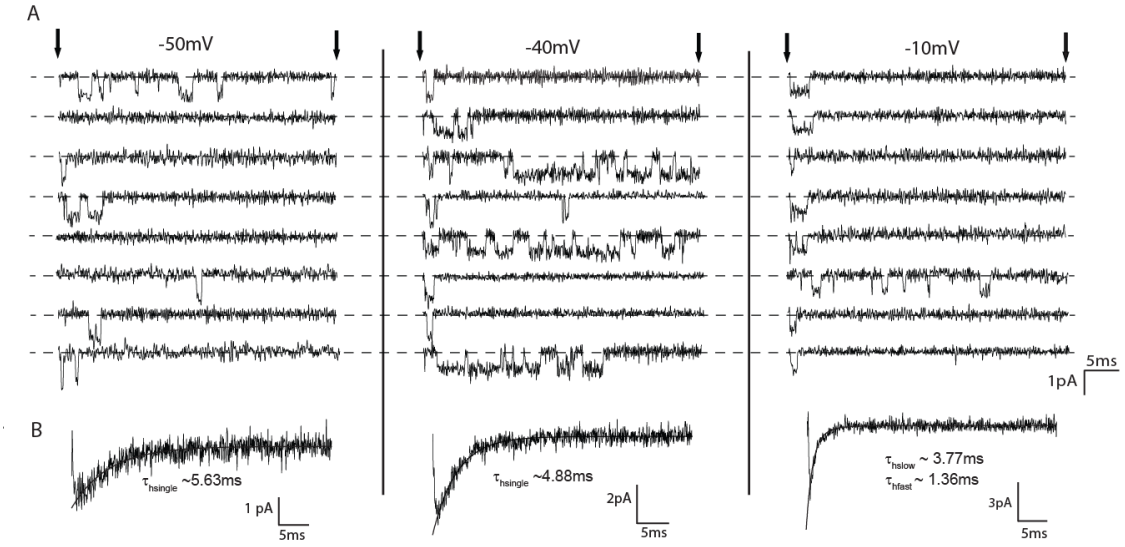

Figure 3.16- ***Illustrative examples of ensemble averages****. A) Representative sweeps of Na^+ channel activity recorded at -50 mV, -40mV and -10 mV from inside-out patches excised from different neurones, both with one apparently active channel. Arrows indicate the onset and end of patch depolarization from -110 mV to the indicated voltage. B) Ensemble averages obtained from each patch depicted in A), from a total of 151 sweeps (-50 mV), 234 sweeps (-40 mV) and 152 sweeps (-10 mV). In -10mV, exponential fits to the decaying phase of the signal were best described by two exponentials (τ_{hf} and τ_{hs}).*

The activity pattern of the sweeps observed in Figure 3.16A is representative of the current traces observed at each membrane potential indicated. At -10mV, brief openings ('non-burst' activity) were mainly obtained, where fast inactivation is prominent (see ensemble averages, Figure 3.16B), and, thus, the possibility of obtaining long lasting or late openings and reopenings is diminished. Such 'burst' activity was rather found at -40mV, where the fast inactivation is less predominant, which increases the likelihood of channel to transit between open and closed states before completion of inactivation. At -50mV, voltage at which the open probability of the sodium channels is generally reduced, non-burst activity was also observed.

Figure 3.16B depicts illustrative ensemble averages obtained from sweeps of different patches in command steps to -50mV, -40mV and -10mV. The decaying phase of the more

hyperpolarized patches (-50mV and -40mV) was better described by a single exponential fit ($\tau_{hsingle}$ = 5.63ms, at -50mV and 4.88ms, at -40mV). At -10mV, the decay phase of the ensemble traces was best described by two exponentials, with τ_{hfast} = 1.36ms and τ_{hslow} = 3.77ms. Such current decays resemble those obtained with the whole-cell approach.

There was variability on the fits applied to all the patches and a tendency emerged when comparing the recordings from fasted neurones to those recorded from fed neurones. In fasted neurones, the fraction of patches in which one single exponential was required in ensemble averages was as follows: 5/5 (-60mV), 4/4 (-50mV), 8/8 (-40mV), 4/4 (-30mV), 3/8 (-20mV), 5/9 (-10mV), 5/7 (0mV), 4/5 (10mV), 3/4 (20mV). On the other hand, in fed neurones, the relative number of patches best fit with just one exponential was reduced: 7/11 (-60mV), 5/8 (-50mV), 4/8 (-40mV), 3/5 (-30mV), 4/6 (-20mV), 5/5 (-10mV), 3/8 (0mV), 7/7 (10mV), 5/6 (20mV). For a better comprehension of these ratios, Figure 3.17 presents the relative contribution of single ($\tau_{hsingle}$) and double exponential (τ_{hfast} and τ_{hslow}) fits in the patches, at each voltage membrane studied, for fed and fasted neurones.

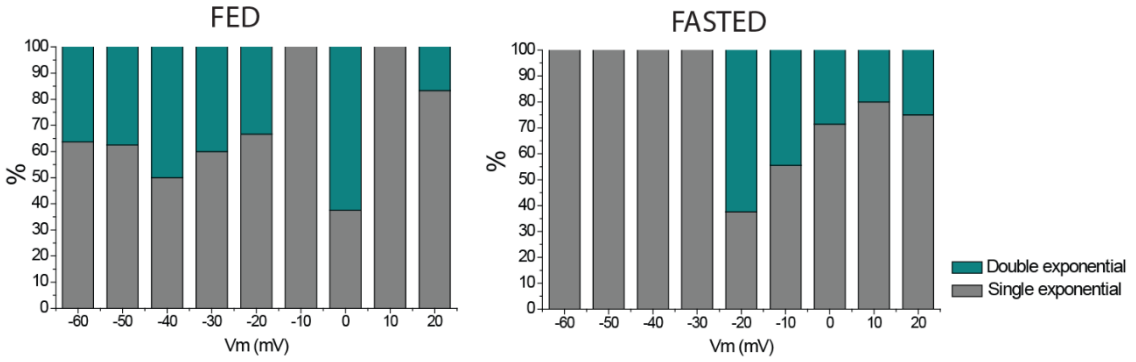

Figure 3.17- ***Fraction of patches (%) with the decay phase of ensemble traces best described by a single (grey bars) or double (green bars) exponential fits, in fed and fasted neurones.***

The stack bars on Figure 3.17 show that in fed neurones two components of inactivation were practically found in all voltage range studied, except for -10mV and 10mV. At potential values between -60 and -30 mV, in fed neurones, there were considerable percentage of patches requiring two exponentials, a tendency that contrast with what was observed in fasted neurones: at the same hyperpolarized potentials (between -60mV and -30mV), all the ensemble averages require only one exponential. Indeed, in fasted neurones, a second component was only seen at potentials more positive than -20mV (including). Overall, these results indicate that the feeding cycle influenced the fraction

of patches with two distinguishable components – τ_{hfast} and τ_{hslow}, an effect more pronounced at more hyperpolarized voltage range (-60mV to -30mV) In other words, a single component is more often found in fasted neurones.

The voltage dependence of the time constant of inactivation, as estimated from ensemble averages, is summarized in Figure 3.18. This analysis allowed to assess the contribution of each component of inactivation in both neurones.

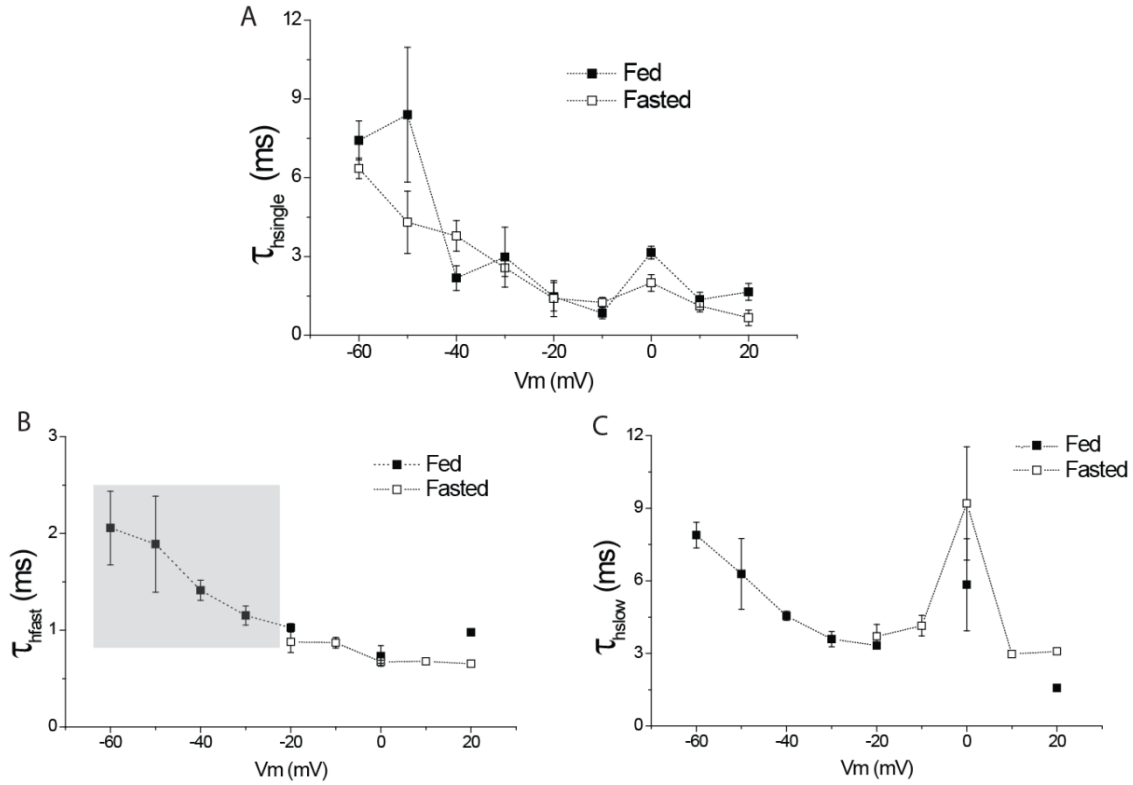

Figure 3.18- ***Effect of the feeding cycle on the voltage dependence of the time constant of inactivation as measured in ensemble averages*** *such as those in Figure 3.16. A) Mean values of the single exponential ($\tau_{hsingle}$) calculated for ensemble average traces best described by one exponential (see Equation 3.4). B) Mean values of fast (τ_{hfast}) and C) slow (τ_{hslow}) components of the decay phase of the signals best fit with two exponentials, as given by Equation 3.4, from fed (filled squares) and fasted (open squares) neurones. Error bars are ±S.E.M. and where no error bars are shown, sample was less than three. The grey box in B) draws attention for the range of voltage steps at which only fed neurones presented data points correspondent to the faster component of inactivation, τ_{hfast}. Indeed, one should note that, at the voltage range between -60mV and -30mV, the mean values of $\tau_{hsingle}$ in fasted neurones is practically superimposed with the mean values of τ_{hslow} of fed neurones, pointing for the exclusiveness of τ_{hfast} in fed neurones at that voltage range. This is consistent with higher channel density in fed neurones, most likely due to the presence of additional channel isoforms with rather fast kinetics of inactivation.*

The values depicted in Figure 3.18A, corresponding to the ensembles that required the fit of a single exponential, resemble the ones verified in the curves of the time-constant of inactivation of whole-cell Na^+ currents. Similar voltage dependence was found which further indicates that the single-channel recordings refer to Na^+ channel openings. Furthermore, despite some apparent discrepancies in some voltages (*e.g.* -50 mV), the

data from fed and fasted neurones presents no significant differences in the voltage range studied ($P > 0.05$).

For the patches that showed two components in the time course of the current decay, the voltage dependence of the τ_{hfast} and τ_{hslow} is presented in figures 3.18B and 3.18C, respectively. As previously observed on whole-cell currents (figure 3.12), τ_{hslow} depicts a greater voltage dependence, in relation to τ_{hfast}. Both graphs show a steady decrease of mean values along the voltage range studied, even considering the observed 'hump' at 0mV. Overall, the graphs in Figure 3.18 point to a lack of influence of the feeding cycle on the kinetics of inactivation of the ensemble currents obtained from patches of fed and fasted neurones. However, at hyperpolarized potentials (between -60mV and -30mV), two observations must be highlighted: a) the curves of $\tau_{hsingle}$ vs. voltage in the fasted neurones and τ_{hslow} vs. voltage in the fed neurones are superimposed and b) the presence of τ_{hfast} is exclusive in fed neurones (Figure3.18B). Altogether, these observations indicate a variation in the channel density throughout the feeding cycle, suggesting that fed neurones have more functional channels when compared to fasted neurones, as indicated by the results obtained from the whole-cell currents.

Qualitatively, the major differences in the decaying phase of the ensemble traces between fed and fasted neurones are presented in the Figure 3.19. The mean pooled response from the same raw data of figure 3.18 was normalized to peak current value, for each of the membrane potentials indicated.

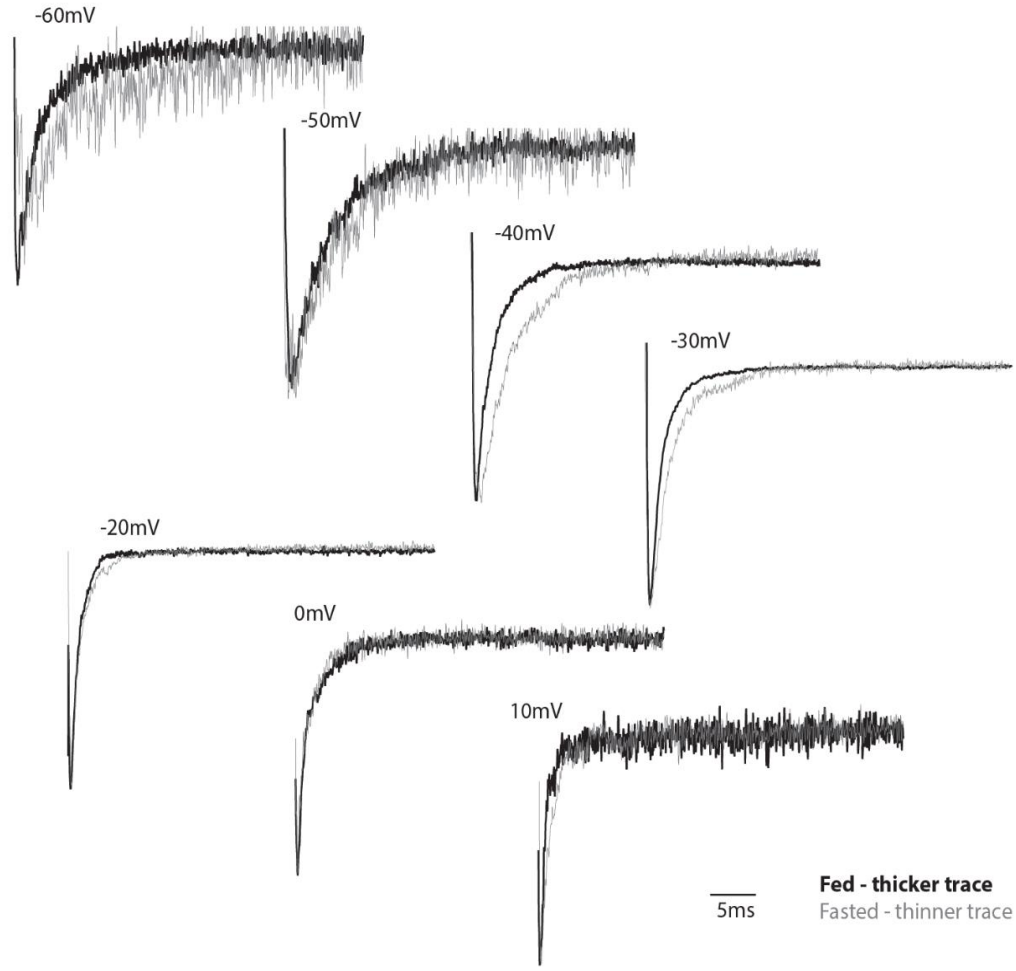

Figure 3.19- ***Pooled ensemble averages (mean values) normalized to peak current values in patches from fasted (thinner grey trace) and fed (thicker black trace) neurones****, obtained in command steps from -60 to 10 mV. For each voltage, the results for fed and fasted neurones were superimposed for comparison.*

In the range from -60mV to -30mV, there was a dominant faster component in fed neurones (more prominent between -40mV and -30mV), which accounts for the sharper drop in the decaying phase observed in the fed neurones. At potentials more depolarized than -20mV the decaying phase of both neurones is essentially overlapped. This result demonstrates that the fast decay observed in fed neurones is dominant over the fast decay of fasted neurones, precisely in the voltage range at which fasted neurones disclose a single exponential. Once again, the exclusive presence of τ_{hf} at hyperpolarized potentials in fed neurones may be accountable for the differences illustrated in Figure 3.19. This is consistent with a greater density of Na^+ channel isoforms with faster kinetics of inactivation in CA1 neurones of fed animals.

3.2.4.3 Na^+ channel expression analysis – western blotting

The likely differential expression of Na^+ channel isoforms in the surface of rat hippocampal neurones was addressed, as a further explanation to the different electrophysiological properties of Na^+ channels.

Plasma membrane-enriched fractions were isolated from hippocampal neurones dissected from fed and fasted animals (see material and methods) and used in western blotting experiments. These samples contained all the neuronal membrane structures, including the plasma membrane where the voltage gated Na^+ channels are functionally located. To detect the presence of $Na_v1.2$, the most common sodium channel isoforms in rat brain (Gordon et al., 1987), PVDF membranes were marked with an antibody raised against the α-subunit (1:2000 dilution) and as a loading control we have used an antibody that recognizes a plasma membrane marker, N-cadherin (1:1000 dilution).

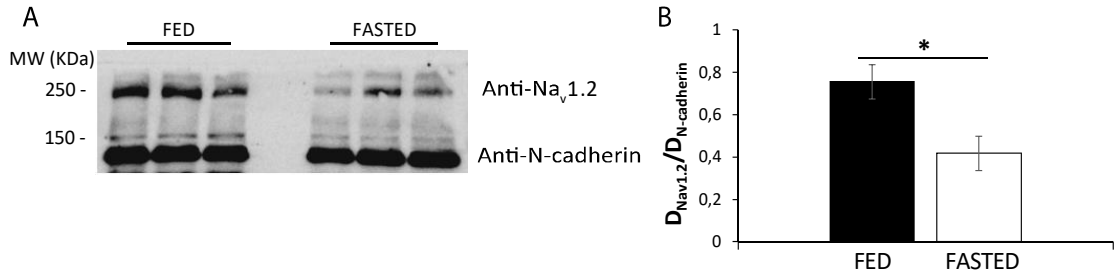

Figure 3.20- ***Expression of rat brain Na^+ channel subtype $Na_v1.2$ in plasma membrane-enriched fractions of hippocampal neurones, from fed and fasted rats.*** *A) Western blotting PVDF membrane marked with antibody raised against $Na_v1.2$ (1:2000) and N-cadherin (1:1000), as a loading control. The first three lanes, on the left, correspond to fed samples and the last three, on the right, to fasted samples. B) Densitometry results obtained by dividing the blot areas measured in ImageLab software (Biorad®). The results are statistically significant (t-student test *0.05<P<0.01, n=3). Error bars are ±S.E.M.*

Figure 3.20A illustrates the effect of feeding cycle on the protein population of rat hippocampal neuronal membranes. The bands located near the 250KDa molecular weight relate to the expression levels of $Na_v1.2$. The first three lanes, on the left, contain the protein extracts of fed rats, suggesting an increased concentration of this isoform in the surface of rat hippocampal plasma membrane when the animals were fed. The quantification of protein expression is shown in Figure 3.20B, confirming the higher levels of $Na_v1.2$ in fed rats. Results are statistically significant ($0.01 < P < 0.05$, n=3).

3.2.4.4 Discussion

The present study aimed at providing data concerning the effect of feeding cycle on sodium (Na^+) currents (I_{Na}) in acutely isolated rat hippocampal CA1 neurones. For such, we developed an integrated analysis of the biophysical and biochemical properties of I_{Na} in neurones of fed and fasted animals.

The significant differences between fed and fasted neurones can be summarized as follows: in fed neurones, the whole-cell currents showed 1) a 1.5-fold increase in average maximum current density values; 2) a hyperpolarizing shift in the voltage dependence of activation curves and a depolarizing shift in the voltage dependence of both 3) steady-state inactivation (h_∞) curve and 4) time-constant of the slow inactivating component (τ_{hslow}). Also, in fed neurones, the single-channel current records displayed 5) higher Na^+ channel unitary current amplitudes and larger conductance mediated through single channels. Finally, western blotting results disclosed 6) an increase in the concentration of a specific Na^+ channel α-subunit, $Na_v1.2$, in plasma membrane-enriched fractions of hippocampus from fed animals.

Considering the voltage dependence of activation curves of Na^+ currents obtained from both conditioned neurones, mean V_h values were significantly different, with fed neurones depicting a hyperpolarizing shift (about 4mV) in comparison to fasted neurones (see Table 3.1). This result indicates an influence of feeding cycle on the conductance of the Na^+ channel population of rat hippocampal CA1 neurones, suggesting a facilitation of the activation process in fed neurones. More specifically, upon feeding, there must be more Na^+ channels opened at more negative membrane voltages, at which the driving force is greater, thus contributing to the higher current density observed in fed neurones. In addition, a more hyperpolarized activation curve lowers the spike voltage threshold, increasing the excitability in hippocampal CA1 neurones of fed animals.

The feeding cycle also influenced the voltage dependence of inactivation of I_{Na}. The V_h parameter of h_∞ in fed neurones showed a significant depolarizing shift by 7mV, in comparison to fasted neurones (see Table 3.1), reflecting an increase of the fraction of activatable channels. Such variation in the voltage dependence of h_∞ is accompanied by a depolarizing shift in the voltage dependence of τ_{hslow} in fed neurones, with slower values obtained at a hyperpolarized voltage range between -45mV and -20mV (see figure

3.12B). In other words, I_{Na} displayed relatively less and slower inactivation in fed neurones in a wide range of potentials, which indicates a greater neuronal excitability after feeding.

By overlapping the activation and inactivation curves, we obtained a voltage range at which the activation occurs when the current is not completely inactivated – 'window current' (French *et al.*, 1990; Ketelaars *et al.*, 2001*a*; Huang *et al.*, 2011). From this analysis, one can estimate that, upon feeding, there are more Na^+ channels available for activation. Again, the larger window current amplitude plus the negative shift observed in its voltage dependence emphasise the thesis of higher state of excitability in fed neurones.

Despite the already mentioned biophysical modifications observed in whole-cell currents, we suggest that the feeding cycle does not play any role over the structure of the voltage-gated Na^+ channels. Such reasoning arises from the analysis of V_s parameter of activation curves, whose output is sensitive to variations in the structure responsible for the gating of the channels - the voltage sensor (Stühmer *et al.*, 1989; Chen *et al.*, 1996). This structure is mainly confined to the positive charged amino acids – arginine residues - embedded in the S4 segments of the channels (Robert Guy & Conti, 1990; Patlak, 1991; Catterall *et al.*, 2005; Bezanilla, 2005). Here, the similarity observed in V_s values between conditions (6.7 ± 0.35 mV/e-fold and 6.8 ± 0.25 mV/e-fold, for fed and fasted neurones, respectively) is an indirect indication that the voltage sensor of the channels might not endure any alteration during the physiological feeding cycle. Accordingly, the number of charges required for the outward movement of the voltage sensor (Armstrong & Bezanilla, 1973; Armstrong & Bezanilla, 1977; Almers, 1978; Yang *et al.*, 1996; Bezanilla, 2000) is expected to be the same in both conditions.

Additional evidence that further suggests the lack of influence of feeding cycle on Na^+ channel structure is brought by the analysis of the voltage dependence of time constant of the fast inactivating component (τ_{hfast}). Fast inactivation is linked to a hinged-lid structure (IFM motif) tethered in the cytoplasmic part of the channel - "ball and chain" model (Bezanilla & Armstrong, 1977; Armstrong, 1981). Here, we clearly showed that τ_{hfast} values of fed and fasted neurones are essentially overlapped (see figure 3.12B), suggesting that the tethered cytoplasmic structures of the Na^+ channels take essentially

the same time to block the pore and completing the fast inactivating mechanism, either in fed and fasted animals.

On the other hand, the already mentioned variations obtained from τ_{hslow} point out to a possible conformational rearrangement of Na^+ channels throughout feeding cycle. Although the slow inactivation is not a fully understood mechanism (Vilin & Ruben, 2001*b*; Goldin, 2003*b*), it is thought to be correlated with conformational alterations at the extracellular pore of the channel (O'Leary *et al.*, 1995; Mickus *et al.*, 1999; Goldin, 2003*b*; Ulbricht, 2005; Silva, 2014). Despite the biophysical interpretation of this outcome is not clear, one may consider alterations in the interaction lipid-protein between the neuronal plasma membrane and the extracellular pore of the channels. Indeed, modifications in the organization and lipid composition of the plasma membrane result in alterations of the fluidity properties of neuronal plasma membrane, which, ultimately might regulate channel functioning (Lee, 2006; Schmidt *et al.*, 2006; Schmidt & MacKinnon, 2008; Dart, 2010; Jiang & Gonen, 2012; Kasimova *et al.*, 2014; Poveda *et al.*, 2014, 2017).

We have sought for possible underlying mechanisms that could account for the biophysical differences described here for the whole-cell currents of fed and fasted neurones. In this regard, we have exploited two possibilities: alterations on Na^+ single-channel activity and in channel density throughout the feeding cycle. These two approaches would be most valuable to provide further mechanistic insights on how feeding led to changes observed in whole-cell currents.

Accordingly, single-channel recordings were performed using the excised inside-out patch configuration. Unitary current amplitudes were measured by fitting all-points amplitude histograms with Gaussian curves. Fed neurones contained patches with higher current amplitude, suggesting an influence of feeding cycle over the unitary conductance. The calculated slope conductance for fed neurones was 16.7 pS, being consistent with the 16.6 pS value obtained in a previous study in rat hippocampal CA1 cells (Fernandes *et al.*, 2001). The lower average single-channel conductance obtained for fasted neurones (12.6 pS) indicates an impact of feeding on the single-channel conductance: each Na^+ channel present at the surface of rat hippocampal CA1 neurones conducts more Na^+ ions through its pore during the post-prandial period, corroborating the results observed in the activation curves of whole-cell currents. There was indeed positive correlation between

the ensemble traces obtained from sweeps with single-channel openings and the whole-cell currents, confirming the nature of such openings as being Na^+ channel events.

Furthermore, the observed distinct behaviour of macroscopic currents may also be explained by variation in the number of functional Na^+ channel isoforms at the plasma throughout the feeding cycle. In the light of this argument, the analyses regarding the whole-cell current density and window current can be interpreted as a result of augmented expression levels of Na^+ channels in fed neurones. Moreover, the ratio of the components of time constant of inactivation (a_f/a_s) reflects a dominance of fast component proportion in both conditions, which, ultimately, highlights the presence of channels with rather faster kinetics, typically found in brain cells (Westenbroek *et al.*, 1989; Vacher *et al.*, 2008; Leterrier *et al.*, 2010). In this regard, $Na_v1.2$, a fast inactivating channel, seemed like a reliable candidate to address this question, as it comprises approximately 70% of the total rat brain Na_v α-subunit pool (Gordon *et al.*, 1987). Thus, any alteration in the surface expression of Na^+ channel populations determined by the feeding cycle, would most likely involve the $Na_v1.2$ isoform.

Indeed, the western blotting experiments, run in plasma membrane-enriched fractions of rat hippocampus, validated this hypothesis, pointing to a higher concentration of $Na_v1.2$ at the surface of hippocampal neurones of fed animals. Hence, the $Na_v1.2$ isoform underwent a differential surface expression whether animals have eaten or not. Although the survey of $Na_v1.2$ isoform has been conducted on the entire tissue of rat hippocampus, one may assume that these results are representative of what happens in the neurones of CA1 subfield, where the electrophysiological experiments were carried out.

The backdrop outlined here of increased neuronal excitability upon feeding is reinforced with higher $Na_v1.2$ density at the plasma membrane. The cellular localization of $Na_v1.2$ channels in the central nervous system neurones – proximal Axon Initial Segment (AIS) –, as well as their physiological function at ensuring action potential backpropagation, make them major players in the modulation of the threshold for the generation of somatodendritic potentials (Westenbroek *et al.*, 1989; Ahn *et al.*, 2007; Hu *et al.*, 2009). Hence, it is plausible to consider that a greater channel density may result in a reduction of action potential threshold in fed neurones, which, *per se*, promotes hyperexcitability.
The possibility of other channel isoforms being overexpressed after feeding should be also considered. For example, the $Na_v1.1$ isoform might be involved in this tidal

regulation of channel expression, as the single-channel conductance value of fed neurones resembles the one obtained for SCN1A expressed in HEK-293 cells (17pS; Vanoye *et al.*, 2006). Hence, one can predict a larger number of $Na_v1.1$ channels at the surface of the soma of hippocampal neurones from fed animals. Indeed, considering the mean pooled ensemble-average currents obtained in the voltage range from -60mV to -30mV (figure 3.19), major differences were found in the decaying phase of the signal in fasted and fed neurones. The higher proportion of τ_{hfast} in fed neurones (sharper drop in the decaying phase) can be attributed to the major contribution of $Na_v1.1$ isoform, which is known for its fast-kinetic properties (Goldin, 1999; Catterall *et al.*, 2005*a*; Eijkelkamp *et al.*, 2012).

In summary, the present study provides evidence for the impact of the feeding cycle on the functioning of Na^+ currents/channels of central pyramidal neurones, mainly confined to the CA1 region of rat hippocampus. By correlating information obtained from electrophysiology with those obtained with molecular biology methods, we conclude that there is a rapid and reversible adjustment of the biophysical and molecular characteristics of I_{Na} to variations of metabolism brought up by the feeding cycle. The differentiated response under fed *vs.* fasted conditions suggest an increase in intrinsic neuronal excitability upon feeding. Such increase of excitability is likely to involve a consequent enhancement of calcium dynamics in CA1 neurones upon feeding. Our results are consistent with changes in the Na^+ channel density of rat hippocampal neurones, which, at some extent, can explain the voltage shifts observed in activation and inactivation curves (both, h_∞ and τ_{hslow}) in fed neurones. Furthermore, the greater current density observed in fed neurones can be justified by the combination of a greater channel density with a higher single-Na^+ channel conductance, leading to a signal amplification of the whole-cell current output. Additionally, the results concerning the V_s parameter and τ_{hfast} suggest that feeding cycle does not determine any structural effect upon the regions responsible for the voltage sensor and fast inactivation of the channels, respectively, whereas changes in τ_{hslow} may indicate conformational alterations in the outer pore of the Na^+ channels.

The results disclosed a new perspective of the interplay between feeding and the hippocampus. The biophysical and biochemical modifications brought by the feeding cycle may elect voltage-gated Na^+ channels as molecular references in the role of hippocampus as a processor of satiety information (Hebben *et al.*, 1985; Higgs, 2002; Davidson *et al.*, 2005, 2009, Henderson *et al.*, 2013, 2016; Parent *et al.*, 2014; Hsu *et al.*,

2015; Jacka *et al.*, 2015; Parent, 2016*b*; Hannapel *et al.*, 2017; Kanoski & Grill, 2017). Thus, when to eat, or how much to eat in any one meal are decisions that may rely on the functioning of Na^+ channels present at the surface of the hippocampus. Speculating, one might regard Na^+ channels as new players in the context of food ingestion-related conditions - overweight and obesity – and metabolic disorder, such as diabetes.

3.3 Voltage-gated Ca^{2+} channels

3.3.1 Calcium signaling in the brain

Calcium (Ca^{2+}) is the widely known universal second messenger that regulates the most important activities of all eukaryotic cells. Ca^{2+} ions are key players in enabling excitable cells to translate their electric excitation into other forms of physiological activity. In neurones, by influencing membrane depolarization (thereby activating other voltage-gated ion channels), regulating gene expression and controlling the release of neurotransmitters from the presynaptic terminals, Ca^{2+} has been shown to influence both long-term potentiation (LTP) and long-term depression (LTD) (Eccles, 1983; Voronin, 1983; Grover & Teyler, 1990; Bliss & Collingridge, 1993; Stanton, 1996; Kawamoto *et al.*, 2012; Brini *et al.*, 2014; Simms & Zamponi, 2014; Zamponi, 2015). Neurones have thus developed extensive and intricate Ca^{2+} signaling pathways to couple the Ca^{2+} signal to their biochemical machinery (Figure 3.21). Given the evidence, Ca^{2+} plays pivotal roles in controlling neuronal excitability, not only within individual neurones, but also among large populations of neurones that comprise neuronal networks (Gleichmann & Mattson, 2011).

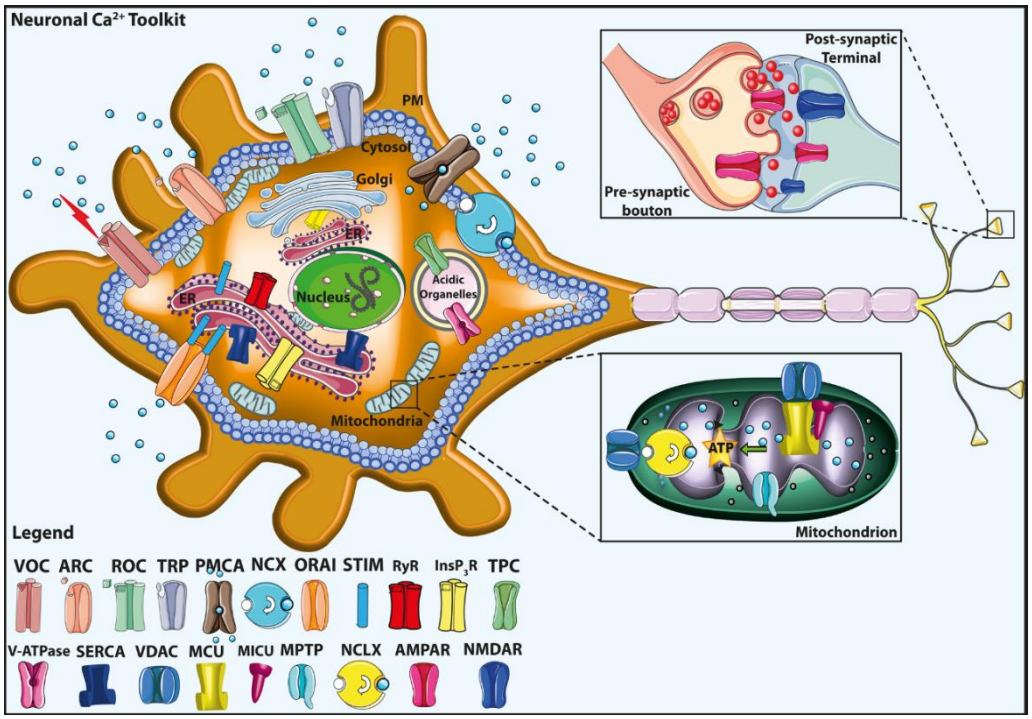

*Figure 3.21- **Neuronal calcium (Ca^{2+}) signaling toolkit**. The Ca^{2+} transport proteins, the receptors of the plasma membrane (PM), and the intracellular organelles, including mitochondria, endoplasmic reticulum (ER), Golgi apparatus, and acidic organelles, are indicated. The mitochondrial Ca^{2+} handling systems (proteins) are shown in greater detail in the bottom right inset. The top right inset shows a schematic view of the pre-synaptic bouton and the post-synaptic termination. The legend on the bottom left indicates the Ca^{2+} transporter proteins. VOC Voltage-gated Ca^{2+} channel, ROC receptor-operated Ca^{2+} channel, ORAI the pore-forming subunit of store-operated Ca^{2+} entry channel (SOC), STIM the Ca^{2+} sensor, TPC two-pore channel, ARC arachidonic acid-regulated Ca^{2+} channel, TRP transient receptor potential channel, PMCA plasma membrane Ca^{2+} ATPase, V-ATPase vacuolar H+ ATPase, InsP3R inositol 1,4,5 tris–phosphate receptors, RyR ryanodine receptor, NCX plasma membrane Na+/Ca^{2+} exchanger, SERCA sarco-/endoplasmic reticulum Ca^{2+} ATPase, MCU mitochondrial Ca^{2+} uniporter, MICU mitochondrial Ca^{2+} uniporter regulator, NCLX mitochondrial Na^{+}/Ca^{2+} exchanger, VDAC voltage-dependent anion channels, MPTP mitochondrial permeability transition pore, AMPAR 2-amino-3-hydroxy-5-methyl-4-isoxazolepropionic acid receptor, NMDAR N-methyl-d-aspartate receptor (Brini et al., 2014)*

While Ca^{2+} regulation is essential to any cell, it is obvious that in neuronal cells the connection between electrochemical ion gradients and biochemical regulatory pathways is of special importance. For such, there must be a tight regulation of intracellular Ca^{2+} concentration ($[Ca^{2+}]_i$), which is accomplished, among other homeostatic mechanisms, by ion channels and ATP-dependent exchangers and pumps (Figure 3.21). Indeed, it has been suggested that once cells opted to use high-energy phosphate compounds as metabolic currency, they faced great evolutionary pressure to maintain an unusually low $[Ca^{2+}]_i$ (< 100 nM) (Tsien & Barret, 2013). Otherwise, salts of calcium and phosphate would precipitate, turning the cytosol into a bone-like solid (Williams, 1970). The 10,000-fold concentration gradient (extracellular $[Ca^{2+}]$ ~1.2mM) makes Ca^{2+} special when compared with the more abundant cations Na^{+} and K^{+}, as it leads to a significant locally increase in $[Ca^{2+}]_i$ with only a small Ca^{2+} flux across the cell membrane (Clapham, 2007), whereas influx of Na^{+} and efflux of K^{+} significantly affect the membrane potential, but cause only relatively minor changes in cytosolic ion concentration (Brini *et al.*, 2014). The $[Ca^{2+}]_i$ increase is the call to action. A good rule of thumb is that Ca^{2+} acts locally, in the vicinity of the channels that delivery it (Hille, 2001).

As a broad generalization, excitable cells translate their electricity into action by Ca^{2+} fluxes modulated by voltage-sensitive, Ca^{2+}-permeable channels. Combining the ideas of Ca^{2+} as a chemical messenger and change in membrane as an initiator of Ca^{2+} influx brings us to the essence of the advantages offered by voltage-gated Ca^{2+} channels (Tsien & Barret, 2013). Ca^{2+} channels in the plasma membrane have an added advantage relative to channels in intracellular membranes, in that they have access to the plasma membrane's voltage potential, a global indicator of cellular activity. A rapid, voltage-dependent

closing of the channel allows for dissipation of the message by diffusion and strong, rapid local buffering, thereby achieving spatio-temporally precise signaling (Tsien & Barret, 2013). Furthermore, signal transduction in different cell types involves different molecular subtypes of voltage-gated Ca^{2+} channels (VGCC), which mediate voltage-gated Ca^{2+} currents with different physiological, pharmacological, and regulatory properties.

3.3.2 Voltage-gated Ca^{2+} channel - Diversity and classification schemes

Without Ca channels our nervous system would have no outputs (Hille, 2001).

VGCCs were first identified in the 1950s (Fatt & Katz, 1953). Since then, multiple types of VGCCs have been measured directly in a variety of cell types from vertebrate and invertebrate organisms. Their classification and nomenclature has been made according to various schemes, based on electrophysiological, pharmacological and biochemical/molecular observations.

Firstly, they were distinguished by their potential of activation, which enabled VGCC in falling into two major categories: high voltage-activated (HVA) channels that open in response to large membrane depolarizations (with a threshold positive to approximately −30mV) and low voltage-activated (LVA) channels that only need a small depolarization to be activated (threshold activation at a membrane voltage positive to −70 mV) (Hagiwara *et al.*, 1975; Llinas & Yarom, 1981; Carbone & Lux, 1984; Armstrong & Matteson, 1985; Yaari *et al.*, 1987).

Following the establishment of advanced technology, such as patch-clamp techniques, the next stage of the classification resulted from the combination of phenomenological parameters including biophysical and pharmacological properties. In what concerns the investigation upon vertebrate neurones, the LVA channels were further classified as T channels and the HVA channels were subdivided into two classes – L and N channels. This common classification of neuronal Ca^{2+} channels was named by Tsien and colleagues (Tsien *et al.*, 1988), following their study on DRG neurones (see table 3.4).

Table 3.4- types of voltage-gated Ca^{2+} channels in vertebrates. Electrophysiological and pharmacological characteristics. Taken from (Hille, 2001)

	Slow, persistent	Fast, inactivating	
	HVA	HVA	LVA
Tsien type[a]	L	P/Q, N, R	T
Snutch gene class[b]	S, C, D, F	A, B, E	G, H, I
Structural nomenclature[c]	$Ca_v1.1$, 1.2, 1.3, 1.4	$Ca_v2.1$, 2.2, 2.3	$Ca_v3.1$, 3.2, 3.3
Activation range[d]	Positive to –30 mV	Positive to –20 mV	Positive to –70 mV
Inactivation range	–60 to –10 mV	–120 to –30 mV	–100 to –60 mV
Inactivation[e]	Very slow ($\tau > 500$ ms)	Partial ($\tau \approx 50$–80 ms)	Complete ($\tau \approx 20$–50 ms)
Deactivation rate[f]	Rapid	Slow	Rapid
Single-channel conductance[g]	25 pS	13 pS	8 pS
Single-channel openings	Continual reopening	Long burst	Brief burst, inactivation
Relative conductance	$Ba^{2+} > Ca^{2+}$	$Ba^{2+} > Ca^{2+}$	$Ba^{2+} = Ca^{2+}$
Divalent block	$Cd^{2+} > Ni^{2+}$	$Cd^{2+} > Ni^{2+}$	$Ni^{2+} > Cd^{2+}$
ω-CTX GVIA block[h]	No	Strong for $Ca_v2.2$	No
Dihydropyridine sensitivity[i]	Sensitive	Resistant	Resistant

T channels are described as having fast current decays, with a small amplitude of single channel conductance during a sustained depolarization ('T' stands for *t*iny conductance and *t*ransient current). Due to their low threshold of activation, they are not seen when a cell is maintained at depolarized holding potentials. L channels, the first HVA subtype being biochemically purified and cloned (Curtis & Catterall, 1984), show large-single channel conductance amplitude and slow kinetics of current decay during a sustained depolarization ('L' stands for *l*arge and *l*ong-lasting). They can be recorded in isolation from T-type currents by starting from depolarized holding potentials (Hille, 2001). Pharmacologically, L-type channels are defined by their sensitivity to 1,4-dihydropyridine (DHP) drugs, a wide class of drugs with either inhibitor (nifedipine, nisoldipine, isradipine) or activator (Bay K 8644) action on the channel (Lipscombe, 2002; Helton, 2005). Novel calcium channels, insensitive to DHPs and with single-channel conductance between those of T-type and L-type channels, were revealed in experiments with neuronal cells (Nowycky *et al.*, 1985; Carbone & Lux, 1987; Fox *et al.*, 1987*a*, 1987*b*). These channels were named N-type Ca^{2+} channels (N for *n*euronal). The availability of blocking agents that target L- and N-type channels revealed other HVA

currents. It was shown that neuronal non-L-type channels could be further classified into subtypes according to their sensitivity to peptide toxins isolated from cone snails and spiders. The channel sensitive to ω-conotoxin GVIA, kept the name N-type channel, whereas the channel sensitive to ω-Aga IVA toxin was named P/Q-type calcium channel (P for Purkinje cells, where this channel was characterized (Llinas *et al.*, 1989)). The channels resistant to these toxins were named R-type calcium channel (R for resistant) (Lacinová, n.d.). Except for their pharmacology, N-, P/Q-, and R-types of Ca^{2+} channels seem functionally similar, disclosing variable degrees of inactivation (Fox *et al.*, 1987*a*, 1987*b*) and modulation by G-protein-coupled receptors (Hille, 2001).

The original classification system of Ca^{2+} channels, which was expanded from the simple LVA/ HVA dichotomy to encompass T-, L-, N-, P-/Q-, R-channels, was subsequently found to be too restrictive to adequately describe all types of Ca^{2+} channels. The nomenclature currently used for calcium channels terminology was proposed based on molecular biological approaches, and specifically, on the amino acid and gene sequence of the pore-forming α_1 subunit ($Ca_v\alpha_1$) (Ertel *et al.*, 2000) (Figure 3.22).

The pharmacological and electrophysiological diversity of calcium channels arises primarily from the existence of multiple α1 subunits (Hofmann *et al.*, 1994), encoded by at least 10 distinct genes (Table 3.4 and Figure 3.22B), organized into three distinct subtypes of VGCCs in animals- Ca_v1, Ca_v2, and Ca_v3 (Catterall *et al.*, 2005*b*).

The Cav1 channel family encodes three different neuronal L-type channels (termed $Ca_v1.2$, $Ca_v1.3$, and $Ca_v1.4$) plus a skeletal muscle-specific isoform, $Ca_v1.1$ (Simms & Zamponi, 2014). In the mammalian brain, $Ca_v1.2$ and $Ca_v1.3$ are the predominant forms of L-type Ca^{2+} channels. They are localized in the cell bodies and proximal dendrites, both at presynaptic as well as postsynaptic locations (Lipscombe & Andrade, 2015). Hippocampal function appears to depend more on $Ca_v1.2$, which, by promoting large influx of Ca^{2+}, initiates downstream protein kinase pathways that promote gene transcription required for long-term synaptic plasticity (long-term potentiation) (Westenbroek *et al.*, 1990; Thibault & Landfield, 1996; Bowden *et al.*, 2001; Striessnig *et al.*, 2015; Zamponi *et al.*, 2015).

The Ca_v2 channel family includes three members ($Ca_v2.1$, $Ca_v2.2$, and $Ca_v2.3$) localized at presynaptic terminals, dendrites and cell bodies (Westenbroek *et al.*, 1992), mainly responsible for the release of neurotransmitters, like glutamate, γ- aminobutyric acid

(GABA), and acetylcholine. Through alternative splicing and assembly with specific ancillary subunits, $Ca_v2.1$ gives rise to P- and Q-type channels. $Ca_v2.2$ encodes N-type channels and $Ca_v2.3$ corresponds to R-type channels (Simms & Zamponi, 2014).

The Ca_v3 channels are represented by three subtypes ($Ca_v3.1$, $Ca_v3.2$, and $Ca_v3.3$), all T-type calcium channels (Perez-reyes, 2003). They have been detected both on and near the soma and at more distal dendritic sites of neurones throughout all brain regions, including hippocampus. Ca_v3 families are mainly involved in triggering low-threshold spikes, which in turn generates a burst of repetitive firing of action potentials mediated by Na^+ channels (Perez-reyes, 2003).

3.3.3 Subunits of VGCCs - Structure

Studies based on biochemical and molecular analyses (Curtis & Catterall, 1984) provide structural differences between HVA and LVA channels (Figure 3.22A). HVA channels are hetero-multimeric protein complexes that are formed through the co-assembly of a functional pore-forming $Cav\alpha_1$ subunit, plus ancillary $Ca_v\beta$, $Ca_v\alpha_2\delta$ and $Ca_v\gamma$ subunits, whereas LVA channels appear to lack these ancillary subunits (Catterall, 2011). The associated α_2, β, γ, δ subunits have auxiliary functions, including the control of channel expression and the modulation of current kinetics. The β subunits greatly enhance cell-surface expression of the α_1 subunits and shift their kinetics and voltage dependence (Catterall, 2000*b*; Brini *et al.*, 2014).

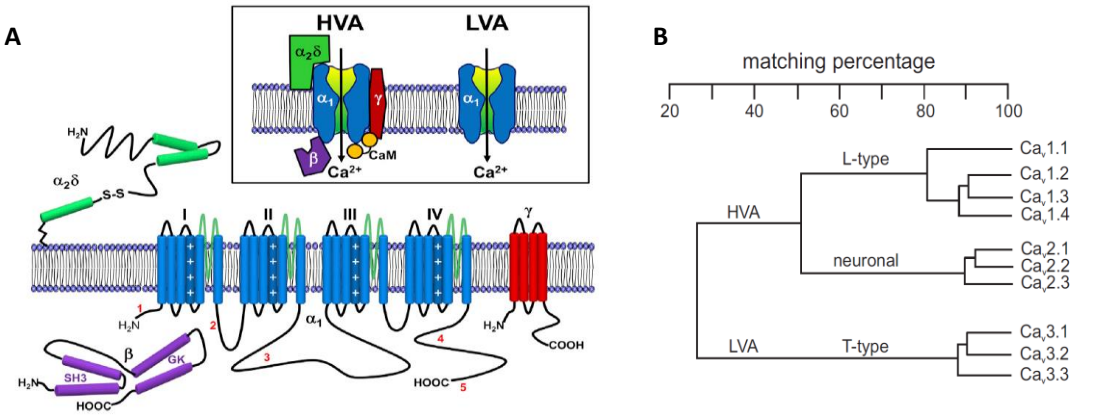

Figure 3.22- ***A) Subunit Composition and Transmembrane Topology of Voltage-Gated Calcium Channel Subunits.*** *HVA channels are heteromultimers comprised of a pore-forming Cavα$_1$ subunit that co-assembles with ancillary Cavβ, Cavα$_2$δ, and possibly Cavγ subunits, plus calmodulin (CaM); LVA channels on the other hand function as Cavα$_1$ subunit monomers. The Cavα$_1$ subunit is comprised of four major transmembrane domains (I–IV) that are connected by cytoplasmic linkers. Each of these domains contains six membrane-spanning helices, plus a re-entrant pore loop (shown in green). The fourth transmembrane segment in each domain contains positively charged amino acids in every third position and forms the voltage sensor. Key protein interaction sites with the Cavα$_1$ subunits are indicated by numbers. Adapted from (Simms & Zamponi, 2014). B) Evolutionary tree of all known VGCCs, considering just the amino acid sequences of α$_1$ subunits. An early evolutionary event separated the α$_1$ subunits into LVA and HVA channels, with less than 30% of sequence homology. A later evolutionary event divided HVA channels into two subfamilies: L-type and neuronal types, with about 50% sequence homology. Individual members of both subfamilies share more than 80% of sequence homology. Adapted from* (Lacinová, n.d.).

The α_1 subunit is a 190- to 250-kDa transmembrane protein composed by four repeat domains (I–IV), each containing six transmembrane α helices (S1–S6), homologous to those found in voltage-gated Na^+ channels (Catterall, 2000*a*). The S4 segments of each domain comprise some positively charged residues, serving as the voltage sensors for activation, moving outward and rotating under the influence of the electric field and initiating a conformational change that opens the pore. A re-entrant P loop motif between S5 and S6 forms the pore lining of the VGCCs. Each of the P loop regions contains highly conserved negatively charged amino acid residues (in the case of HVA channels, glutamic acids) that cooperate to form a pore that is highly selective for permeant cations such as calcium, barium, and strontium (Simms & Zamponi, 2014). The cytoplasmic linker regions of the α1subunit contain sites that are substrates for phosphorylation and interaction with regulatory proteins, and the intracellular carboxyl (C)-terminal region contains a binding site for calmodulin (CaM), which mediates Ca^{2+}-triggered inactivation of the channel upon prolonged membrane depolarization (Hering *et al.*, 2005; Dolphin, 2009; Catterall, 2011). All Ca^{2+} channels share these general structural features.

3.3.4 VGCC distribution in rat hippocampal CA1 neurones

Many of the properties of the Ca^{2+} channels recorded from hippocampal CA1 neurones – single-channel conductance and pharmacological response - are reminiscent of those reported for the multiple types of channels described first in peripheral neurones (Kay & Wong, 1987; Ozawa *et al.*, 1989; Takahashi *et al.*, 1989; Fisher *et al.*, 1990; Toselli &

Taglietti, 1990; Kay, 1991; O´Dell & Alger, 1991; Thompson & Wong, 1991; Wong & Stewart, 1992).

To date, at least 5 types of Ca^{2+} channels have been described in rat hippocampal CA1 neurones – T-, L-, N-, P-/Q- and R- channels (Takahashi *et al.*, 1989; Toselli & Taglietti, 1990; Magee & Johnston, 1995*a*; Igelmund *et al.*, 1996; Porter *et al.*, 1997). The subcellular distribution of these channels is one of the main factors that determines their effectiveness in supporting different neuronal functions. The extensive dendritic arborizations of CA1 pyramidal neurones results in tens of thousands of widely distributed synaptic inputs, most of which are both physically and electrotonically distant from the soma (Andersen *et al.*, 2007). The integration of these synaptic inputs depends to a considerable extent on the expression of voltage-gated channels in different regions of the neuronal membrane.

In rat hippocampal CA1 pyramidal neurones, the density of both low- and high-threshold Ca^{2+} channels throughout the extent of longitudinal somatodendritic axis may be constant (Magee & Johnston, 1995*a*, 1995*b*). However, substantial differences in the type of channels can be found within the somatic and dendritic regions of these neurones, with a trend for more HVA channels to be encountered in the soma and proximal dendrites and more LVA channels to be detected in more distal dendrites (Figure 3.23).

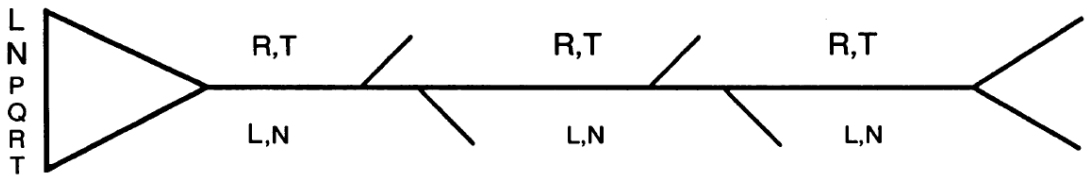

Figure 3.23- ***Schematic representation of the Ca^{2+} channel distribution in the soma and apical dendrites of hippocampal CA1 neurones****. Relative densities of different channel types are represented by font size. Taken from Magee & Johnston (1995).*

L- and N-type channels are mainly found in the soma of CA1 neurones, which is consistent with somatic patch-clamp recordings taken from CA1 neurones (Ozawa *et al.*, 1989; Takahashi *et al.*, 1989; Fisher *et al.*, 1990; Thompson & Wong, 1991) and with antibody-binding imaging studies for L- and N-type Ca^{2+} channels, which indicated the highest density of these channels in the somatodendritic compartment (Westenbroek *et al.*, 1990; Pravettoni *et al.*, 2000; Bowden *et al.*, 2001; Leitch *et al.*, 2009). Nevertheless, a lower expression level of L- and N- type channels is likely to be found at the distal

regions of the apical dendrites. Although no data are available regarding the subtypes of Ca^{2+} channels in CA1 axons, pharmacological studies of synaptic transmission and presynaptic Ca^{2+} entry indicate that N-, P-, Q-, and R-type Ca^{2+} channels are most abundant in other axon terminals of the hippocampus (Andersen *et al.*, 2007).

On the other hand, T-type channels are primarily localized in the apical dendrites. At this point, it is relevant to highlight that the expression of T-type channels in rat hippocampal CA1 neurones undergoes changes during the developmental stages of the animals. In fact, it has been established that T-type channels are mostly found on neurones isolated from neonatal animals (O´Dell & Alger, 1991; Thompson & Wong, 1991; Campbell *et al.*, 1996; Kortekaas & Wadman, 1997; Porter *et al.*, 1997; Ribeiro & Costa, 2000). One possible explanation might be enclosed in a displacement of the expression of T-type channels within the neuron, in the course of maturation. In CA1 pyramidal neurones of very young animals, T-type channels might be distributed throughout the neuron and, as the animal matures, these channels may become primarily localized to the dendritic arborizations (Magee & Johnston, 1995*a*)

3.3.5 Influence of feeding cycle on neuronal Ca^{2+} currents

Given the pivotal importance of voltage-gated Ca^{2+} channels outlined in the introductory sections, the present section gains relevance as it focuses on the oscillations of the activity of such channels throughout the feeding cycle.

3.3.5.1 Whole-cell voltage clamp recordings

Features of the currents

The present section comprises data concerning the influence of feeding cycle in the characteristics of whole-cell voltage clamp Ca^{2+} currents of rat hippocampal CA1 neurones. Ca^{2+} currents were evoked with a step of depolarized voltages from -60mV up to +30mV (increments of 10mV), following a conditioning pulse of -120mV to remove inactivation. Holding potential was set at -70mV (Figure 3.24). With these protocol, both high-voltage activated (HVA) and low-voltage activated (LVA) currents could be recorded (Vreugdenhil & Wadman, 1992; Kortekaas & Wadman, 1997; Ribeiro & Costa, 2000).

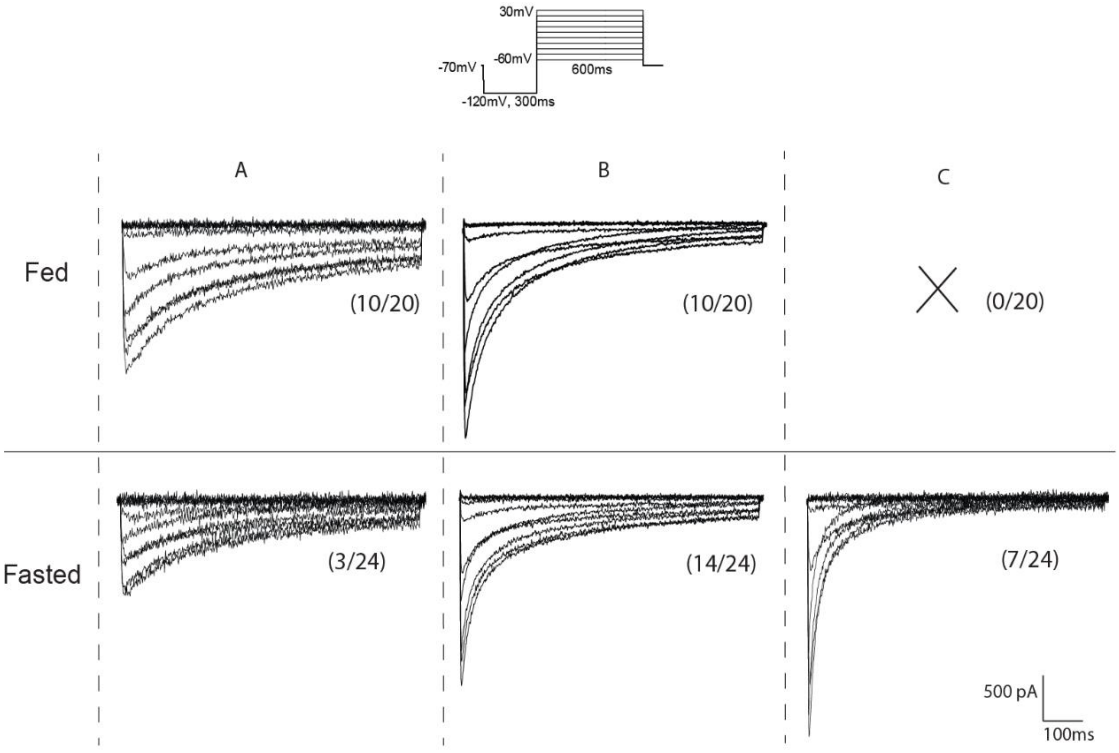

Figure 3.24- ***Effect of feeding cycle over the calcium currents of acutely isolated rat CA1 hippocampal neurones.*** *Whole-cell voltage clamp Ca^{2+} currents, recorded in neurones from fed and fasted animals, were evoked in series of depolarization command pulses (600ms in duration), in steps of 10mV, from -60mV to +30mV, following a hyperpolarizing conditioning pulse at -120mV (300ms in duration). Holding potential was set at -70mV (see inset). Traces are representative recordings of the 3 types of Ca^{2+} current traces observed in fed (n=20) and fasted (n=24) neurones, here termed 'A', 'B' and 'C' (see description in the text). The quantitative distribution of each type of current trace within both conditions is indicated.*

The records depicted in Figure 3.24 illustrate 3 types of currents, here termed currents 'A', 'B' and 'C' (or, alternatively, 'A-, B-, C-type currents') with distinct properties in terms of kinetics of inactivation and a differential distribution between fed and fasted neurones. Current 'A' was characterized by its slow kinetics, with a minimal contribution of the transient component, and with a prominent slow-inactivating component (here termed 'sustained current') at the end of the 600ms command pulse. Current 'B' had faster kinetics, with the current decay better described by two components – fast and slow – and a sustained current with smaller amplitude. Current 'C' had the fastest kinetics, with a sharper decay of inactivation and a sustained current barely detected, envisaging a greater proportion of the fast component in relation to the slow component. The sorting of these currents was a result of visual examination, based on the characteristics described above. In order to avoid biased results, any currents with ambiguous inactivation profiles were labelled as being 'B'-type currents.

The expression of these currents was found to be different between fed and fasted neurones. Current A was present in both conditions, however more often in fed neurones: 10/20 recordings from fed neurones, as oppose to only 3/24 for fasted neurones. Current B was evenly observed between the two conditions: 10/20 recordings assigned to fed neurones and 14/24 assigned to fasted neurones. Finally, current C was only found in fasted neurones, with 7 recordings registered (7/24).

Voltage dependence of activation

The existence of a sustained current, more prominent in the A-type current, prompted an analysis of the voltage-dependence of both, the peak current and at the end of the 600ms pulse, as a measure of the sustained current (Figure 3.25A).

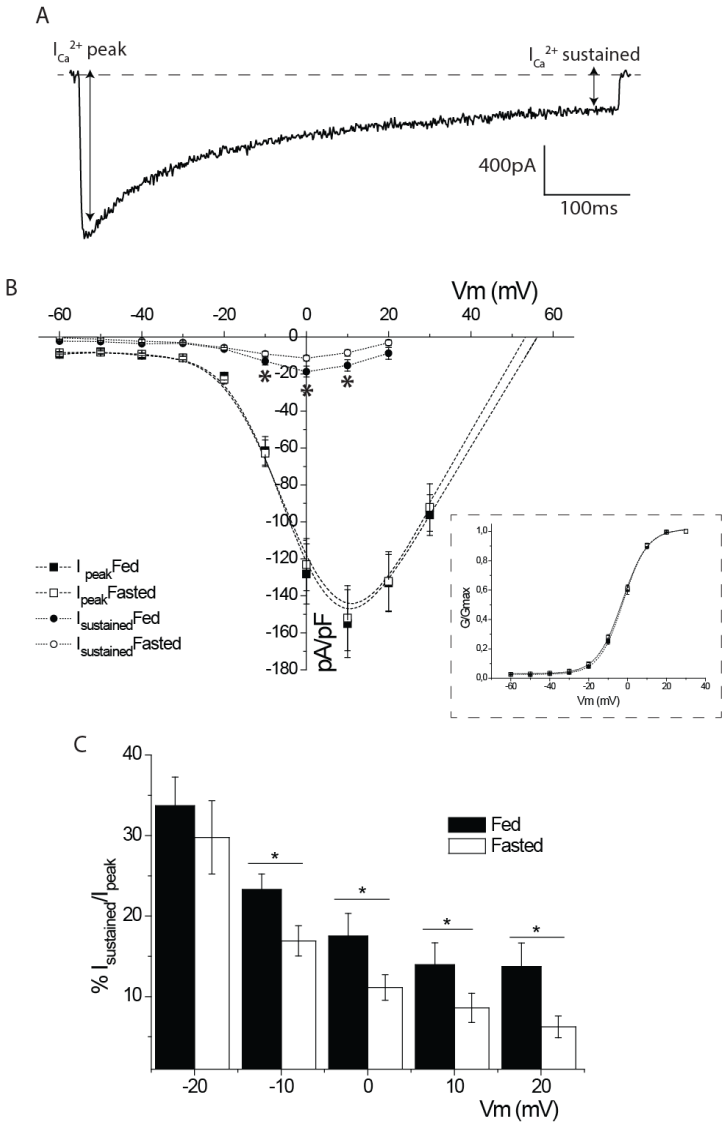

Figure 3.25- ***Influence of the feeding cycle on the amplitude of Ca^{2+} currents taken at the peak of the traces (peak current) and at the end of the 600ms pulse (sustained current)****. A) Illustrative trace indicating where the analysis was undertaken. Dashed line represents zero current. B) I-V curves of mean Ca^{2+} peak (squares) and sustained (circles) currents normalized to cell capacitance (pA/pF), obtained from freshly isolated rat hippocampal CA1 neurones of fed (filled symbols; n=20) and fasted (open symbols; n=24) animals. I-V curves relate to Ca^{2+} currents like those depicted in figure 3.24. The dashed lines are trend lines for a better comprehension of the data. The inset depicts the mean conductance normalized to the maximum value (G/G_{max}) of Ca^{2+} peak currents. There is no shift in the voltage-dependence of activation curves, as V_h values are similar in both conditions (-2.1 ± 0.82 and -2.9 ± 0.60, for fed and fasted neurones, respectively). Dashed lines are the solution of Equation 3.3. C) Relative contribution of Ca^{2+} sustained current to the overall Ca^{2+} current is shown by plotting the mean amplitude of the sustained current as a percentage of the mean peak current, obtained in the voltage range between -20mV and 20mV. Error bars are ±S.E.M. values (t-student analysis *0.01<P<0.05).*

Figure 3.25B depicts the current to voltage (*I-V*) relationship, whose data comprises the mean values of peak (I_{peak}) and sustained ($I_{sustained}$) Ca^{2+} current amplitudes (pA), normalized to the cell capacitance (pA/pF), as a measure of current density, obtained in the voltage range studied (-60mV to +30mV). From the data points concerning I_{peak}, one can ascertain a common feature upon the heterogeneity of Ca^{2+} currents illustrated in Figure 3.24, *i.e.*, there is a dominant high-voltage activated (HVA) component, since peak

Ca^{2+} currents were activated with a threshold higher than -30 mV, with a mean maximum amplitude attained around 10 mV, either for fed and fasted neurones.

The mean current density, taken at the peak of the traces, shows no differences between fed and fasted neurones (-155.0 ± 18.27 pA/pF, n = 20, and -152.1 ± 17.53 pA/pF, n = 24, respectively). Peak current values were converted to conductance via the relationship $G = I/(V_m - E_{Ca^{2+}})$ where V_m is the step command voltage and $E_{Ca^{2+}}$ the reversal potential estimated from the extrapolation of the rising phase of the *I-V* curves. The voltage dependence of activation of peak current was studied normalizing G for its maximal value (G/G_{max}) and plotting the mean values against step command potential (see inset Figure 2B). Data were fitted with *equation 3.3* (Boltzmann distribution).

The average fitting parameters values of activation curves – V_h and V_s - are presented in table 3.5. V_h values were as follows: -2.1 ± 0.82mV and -2.9 ± 0.60mV, for fed and fasted neurones, respectively. V_s values were also similar in both conditions: 5.9 ± 0.17 mV/e-fold and 6.3 ± 0.17 mV/e-fold, for fed and fasted neurones, respectively. The differences registered are not significant ($P > 0.05$). These results support that feeding cycle does not exert any influence on the voltage-dependence of activation of whole-cell Ca^{2+} currents. Indeed, no shift and/or apparent deviation in the slope of the activation curves were observed (inset of Figure 3.25B).

On the other hand, $I_{sustained}$, also with an activation threshold around -30mV in both conditions, depicted higher mean current density values in neurones from fed animals. The maximum values, registered at 0mV, were -18.7 ± 2.92 pA/pF and -11.5 ± 1.50 pA/pF, for fed and fasted neurones, respectively. Differences are significant in the voltage range from -10mV to 10mV ($0.05 > P > 0.01$). The relative contribution of sustained current is illustrated by plotting the average of $I_{sustained}$ as a percentage of I_{peak}, obtained in the voltage range between -20mV and 20mV (figure 3.25C). Fed neurones showed significantly larger values in the voltage range between -10mV and 20mV ($0.05 > P > 0.01$). At 0mV, the values were as follows: 17.5 ± 2.81% and 11.1 ± 1.57%, for fed and fasted neurones, respectively. This is consistent with the higher abundance of current 'A' upon feeding.

Voltage dependence of steady-state of inactivation (h_∞)

The steady-state inactivation of the whole-cell current was measured using 1.5s conditioning pulses to voltages between -120 and 0 mV with 10 mV increments, from a holding potential of -70mV. The patch was then subjected to a 1s depolarising step to 0 mV to record the remaining current (Figure 3.26A).

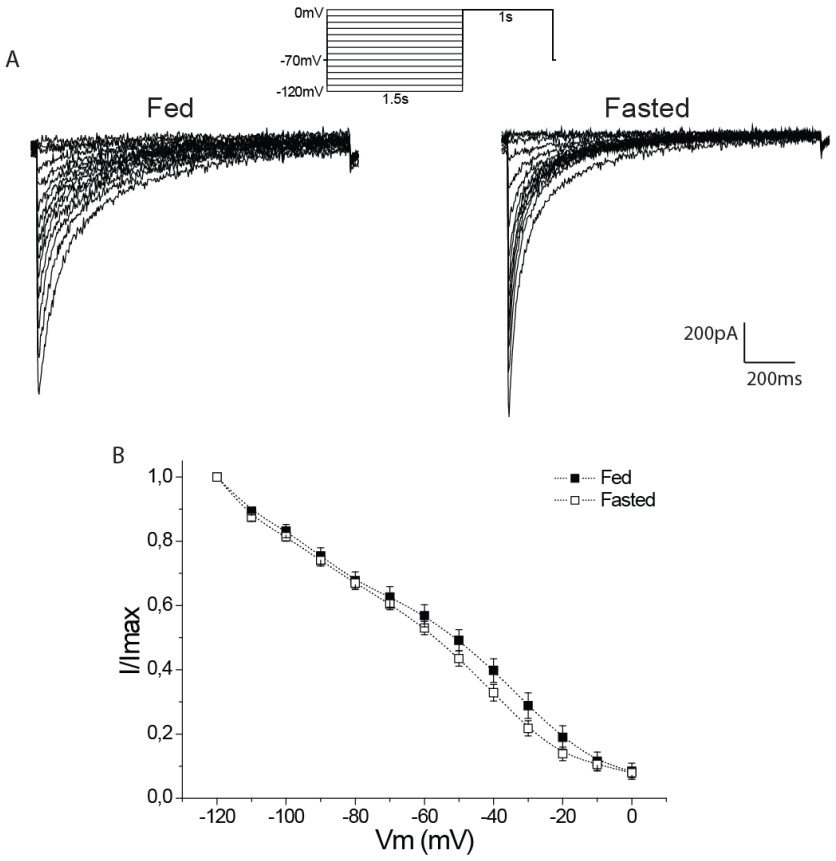

Figure 3.26- ***Influence of feeding cycle on steady-state inactivation (h_∞) of Ca^{2+} currents.*** *Whole-cell voltage clamp Ca^{2+} currents were evoked by a command step to 0 mV (1s) following a set of pre-pulses (1.5s) ranging from −120 mV to 0 mV in steps of 10 mV; holding potential of −70 mV (inset). A) Records were obtained in the command pulse from a neuron of a fed and fasted animal. B) Mean peak Ca^{2+} current normalized to the maximum value (I/I_{max}) as a function of pre-pulse potentials, from neurones of fed (filled squares; n=13) and fasted (open squares; n=16) animals. The steady-state inactivation curves (h_∞) were best fitted by a sum of sigmoids (equation 2) and the significant shift of the second component is expressed in the V_{h2} values: -36.9 ± 2.02mV and –42.99 ± 2.55mV, for fed and fasted neurones, respectively (t-student analysis; 0,01<P<0,05). Error bars are ±S.E.M. values.*

Peak current values were normalized to the maximal response (I/I_{max}) and plotted against conditioning pulses to obtain steady-state inactivation curves (Figure 3.26B). The results showed a complex biphasic curve, well described by a sum of two sigmoids:

$$I/I_{max} = \left[a/\left\{1 + e^{[(V_{h1} - V_m/V_{s1})]}\right\}\right] + \left[(1-a)/\left\{1 + e^{[(V_{h2} - V_m)/V_{s2}]}\right\}\right] \quad (\textit{Equation 3.6}),$$

where a and $(1-a)$ are the weighing coefficients of the first and second components of the steady-state of inactivation curves, V_m is the step command potential, $V_{h1}$and V_{h2} are the voltage at which half-maximal inactivation is reached within each component, and V_{s1} and V_{s2} the corresponding slope factors. The average fitting parameters are summarized in table 3.5.

Table 3.5- Activation and steady-state inactivation (h_∞) fitting parameters V_h (mV) and V_s (mV/e-fold) (Equations 3.3 and 3.6, respectively) for neurones of fed and fasted animals. Statistical analysis performed with a t-test; 0.01<P-value<0.05. Values are mean ± S.E.M.

	Voltage dependence of activation (mV)			**Voltage dependence of inactivation (mV)**				
	V_h	V_s	*n*	V_{h1}	V_{s1}	a	V_{h2}	V_{s2}
Fed	-2.1 ± 0.82	5.9 ± 0.17	20	-99.4 ± 1.37	-8.3 ± 0.48	0.33 ± 0.035	-36.9 ± 2.02	-16.1 ± 1.43
Fasted	-2.9 ± 0.60	6.3 ± 0.17	24	-100.5 ± 2.12	-7.5 ± 0.91	0.39 ± 0.053	-43.0 ± 2.55	-16.9 ± 1.55
P-value	*n.s.*		-		*n.s.*		0.033	*n.s.*

The parameters of the first, most hyperpolarized, component – V_{h1} and V_{s1} – was not altered with feeding cycle: V_{h1} = -99.4 ± 1.37mV, V_{s1} = -8.3 ± 0.48 mV/*e*-fold in fed neurones (n=13, $P > 0.05$) and V_{h1} = -100.5 ± 2.12 and V_{s1} = -7.5 ± 0.91 mV/*e*-fold in fasted neurones (n=16, $P > 0.05$). The first component (V_1) accounted for 33% and 39% of the total current, in fed and fasted neurones, respectively. Such difference is not significant ($P > 0.05$). However, we observed that V_{h2} parameter statistically differed in fed and fasted neurones: -36.9 ± 2.02mV and -43.0 ± 2.55mV, respectively ($0.05 > P > 0.01$). This result indicates that the Ca^{2+} currents accountable for the second component of h_∞ underwent a significant depolarizing shift by 6mV in fed neurones. This demonstrates that Ca^{2+} currents in fasted neurones begin to inactivate at more negative potentials, thus pointing to a reduction in the levels of excitability in fasting conditions.

Time-constant of inactivation (τ_h(ms))

The decay phase of the Ca^{2+} currents, obtained with activation protocols (Figure 3.24), was described with an exponential time course, given by *Equation 3.4.*

In the present study, we could only detect the presence of two components of inactivation at more depolarized voltage potentials (less negative than -20mV, including). Figure 3.27A illustrates exponential fits to the decay phase of currents evoked in command steps

to -30, and -20 mV from -70 mV holding potential. At -30 mV, the current decayed monoexponentially with a time constant of 153 ms; at -20 mV, the inactivating phase was best described by two exponentials, with time constants of 42ms and 266ms.

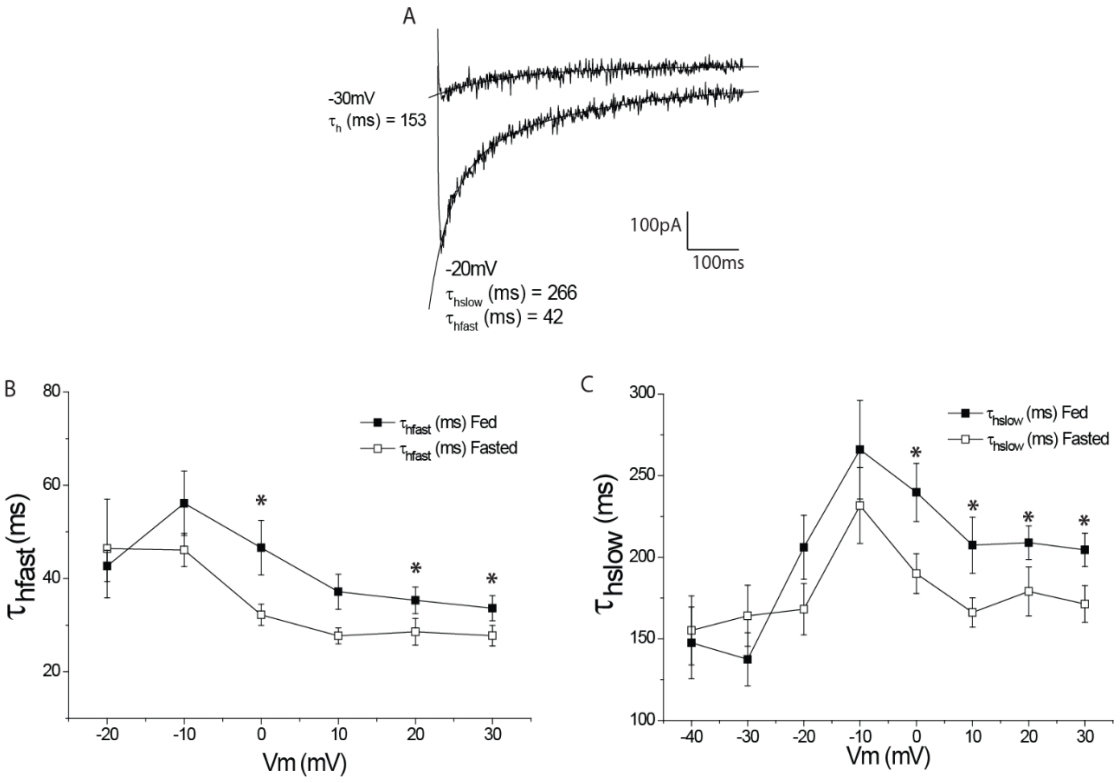

*Figure 3.27- **Effect of feeding cycle on the time-constant of inactivation (τ_h(ms)) of Ca^{2+} currents.** A) Illustration of fitting of the decay phase of Ca^{2+} currents evoked by an activation protocol. The inactivation could be described by a single (-30mV command pulse) or a by double exponential (-20mV command pulse), equation 3.4. B) and C) Voltage-dependence of the B) fast and C) slow components of time-constant of inactivation (τ_{hfast} (ms) and τ_{hslow} (ms), respectively) measured in activation protocols, of fed (filled squares) and fasted (open squares) animals. Error bars are ±S.E.M. (* t-test; 0.05 > P > 0.01).*

The effect of feeding cycle over the voltage dependence of τ_h(ms) was addressed. The mean values of τ_{hf} and τ_{hs}, measured in activation protocols, are depicted in figures 3.27B and 3.27C, respectively.

The plot concerning the fast component (Figure 3.27B) demonstrates that τ_{hf} was voltage dependent in both fed and fasted neurones. Fed neurones showed slower values of τ_{hf} nearly in all voltage range studied. At 0mV, we have obtained 46.6 ± 5.86ms (fed neurones) and 32.3 ± 2.29ms (fasted neurones). The difference is significant at 0mV, 20mV and 30mV ($0.05 > P > 0.01$). τ_{hs} (Figure 3.27C) shows that fed and fasted neurones inactivated in a complex way, suggesting a combination of inactivation mechanisms (Ribeiro & Costa, 2000). For voltage command steps more depolarized (from 0mV to

30mV), fed neurones showed significant larger τ_{hs}values ($0.05 > P > 0.01$). In command steps to 0mV, the mean values were as follows: 239.7 ± 17.78ms and 189.9 ± 12.21ms, for fed and fasted neurones, respectively. Overall, fed neurones inactivated slower than fasted neurones, which suggests a long-lasting entry of Ca^{2+} ions into the soma of CA1 hippocampal neurones of fed animals.

To assess the contribution of each current type presently described in this report (Figure 3.24) to the overall time-constant of inactivation, the mean values of τ_{hf} and τ_{hs} of currents 'A', 'B' and 'C' were discriminated. The comparison of these values allowed to evaluate whether the results observed on the kinetics of inactivation from the pooled data were due to: a) the differential distribution of the currents between fed and fasted neurones (related to the intrinsic characteristics of each current type) or; b) differences obtained within the same current type between both conditions (a given type current, say A-type, could be faster in fasted neurones when compared to fed neurones), or both. The results were obtained at a command potential of 0mV and are showed in Table 3.6.

Table 3.6- Average values of time-constants (ms) of the fast and slow inactivating components - τ_{hfast} and τ_{hslow}, addressed for each type of current outlined in this study, at 0mV. Values are mean ± S.E.M.

	Types of current								
At 0mV	**A'**			**B'**			**C'**		
	τ_{hfast} (ms)	τ_{hslow} (ms)	*n*	τ_{hfast} (ms)	τ_{hslow} (ms)	*n*	τ_{hfast} (ms)	τ_{hslow} (ms)	*n*
Fed	65.5 ± 7.99	289.3 ± 26.48	10	29.8 ± 2.21	190.1 ± 9.31	10	-	-	-
Fasted	50.1 ± 4.82	282.7 ± 17.30	3	32.0 ± 2.18	192.2 ± 14.85	14	24.7 ± 1.37	148.4 ± 5.26	7
P-value			*n.s.*					-	

In what concerns the current 'A', fed neurones disclosed augmented τ_{hf}values, however the difference is not significant ($P > 0.05$), given the reduced number of patches with this type of current found in fasted neurones (n=3). τ_{hs} does not differ between conditions. Current 'B' showed similar values of $\tau_{hf}$and τ_{hs}, whether the animals were or not fed, thus not contributing to the observed variation in the overall time constant of inactivation between conditions. One can conclude that the faster inactivation observed in the pooled data from fasted neurones is supported by the exclusive expression of 'C' current.

The differences observed in Ca^{2+} currents decay in both conditions can also be quantified by the analysis of the coefficients of fast and slow inactivating components - a_{fast} and a_{slow}. Figure 3.28A depicts the voltage-dependence of the ratios calculated from the coefficients in *Equation 3.4* (a_f/a_s).

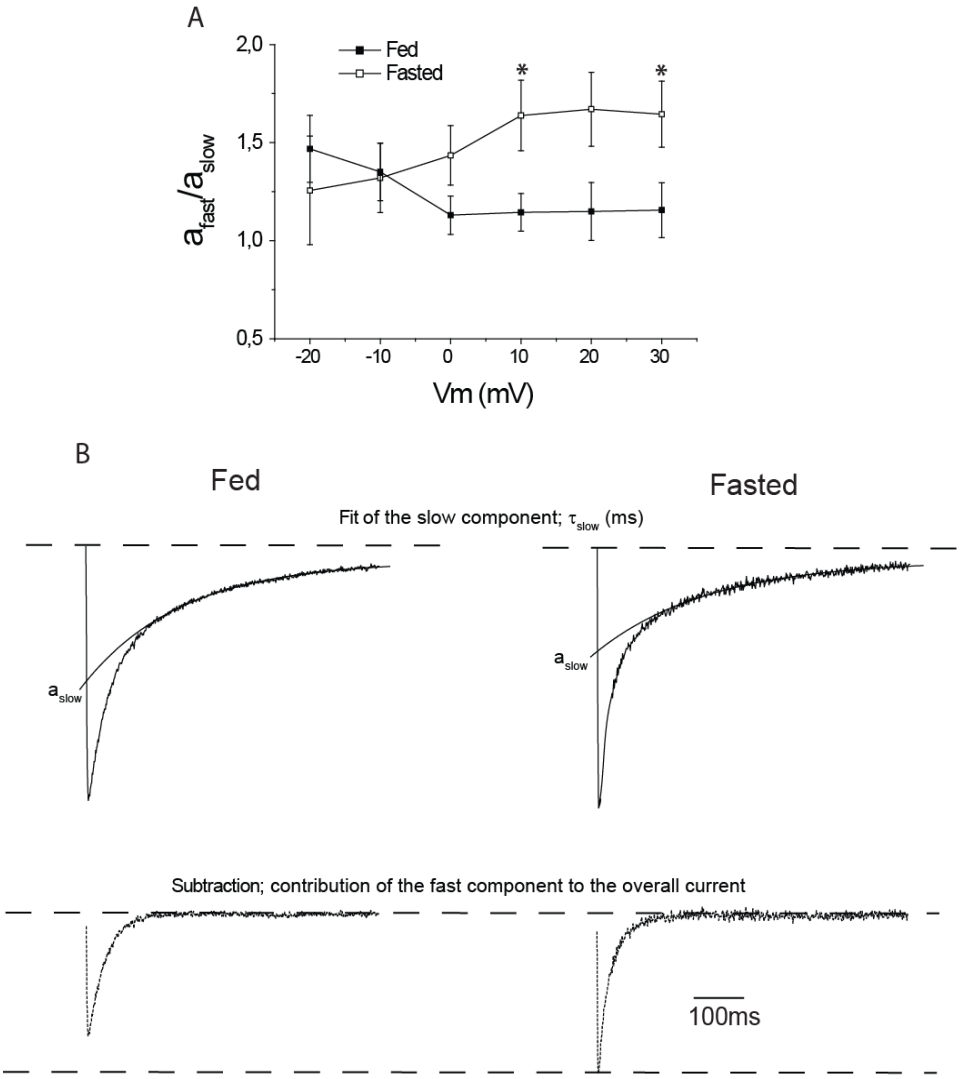

*Figure 3.28- **Effect of feeding cycle on the coefficients of the inactivating components, a_{fast} and a_{slow}.** A) Analysis of the voltage-dependence of the ratio af/as in fed (filled squares) and fasted (open squares) neurones. Error bars are ±S.E.M. (* t-test; 0.05 > P > 0.01). B) Illustration of the influence of feeding cycle on the inactivating components of Ca^{2+} currents. Typical examples of B-type current traces recorded in fed and fasted neurones, obtained at 0mV. Currents were normalized to peak current values for a better comprehension of the data. In the upper traces, the fitting was taken within the slow component of the inactivation of Ca^{2+} current. The fast component (bottom traces) is obtained by subtracting the τ_{slow} traces to the overall current. In fasted neurones, a faster decay and a greater amplitude of the fast component is observed.*

In the voltage range used, the fast component prevails over the slow component (ratio greater than 1). In fasted neurones, a_f/a_s increased with depolarization, as a straight

consequence of the major contribution of the fast component (Figure 3.28B). In fed neurones, we observed a decrease in the ratio values, reaching a plateau level close to unitary value between 0mV and 30mV, which can be explained by convergence of the values registered for the coefficients of fast and slow components in such voltage range (data not shown). At potentials more positive than 10 mV, the ratio a_f/a_s clearly differed in fed and fasted neurones. At 10mV, the mean ratio values were: 1.1 ± 0.10 (fed neurones) and 1.6 ± 0.18 (fasted neurones). The difference is statistically significant at 10mV and 30mV ($0.05 > P > 0.01$).

Figure 3.28B sets a graphical explanation of the effect of feeding cycle over the time-constants and respective coefficients of inactivation. The traces revealed a sharper decay and a greater amplitude of the fast component in the illustrated fasted neuron, as oppose to a greater amplitude of the slow component in the fed neuron. This is consistent with an overall faster inactivation obtained for neurones of fasting animals.

3.3.5.2 Discussion

The present report addresses the influence of feeding cycle on the whole-cell Ca^{2+} currents of rat hippocampal CA1 neurones. Three types of high threshold voltage activated (HVA) currents with different current decay properties were recorded. Fed neurones expressed more prominently a slowly-inactivating (here defined as 'sustained') current at the end of the 600ms pulse, whereas currents with the fastest kinetics were mostly attributed to fasted neurones. This effect of feeding cycle upon the expression of Ca^{2+} currents resulted in increased mean values of time-constants of inactivation (τ_h) upon feeding. Additionally, a depolarizing shift in the second component of the steady-state inactivation (h_∞) curve was observed in fed neurones.

The distinct whole-cell currents were termed, for simplicity, 'A', 'B' and 'C'. Current 'B' was found in both conditions, with a similar patch distribution in fed and fasted neurones: 50% and 58%, respectively. The main differences reported here were related to the differential distribution of the remaining currents. Current 'A', characterized by the presence of a conspicuous sustained current, was observed more often in neurones from fed animals. This explains the significantly higher amplitude of the sustained current in fed neurones (see figure 3.25B). In turn, current 'C', with the fastest current decay kinetics, was only observed in fasted neurones.

The heterogeneity of Ca^{2+} currents observed here must be indicative of distinct molecular identities at the surface of neuronal plasma membrane. Accordingly, the respective *I-V* curves invariably disclosed an activation threshold at -30mV, which means that the variation on the channel´s phenotype fits within the range of HVA channels (Tsien *et al.*, 1988; Bean, 1989; Snutch & Reiner, 1992; Catterall, 2000, 2011; Brini *et al.*, 2014). The absence of a low-threshold activated (LVA) current indicates we could not detect T-type Ca^{2+} currents, which is in accordance with several reports on the effect of maturation over the expression of Ca^{2+} currents (Fisher *et al.*, 1990; Thompson & Wong, 1991; Campbell *et al.*, 1996; Thibault & Landfield, 1996; Kortekaas & Wadman, 1997; Porter *et al.*, 1997; Ribeiro & Costa, 2000). At the age of the animals used in this study (P21-P29), hippocampal neurones consistently express Ca^{2+} currents with electrophysiological properties similar to those in older animals (Lukyanetz *et al.*, 2002), *i.e.*, mostly HVA and seldom LVA currents. It is established that rat hippocampal CA1 neurones express all known types of HVA Ca^{2+} channels (L, N, P, Q and R; Ishibashi *et al.*, 1998; Lenz *et*

al., 1998), being the N- and L- type Ca^{2+} channels the most predominant categories, mainly contributing to total HVA calcium current in CA1 hippocampal neurones (Fisher *et al.*, 1990; Westenbroek *et al.*, 1990; Vreugdenhil & Wadman, 1992; Magee & Johnston, 1995; Pravettoni *et al.*, 2000; Bowden *et al.*, 2001; Lukyanetz *et al.*, 2002; Leitch *et al.*, 2009). In the present report, we did not pursuit a pharmacological approach, nor presented additional single-channel data to distinguish between HVA Ca^{2+} currents. However, we provide indications that infer about the phenotype of the Ca^{2+} channel currents present in the plasma membrane of fed and fasted neurones, as being either N- or L-type Ca^{2+} currents. The slowly-inactivating sustained currents, characteristic of the 'A'-type currents outlined in this study, are typically described as being L-type current (Nowycky *et al.*, 1985; Takahashi *et al.*, 1989; Catterall, 2000; Lipscombe, 2002; Helton, 2005), whereas the faster inactivating currents - 'B' and 'C' types - are likely to be linked to the expression of mainly N-type channels (Nowycky *et al.*, 1985; Tsien *et al.*, 1988; Plummer *et al.*, 1989; Plummer & Peter, 1991; McNaughton & Randall, 1997).

In what the voltage dependence of inactivation is concerned, the experimental data points of h_∞ further supports a heterogeneous and differential distribution of Ca^{2+} channels in rat hippocampal CA1 neurones during feeding cycle. Both h_∞ curves were well fitted by double Boltzmann functions, suggesting either that at least two distinct types of Ca^{2+} channels are recruited in the inactivation or that a single population of channels undergoes multiple inactivation processes (Ribeiro & Costa, 2000; Lukyanetz *et al.*, 2002). As we recorded Ca^{2+} currents from the whole surface of the neurones, the results here depicted must comply with the first hypothesis. Moreover, in fed neurones, V_{h2} is significantly shifted towards depolarized potentials, which is indicative of an increased involvement of Ca^{2+} channels that inactivate with stronger depolarizations, another electrophysiological feature of the L-type channels (Ozawa *et al.*, 1989; Yasuda *et al.*, 2004; Catterall *et al.*, 2005; Spafford *et al.*, 2006). This result suggests a greater steady-state availability of this type of channels in fed neurones, which is aligned with the major fraction of patches recorded with current 'A' in neurones from fed animals (50%, 10 out of 20 patches), in comparison to neurones of fasted animals (12.5%, 3 out of 24 patches).

The distinct profiles of the whole-cell currents can be quantified by the analysis of the coefficients of fast and slow components of the time-constant of inactivation – a_{fast} and a_{slow}. The ratio a_{fast}/a_{slow} showed significant higher values in fasted neurones, mostly due to a larger contribution of a_{fast}, when compared to fed neurones. Our results also depicted

an increased prevalence of a_{slow} in fed neurones in relation to fasted neurones, which is closely related to the presence of the Ca^{2+} sustained current. The illustration of the proportions between a_{fast} and a_{slow} in figure 3.28B helps to explain the slower mean values of τ_{hf} and τ_{hs} observed in fed neurones (see figures 3.27B and 3.27C).

Given the gathered evidence, one can point out that the major contribution of the slowly-inactivating, resembling L-type currents, will enable the entry of Ca^{2+} for a longer period into the soma of fed neurones. On the other hand, the expression of a 'C-type' current has the major contribution to the overall fastest kinetics of inactivation observed in fasted neurones (see table 3.6 and figure 3.27).

In conclusion, the array of expression of Ca^{2+} currents in fed and fasted neurones might be related to a variation in the Ca^{2+} channels´ phenotype, in the course of feeding cycle. The predominant 'A'-type current in fed neurones, in relation to fasted neurones, anticipates larger entry of Ca^{2+} ions into the soma during membrane depolarizations, which may determine significantly different physiological outputs during the feeding cycle. Indeed, the greater intracellular Ca^{2+} dynamics envisaged in fed neurones may reinforce the neuronal synaptic performance, given the vital role of Ca^{2+} on the signal transduction processes directly involved on synaptic-dependent memory phenomena, like Long-Term Potentiation (LTP) (Eccles, 1983; Voronin, 1983; Volianskis & Jensen, 2003; Zamponi *et al.*, 2015).

Thus, the indication of a larger Ca^{2+} influx through voltage-gated channels, brought up by 1) an abundance of a Ca^{2+}-sustained current and 2) the depolarizing shift of V_{h2} observed in the h_∞ curves, might concur to higher rate of synaptic plasticity events in fed neurones. Such outcome would endorse the role of hippocampus in inhibiting meal onset during the post-prandial period, due to the formation of episodic-meal related memories, as established by other authors (Higgs, 2002, 2008; Parent, 2016). The dynamics of voltage gated Ca^{2+} channels observed during the feeding cycle must be related with molecular mechanisms by which hippocampus integrates information to ensure energy homeostasis.

3.4 References

Afonso RA, Fernandes AB, Santos C, Ligeiro D, Ribeiro RT, Lima IS, Patarrao RS, Videira PA, Caldeira J & Macedo MP (2012). Postprandial Insulin Resistance in Zucker Diabetic Fatty Rats is Associated with Parasympathetic-Nitric Oxide Axis Deficiencies. *J Neuroendocrinol* **24,** 1346–1355.

Almers W (1978). Gating currents and charge movements in excitable membranes. *Rev Physiol Biochem Pharmacol* **82,** 96–190.

Andersen P, Morris R, Amaral D, Bliss T & O`Keefe J (2007). *The Hippocampus Book*. Oxford University Press, Mew York.

Armstrong CM & Bezanilla F (1973). Currents related to movement of the gating particles of the sodium channels. *Nature* **242,** 459–461.

Armstrong CM & Bezanilla F (1977*a*). Inactivation of the sodium channel. II. Gating current experiments. *J Gen Physiol* **70,** 567–590.

Armstrong CM & Bezanilla F (1977*b*). Inactivation of the sodium channel. II. Gating current experiments. *J Gen Physiol* **70,** 567–590.

Bean BP (1989). Classes of Calcium Channels in Vertebrate Cells. *Annu Rev Physiol* **51,** 367–384.

Bezanilla F (1977). Inactivation o f the S o d i u m C h a n n e l I . Sodium Current Experiments. **70,** 549–566.

Bezanilla F (2000). The voltage sensor in voltage-dependent ion channels. *Physiol Rev* **80,** 555–592.

Bezanilla F & Armstrong CM (1977). Inactivation of the sodium channel. I. Sodium current experiments. *J Gen Physiol* **70,** 549–566.

Bliss T V & Collingridge GL (1993). A synaptic model of memory: long-term potentiation in the hippocampus. *Nature* **361,** 31–39.

Bowden SEH, Fletcher S, Loane DJ & Marrion N V (2001). Somatic Colocalization of Rat SK1 and D class (Cav1.2) L-type Calcium Channels in Rat CA1 Hippocampal Pyramidal Neurones. *J Neurosci* **21,** 1–6.

Brini M, Calì T, Ottolini D & Carafoli E (2014). Neuronal calcium signaling: Function and dysfunction. *Cell Mol Life Sci* **71,** 2787–2814.

Bruehl C & Witte OW (2003). Relation Between Bicarbonate Concentration and Voltage Dependence of Sodium Currents in Freshly Isolated CA1 Neurones of the Rat. *J Neurophysiol*.

Campbell LW, Hao S-YY, Thibault O, Blalock EM & Landfield PW (1996). Aging changes in voltage-gated calcium currents in hippocampal CA1 neurones. *J Neurosci* **16,** 6286–6295.

Carbone E & Lux HD (1987). Kinetics and selectivity of a low-voltage-activated calcium current in chick and rat sensory neurones. *J Physiol* **386,** 547–570.

Catterall WA (1992). Cellular and molecular biology of voltage-gated sodium channels. *Physiol Rev* **72,** S15-48.

Catterall WA (2000*a*). From ionic currents to molecular mechanisms: the structure and function of voltage-gated sodium channels. *Neuron* **26,** 13–25.

Catterall WA (2011). Voltage-Gated Calcium Channels. *Cold Spring Harb Perspect Biol*; DOI: 10.1016/B978-0-323-44733-1.00002-X.

Catterall W a (2000*b*). Structure and Regulation of Voltage-Gated Ca2+ Channels. *Annu Rev Cell Dev Biol* **16,** 555.

Catterall W a, Goldin AL & Waxman SG (2005*a*). International Union of Pharmacology. XLVII. Nomenclature and structure-function relationships of voltage-gated sodium channels. *Pharmacol Rev* **57,** 397–409.

Catterall W a, Perez-Reyes E, Snutch TP & Striessnig J (2005*b*). International Union of Pharmacology. XLVIII. Nomenclature and structure-function relationships of voltage-gated calcium channels. *Pharmacol Rev* **57,** 411–425.

Catterall WA, Morrow CS & Hartshorne RP (1979). Neurotoxin binding to receptor sites associated with voltage-sensitive sodium channels in intact, lysed, and detergent-solubilized brain membranes. *J Biol Chem* **254,** 11379–11387.

Chad JE, Stanford I, Wheal HV, Williamson R & Woodhall G (1991). Dissociated neurones from adult rat hippocampus. In *Cellular neurobiology: a practical approach*, ed. Chad J & Wheal H, pp. 19–37. Oxford University Press, Oxford.

Chong HL & Ruben PC (2008). Interaction between voltage-gated sodium channels and the neurotoxin, tetrodotoxin. *Channels* **2,** 407–412.

Clapham DE (2007). Calcium Signaling. *Cell* **131,** 1047–1058.

Costa PF (1996). The kinetic parameters of sodium currents in maturing acutely isolated rat hippocampal CA1 neurones. *Brain Res Dev Brain Res* **91,** 29–40.

Costa PF, Santos AI & Ribeiro MA (1994). Potassium currents in acutely isolated maturing rat hippocampal CA1 neurones. *Dev Brain Res* **83,** 216–223.

Curtis BM & Catterall WA (1984). Purification of the Calcium Antagonist Receptor of the Voltage-Sensitive Calcium Channel from Skeletal Muscle Transverse Tubules.

Biochemistry **23,** 2113–2118.

Dart C (2010). Lipid microdomains and the regulation of ion channel function. *J Physiol* **588,** 3169–3178.

Davidson T, Kanoski S, Walls E & Jarrard L (2005). Memory inhibition and energy regulation. *Physiol Behav* **86,** 731–746.

Davidson TL, Chan K, Jarrard LE, Kanoski SE, Clegg DJ & Benoit SC (2009). Contributions of the Hippocampus and Medial Prefrontal Cortex to Energy and Body Weight Regulation. *Hippocampus* **19,** 235–252.

Dolphin AC (2009). Calcium channel diversity: multiple roles of calcium channel subunits. *Curr Opin Neurobiol* **19,** 237–244.

Eccles JC (1983). Calcium in long-term potentiation as a model for memory. *Neuroscience* **10,** 1071–1081.

Eijkelkamp N, Linley JE, Baker MD, Minett MS, Cregg R, Werdehausen R, Rugiero F & Wood JN (2012). Neurological perspectives on voltage-gated sodium channels. *Brain* **135,** 2585–2612.

Ertel EA, Campbell KP, Harpold MM, Hofmann F, Mori Y, Perez-Reyes E, Schwartz A, Snutch TP, Tanabe T, Birnbaumer L, Tsien RW & Catterall WA (2000). Nomenclature of Voltage-Gated Calcium Channels. *Neuron* **25,** 533–535.

Fatt P & Katz B (1953). The electrical properties of crustacean muscle fibres. *J Physiol* **120,** 171–204.

Fernandes J (2002). *Single channel sodium currents in rat CA1 neurones at two stages of maturation: two kinetically distinct channels* (thesis). Nova Medical School.

Fernandes J, Marvão P, Santos a I & Costa PF (2001). Sodium channel currents in maturing acutely isolated rat hippocampal CA1 neurones. *Brain Res Dev Brain Res* **132,** 159–174.

Fisher RE, Gray R & Johnston D (1990). Properties and distribution of single voltage-gated calcium channels in adult hippocampal neurones. *JNeurophysiol* **64,** 91–104.

Fox AP, Nowycky MC & Tsien RW (1987*a*). Single-channel recordings of three types of calcium channels in chick sensory neurones. *J Physiol* **394,** 173–200.

Fox AP, Nowycky MC & Tsien RW (1987*b*). Kinetic and pharmacological properties distinguishing three types of calcium currents in chick sensory neurones. *J Physiol* **394,** 149–172.

French CR, Sah P, Bucketr KJ, Gage PW & Curtin J (1990). A Voltage-dependent Persistent Sodium Current in Mammalian Hippocampal Neurones. *J Gen Physiol*

0, 1139–1157.

Gleichmann M & Mattson MP (2011). Neuronal Calcium Homeostasis and Dysregulation. *Antioxid Redox Signal* **14,** 1261–1273.

Goldin AL (1999). Diversity of mammalian voltage-gated sodium channels. *Ann N Y Acad Sci* **868,** 38–50.

Goldin AL (2003*a*). Mechanisms of sodium channel inactivation. *Curr Opin Neurobiol* **13,** 284–290.

Goldin AL (2003*b*). Mechanisms of sodium channel inactivation. *Curr Opin Neurobiol* **13,** 284–290.

Gong B, Rhodes KJ, Bekele-Arcuri Z & Trimmer JS (1999). Type I and type II Na(+) channel alpha-subunit polypeptides exhibit distinct spatial and temporal patterning, and association with auxiliary subunits in rat brain. *J Comp Neurol* **412,** 342–352.

Gordon D, Merrick D, Auld V, Dunn R, Goldin AL, Davidson N & Catterall WA (1987). Tissue-specific expression of the RI and RII sodium channel subtypes. *Proc Natl Acad Sci U S A* **84,** 8682–8686.

Grubb MS, Shu Y, Kuba H, Rasband MN, Wimmer VC & Bender KJ (2011). Short- and Long-Term Plasticity at the Axon Initial Segment. *J Neurosci* **31,** 16049–16055.

Hagiwara S, Ozawa S & Sand O (1975). Voltage clamp analysis of two inward current mechanisms in the egg cell membrane of a starfish. *J Gen Physiol* **65,** 617–644.

Hamill OP, Marty A, Neher E, Sakmann B & Sigworth FJ (1981). Improved patch-clamp techniques for high-resolution current recording from cells and cell-free membrane patches. *Pflugers Arch Eur J Physiol* **391,** 85–100.

Hannapel RC, Henderson YH, Nalloor R, Vazdarjanova A & Parent MB (2017). Ventral hippocampal neurones inhibit postprandial energy intake. *Hippocampus* **27,** 274–284.

Hebben N, Corkin S, Eichenbaum H & Shedlack K (1985). Diminished ability to interpret and report internal states after bilateral medial temporal resection: case H.M. *Behav Neurosci* **99,** 1031–1039.

Helton TD (2005). Neuronal L-Type Calcium Channels Open Quickly and Are Inhibited Slowly. *J Neurosci* **25,** 10247–10251.

Henderson YO, Nalloor R, Vazdarjanova A & Parent MB (2016). Sweet orosensation induces Arc expression in dorsal hippocampal CA1 neurones in an Experience-dependent manner. *Hippocampus* **26,** 405–413.

Henderson YO, Smith GP & Parent MB (2013). Hippocampal neurones inhibit meal onset. *Hippocampus* **23,** 100–107.

Hering S, Sokolov S, Berjukow S, Marksteiner R, Margreiter E & Timin EN (2005). Calcium Channel Block and Inactivation. *Voltage-Gated Calcium Channels*281–293.

Higgs S (2002). Memory for recent eating and its influence on subsequent food intake. *Appetite* **39,** 159–166.

Higgs S (2008). Cognitive influences on food intake: The effects of manipulating memory for recent eating. *Physiol Behav* **94,** 734–739.

Hille B (2001). *Ion Channels of Excitable Membranes*, Third. Sinauer Associates, Inc.

Hirschberg B, Rovner A, Lieberman M & Patlak J (1995). Transfer of twelve charges is needed to open skeletal muscle Na+ channels. *J Gen Physiol* **106,** 1053–1068.

Hodgkin AL & Huxley AF (1952*a*). Currents carried by sodium and potassium ions through the membrane of the giant axon of Loligo. *J Physiol* **116,** 449–472.

Hodgkin AL & Huxley AF (1952*b*). The dual effect of membrane potential on sodium cinductance in the giant axon of Loligo. *J Physiol* **116,** 497–506.

Hodgkin AL & Huxley AF (1952*c*). A quantitative description of membrane current and its application to conduction and excitation in nerve. *J Physiol* **117,** 500–544.

Hodgkin AL, Huxley AF & Katz B (1952). Measurement of current-voltage relations in the membrane of the giant axon of *Loligo*. *J Physiol* **116,** 424–448.

Hodgkin AL & Huxley A.F. (1952). The Components of Membrane Counductance in the Giant Axon of Loligo. *J Physiol* **116,** 473–496.

Hofmann F, Biel M & Flockerzi V (1994). Molecular basis for Ca2+ channel diversity. *Annu Rev Neurosci* **17,** 399–418.

Hsu TM, Hahn JD, Konanur VR, Noble EE, Suarez AN, Thai J, Nakamoto EM & Kanoski SE (2015). Hippocampus ghrelin signaling mediates appetite through lateral hypothalamic orexin pathways. *Elife* **4,** 1–20.

Hu W, Tian C, Li T, Yang M, Hou H & Shu Y (2009). Distinct contributions of Nav1.6 and Nav1.2 in action potential initiation and backpropagation. *Nat Neurosci* **12,** 996–1002.

Huang H, Priori SG, Napolitano C, O'Leary ME & Chahine M (2011). Y1767C, a novel SCN5A mutation, induces a persistent Na+ current and potentiates ranolazine inhibition of Nav1.5 channels. *AJP Hear Circ Physiol* **300,** H288–H299.

Igelmund P, Zhao YQ & Heinemann U (1996). Effects of T-type, L-type, N-type, P-

type, and Q-type calcium channel blockers on stimulus-induced pre- and postsynaptic calcium fluxes in rat hippocampal slices. *Exp brain Res* **109,** 22–32.

Ishibashi H, Murai Y & Akaike N (1998). Effect of nilvadipine on the voltage-dependent Ca2+ channels in rat hippocampal CA1 pyramidal neurones. *Brain Res*121–127.

Isom LL (2001). Sodium Channel β Subunits: Anything but Auxiliary. *Neurosci* **7,** 42–54.

Jacka FN, Cherbuin N, Anstey KJ, Sachdev P & Butterworth P (2015). Western diet is associated with a smaller hippocampus: a longitudinal investigation. *BMC Med* **13,** 215.

Jiang Q-X & Gonen T (2012). The influence of lipids on voltage-gated ion channels. *Curr Opin Struct Biol* **22,** 529–536.

Kasimova MA, Tarek M, Shaytan AK, Shaitan K V. & Delemotte L (2014). Voltage-gated ion channel modulation by lipids: Insights from molecular dynamics simulations. *Biochim Biophys Acta - Biomembr* **1838,** 1322–1331.

Kay AR (1991). Inactivation Kinetics of Calcium Current of acutely dissociated CA1 pyramidal cells of the mature guinea-pig hippocampus. *J Physiol* **437,** 27–48.

Kay AR & Wong RKS (1986). Isolation of neurones suitable for patch-clamping from adult mammalian central nervous systems. *J Neurosci Methods* **16,** 227–238.

Kay AR & Wong RKS (1987). Calcium current activation kinetics in isolated pyramidal neurones of the CAl region of the mature guinea-pig hippocampus. *J Physiol* **392,** 603–616.

Ketelaars SO., Gorter J., van Vliet E., Lopes da Silva F. & Wadman W. (2001*a*). Sodium currents in isolated rat CA1 pyramidal and dentate granule neurones in the post-status epilepticus model of epilepsy. *Neuroscience* **105,** 109–120.

Ketelaars SOM, Gorter JA, Van Vliet EA, Lopes da Silva FH & Wadman WJ (2001*b*). Sodium currents in isolated rat CA1 pyramidal and dentate granule neurones in the post-status epilepticus model of epilepsy. *Neuroscience* **105,** 109–120.

Kontis KJ & Goldin AL (1997). Sodium channel inactivation is altered by substitution of voltage sensor positive charges. *J Gen Physiol* **110,** 403–413.

Kortekaas P & Wadman WJ (1997). Development of HVA and LVA calcium currents in pyramidal CA1 neurones in the hippocampus of the rat. *Dev Brain Res* **101,** 139–147.

Kühn FJ & Greeff NG (1999). Movement of voltage sensor S4 in domain 4 is tightly

coupled to sodium channel fast inactivation and gating charge immobilization. *J Gen Physiol* **114,** 167–183.

Lacinová L (n.d.). *Voltage-dependent calcium channels* (thesis).

Lehmann-Horn F & Jurkat-Rott K (2003). Nanotechnology for neuronal ion channels. *J Neurol Neurosurg Psychiatry* **74,** 1466–1475.

Leitch B, Szostek A, Lin R & Shevtsova O (2009). Subcellular distribution of L-type calcium channel subtypes in rat hippocampal neurones. *Neuroscience* **164,** 641–657.

Leterrier C, Brachet A, Fache MP & Dargent B (2010). Voltage-gated sodium channel organization in neurones: Protein interactions and trafficking pathways. *Neurosci Lett* **486,** 92–100.

Lipscombe D (2002). L-Type Calcium Channels. Highs and New Lows. *Circ Res* **90,** 933–935.

Lipscombe D & Andrade A (2015). Calcium Channel CaVα1 Splice Isoforms - Tissue Specificity and Drug Action. *Curr Mol Pharmacol* **8,** 22–31.

Llinas BYR & Yarom Y (1981). Electrophysiology of mammalian inferior olivary neurones in vitro. Different types of voltage-dependent ionic conductances. *J Physiol* **315,** 549–567.

Llinas R, Sugimori M, Lin JW & Cherksey B (1989). Blocking and isolation of a calcium channel from neurones in mammals and cephalopods utilizing a toxin fraction (FTX) from funnel-web spider poison. *Proc Natl Acad Sci* **86,** 1689–1693.

Lukyanetz EA, Shkryl VM & Kostyuk PG (2002). Selective blockade of N-type calcium channels by levetiracetam. *Epilepsia* **43,** 9–18.

Madison D V & Edson EB (2001). Preparation of hippocampal brain slices. *Curr Protoc Neurosci* **Chapter 6,** Unit 6.4.

Magee JC & Johnston D (1995*a*). Characterization of single voltage-gated Na+ and Ca2+ channels in apical dendrites of rat CA1 pyramidal neurones. *J Physiol* **487,** 67–90.

Magee JC & Johnston D (1995*b*). Synaptic Activation of Voltage-Gated Channels in the Dendrites of Hippocampal Pyramidal Neurones. *Science (80-)* **268,** 301–304.

Marban E, Yamagishi T & Tomaselli GF (1998). Structure and function of voltage-gated sodium channels. *J Physiol*647–657.

McNaughton NCL & Randall AD (1997). Electrophysiological properties of the human N-type Ca2+ channel: I. Channel gating in Ca2+ Ba2+ and Sr2+ containing

solutions. *Neuropharmacology* **36,** 895–915.

Mickus T, Jung HY & Spruston N (1999*a*). Properties of slow, cumulative sodium channel inactivation in rat hippocampal CA1 pyramidal neurones. *Biophys J* **76,** 846–860.

Mickus T, Jung HY & Spruston N (1999*b*). Slow sodium channel inactivation in CA1 pyramidal cells. *Ann N Y Acad Sci* **868,** 97–101.

Nguyen HM & Goldin AL (2010). Sodium channel carboxyl-terminal residue regulates fast inactivation. *J Biol Chem* **285,** 9077–9089.

Nowycky MC, Fox AP & Tsien RW (1985). Three types of neuronal calcium channel with different calcium agonist sensitivity. *Nature* **316,** 440–443.

O'Leary ME, Chen LQ, Kallen RG & Horn R (1995). A molecular link between activation and inactivation of sodium channels. *J Gen Physiol* **106,** 641–658.

O´Dell TJ & Alger BE (1991). Single calcium channels in rat and guinea-pig hippocampal neurones. *J Physiol* **436,** 739–767.

Ogden D ed. (1994). *Microelectrode techniques: the Plymouth Workshop handbook*, 2nd edn. The Company of Biologists.

Ozawa S, Tsuzuki K, Iino M, Ogura A & Kudo Y (1989). Three types of voltage-dependent calcium current in cultured rat hippocampal neurones. *Brain Res* **495,** 329–336.

Palou A, Remesar X, Arola L, Herrera E & Alemany M (1981). Metabolic effects of short term food deprivation in the rat. *Horm Metab Res* **13,** 326–330.

Parent MB (2016). Cognitive control of meal onset and meal size: Role of dorsal hippocampal-dependent episodic memory. *Physiol Behav* **162,** 112–119.

Parent MB, Darling JN & Henderson YO (2014). Remembering to eat: hippocampal regulation of meal onset. *Am J Physiol Regul Integr Comp Physiol* **306,** R701–R713.

Patlak J & Horn R (1982). Effect of N-bromoacetamide on single sodium channel currents in excised membrane patches. *J Gen Physiol* **79,** 333–351.

Perez-reyes E (2003). Molecular Physiology of Low-Voltage-Activated T-type Calcium Channels. *Physiol Rev* **83,** 117–161.

Plummer MR, Logothetis DE & Hess P (1989). Elementary Properties and Pharmacological Sensitivities of Calcium Channels in Mammalian Peripheral Neurones. *Neuron* **2,** 1453–1463.

Plummer MR & Peter H (1991). Reversible uncoupling of inactivation in N-type

calcium channels. *Nature* **351,** 657–659.

Porter NM, Thibault O, Thibault V, Chen KC & Landfield PW (1997). Calcium channel density and hippocampal cell death with age in long-term culture. *J Neurosci* **17,** 5629–5639.

Poveda JA, Giudici AM, Renart ML, Molina ML, Montoya E & Encinar JA (2014). Lipid modulation of ion channels through specific binding sites. *BBA - Biomembr* **1838,** 1560–1567.

Poveda JA, Marcela Giudici A, Lourdes Renart M, Morales A & González-Ros JM (2017). Towards understanding the molecular basis of ion channel modulation by lipids: Mechanistic models and current paradigms. *Biochim Biophys Acta - Biomembr* **1859,** 1507–1516.

Pravettoni E, Bacci A, Coco S, Forbicini P, Matteoli M & Verderio C (2000). Different localizations and functions of L-type and N-type calcium channels during development of hippocampal neurones. *Dev Biol* **227,** 581–594.

Qiao X, Werkman TR, Gorter JA, Wadman WJ & Vliet EA Van (2013). Expression of sodium channel alpha subunits 1.1, 1.2 and 1.6 in rat hippocampus after kainic acid-induced epilepsy. *Epilepsy Res* **106,** 1–12.

Ribeiro MA & Costa PF (2000). Kinetic parameters of calcium currents in maturing acutely isolated CA1 cells. *Dev Brain Res* **124,** 11–23.

Robert Guy H & Conti F (1990). Pursuing the structure and function of voltage-gated channels. *Trends Neurosci* **13,** 201–206.

Sah P, Gibb AJ & Gage PW (1988). The sodium current underlying action potentials in guinea pig hippocampal CAI neurones. *J Gen Physiol* **91,** 373–398.

Sakmann B & Neher E eds. (1995). *Single-channel recording*, Second. Plenum Press, New York.

Sakmann B & Stuart G (1995). Patch-pipette recordings from the soma, dendrites, and axon of neurones in brain. In *Single-channel recording*, ed. Sakmann B & Neher E, pp. 199–211. Plenum Press, New York.

Schwartzkroin PA (1981). To slice or not to slice. In *Electrophysiology of isolated mammalian CNS preparations*, ed. Kerkut GA & Wheal HV. Academic Press, London.

Simms BA & Zamponi GW (2014). Neuronal voltage-gated calcium channels: Structure, function, and dysfunction. *Neuron* **82,** 24–45.

Snutch TP & Reiner PB (1992). Ca2+ channels: diversity of form and function. *Curr*

Opin Neurobiol **2,** 247–253.

Spruston N (2008). Pyramidal neurones: Dendritic structure and synaptic integration. *Nat Rev Neurosci* **9,** 206–221.

Stanton PK (1996). LTD, LTP, and the sliding threshold for long-term synaptic plasticity. *Hippocampus* **6,** 35–42.

Stühmer W, Conti F, Suzuki H, Wang XD, Noda M, Yahagi N, Kubo H & Numa S (1989). Structural parts involved in activation and inactivation of the sodium channel. *Nature* **339,** 597–603.

Sun GY, Huang HM, Kelleher JA, Stubbs EB & Sun AY (1988). Marker enzymes, phospholipids and acyl group composition of a somal plasma membrane fraction isolated from rat cerebral cortex: a comparison with microsomes and synaptic plasma membranes. *Neurochem Int* **12,** 69–77.

Takahashi K, Wakamori M & Akaike N (1989). Hippocampal CA1 pyramidal cells of rats have four voltage-dependent calcium channels. *Neurosci Lett* **104,** 229–234.

Taylor CP (1993). Na+ Currents that fail to inactivate. *Trends Neurosci* **664,** 455–460.

Thibault O & Landfield PW (1996). Increase in Single L-Type Calcium Channels in Hippocampal Neurones During Aging. *Science (80-)* **272,** 1017–1020.

Thompson SM & Wong RKS (1991). Development of calcium current subtypes in isolated rat hippocampal pyramidal cells. *J Physiol* **439,** 671–689.

Toselli M & Taglietti V (1990). Pharmacological Characterization of Voltage-Dependent Calcium Currents in Rat Hippocampal Neurones. *NeurosciLett* **112,** 70–75.

Tsien RW & Barret CF (2013). A Brief History of Calcium Channel Discovery. *Madame Curie Biosci Database - NCBI Bookshelf*.

Tsien RW, Lipscombe D, Madison DV, Bley KR & Fox AP (1988). Multiple types of neuronal calcium channels and their selective modulation. *Trends Neurosci* **11,** 431–438.

Ulbricht W (2005). Sodium Channel Inactivation: Molecular Determinants and Modulation. *Physiol Rev* **85,** 1271–1301.

Vacher H, Mohapatra DP & Trimmer JS (2008). Localization and Targeting of Voltage-Dependent Ion Channels in Mammalian Central Neurones. *Physiol Rev* **88,** 1407–1447.

Vanoye CG, Lossin C, Rhodes TH & George AL (2006). Single-channel Properties of Human Na V 1.1 and Mechanism of Channel Dysfunction in SCN1A -associated

Epilepsy. *J Gen Physiol J Gen Physiol* **0,** 1–14.

Vedantham V & Cannon SC (1998). Slow inactivation does not affect movement of the fast inactivation gate in voltage-gated Na+ channels. *J Gen Physiol* **111,** 83–93.

Vilin YY & Ruben PC (2001). Slow Inactivation in Voltage-Gated Sodium Channels: Molecular Substrates and Contributions to Channelopathies. *Cell Biochem Biophys* **35,** 171–190.

Voronin LL (1983). Long-term potentiation in the hippocampus. *Neuroscience* **10,** 1051–1069.

Vreugdenhil M, Faas GC & Wadman WJ (1998). Sodium currents in isolated rat CA1 neurones after kindling epileptogenesis. *Neuroscience* **86,** 99–107.

Vreugdenhil M & Wadman WJ (1992). Enhancement of calcium currents in rat hippocampal CA1 neurones induced by kindling epileptogenesis. *Neuroscience* **49,** 373–381.

Wang J, Ou S-W & Wang Y-J (2017). Distribution and function of voltage-gated sodium channels in the nervous system. *Channels* **11,** 0–0.

Webb JR (2007). *Slow inactivation of sodium channels: structural clues and disease associations* (thesis). The University of Texas Southwestern Medical Center at Dallas.

Westenbroek RE, Ahlijanian MK & Catterall WA (1990). Clustering of L-type Ca2+ channels at the base of major dendrites in hippocampal pyramidal neurones. *Nature* **347,** 281–284.

Westenbroek RE, Hell JW, Warner C, Dubel SJ, Snutch TP & Catterall W a (1992). Biochemical properties and subcellular distribution of an N-type calcium channel alpha 1 subunit. *Neuron* **9,** 1099–1115.

Westenbroek RE, Merrick DK & Catterall WA (1989). Differential subcellular localization of the RI and RII Na+ channel subtypes in central neurones. *Neuron* **3,** 695–704.

Williams RJP (1970). Cation Distributions and The Energy Status of Cells. *Bioenergetics* **1,** 215–225.

Wong RKS & Stewart M (1992). Different firing patterns generated in dendrites and somata of CA1 pyramidal neurones in guinea-pig hippocampus. *J Physiol* **457,** 675–687.

Yang N, George AL & Horn R (1996). Molecular basis of charge movement in voltage-gated sodium channels. *Neuron* **16,** 113–122.

4 Feeding cycle on neuronal Plasma membrane

The previous chapter of this thesis unveiled groundbreaking insights towards the effect of feeding cycle upon the biophysics and molecular expression of proteins imbedded in the phospholipid bilayer of the neuronal plasma membrane (PM). Those findings demanded a research upon the possible influence of the feeding cycle on the bulk lipid of the PM of rat hippocampus. Specifically, the present chapter provides information regarding the lipid composition, lateral heterogeneity and physical properties of PM, such as order and fluidity.

4.1 Plasma Membrane domains – lipid composition and distinct phases

Biological membranes provide physical boundaries between different worlds, separating the cellular and extracellular environments and the diverse cellular compartments. Contrary to previous assumptions based on the fluid mosaic model (Singer and Nicolson, 1972), the plasma membrane (PM) is presently described as a mosaic of domains with different lipid and protein compositions, properties and functions. Lipids are characterized by a great structural diversity, both in terms of their polar head group, length and unsaturation degree of their hydrocarbon chains (Van Meer, 2005; Pike, 2009; Quinn & Wolf, 2010; Sonnino & Prinetti, 2010; Sezgin *et al.*, 2017). The combination of different head groups and variations in fatty acid tails results in more than a thousand different lipid species in any eukaryotic cell (Van Meer *et al.*, 2008). Such multiplicity of structures may induce the lateral segregation of lipids into domains with distinctive properties in terms of size, rigidity, and thickness (Quinn & Wolf, 2010; Ingólfsson et al., 2014; Marquês et al., 2015). In this regard, one property of lipids that has fascinated scientists is their phase behaviour. In model systems, lipids can adopt various fluid and solid phases, which are characterized by a different spatial arrangement and motional freedom of each lipid with respect to its neighbours (Van Meer *et al.*, 2008). Since some of these phases are adopted under physiological conditions of temperature, pH, ionic

strength, etc., by lipid species that coexist in cell membranes, it is expected that arrangements reminiscent of these different phases may be found in biological membranes *in vivo* (Elson *et al.*, 2010; de Almeida & Joly, 2014).

The fundaments for the structure and functions of biological membranes are thus determined, to a considerable extent, by the intrinsic properties and composition of membrane lipids. Indeed, altered lipid composition is linked to many pathological conditions, *e.g.*, cancers, HIV infections, diabetes, atherosclerosis, cardiovascular disease, and Alzheimer's disease (Van Meer, 2005; Adibhatla & Hatcher, 2008; Ingólfsson *et al.*, 2017). The brain appears to be especially susceptible to disease states that are enhanced or accelerated by certain lipid compositions (Mattson, 2005; Adibhatla & Hatcher, 2008; Sebastião *et al.*, 2013; Escribá & Nicolson, 2014)(Adibhatla & Hatcher, 2008; Sebastião *et al.*, 2013). For instance, specific phosphatidyl inositol phosphate (PIP) lipids are involved in regulation of aspects of neuronal cell function. In particular, PIPs can modulate ion flux through PM ion channels (Dart, 2010; Jiang & Gonen, 2012; Poveda *et al.*, 2014) by direct interaction with the ion channels or by modulating membrane charge (Ingólfsson *et al.*, 2017).

The structure of biological membranes is mainly defined by three classes of lipids, whose packing forms the lipid bilayer: glycerophospholipids, which for simplicity will be designated here by phospholipids (PLs), sphingolipids (SLs) and sterols. PLs, the major lipids in eukaryotic membranes, contain a diacylglycerol (DAG) moiety as hydrophobic component with saturated or unsaturated fatty acyl chains of variable length and a polar head group, usually consisting of an alcohol attached to the phosphate group (Van Meer, 2005; Simons & Sampaio, 2011; van Meer & de Kroon, 2011). The general structure of PLs and common head groups are shown in Figure 4.1, being phosphatidylcholine (PC) the most abundant in mammals, followed by phosphatidylethanolamine (PE), phosphatidylserine (PS), phosphatidylinositol (PI), and phosphatidic acid (PA) (Van Meer, 2005; Van Meer *et al.*, 2008). The level of saturation of their fatty acyl chains regulates the rigidity of the biological membranes; the kinked hydrocarbon chains of the largely unsaturated PLs yield fluid phases in the membranes (also known as l_d, liquid-disordered phase), thus preventing close packing of the lipids within the bilayer. Analysis of the phospholipid composition of the rat hippocampus shows PC, PE and PS as the predominant phospholipids (Chavko *et al.*, 1993; Wen & Kim, 2004), while the fatty acid composition shows enrichment with 16:0 (palmitic), 18:0 (stearic), 18:1 (oleic), 18:2

(linoleic), 20:4 (arachinodic) and 22:6 (docosahexaenoic) fatty acids (Ulmann *et al.*, 2001; Murthy *et al.*, 2002).

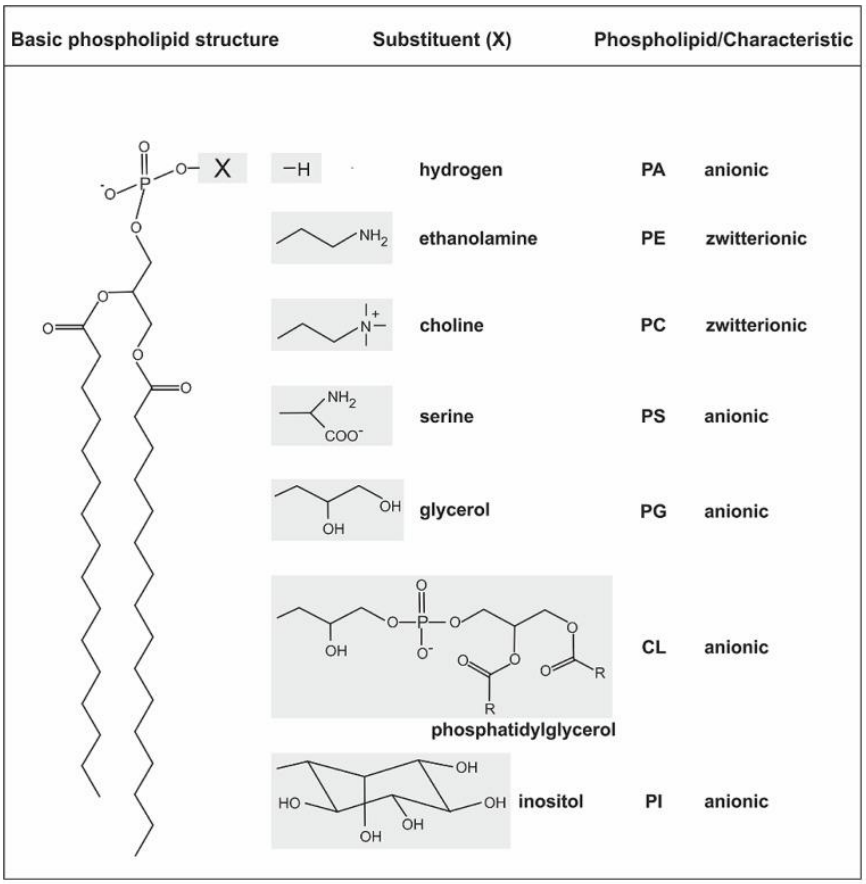

Figure 4.1- ***General structure of phospholipids and common head groups.*** *PLs contain two fatty acids ester-linked to glycerol at C-1 and C-2, and a polar head group attached at C-3 via a phosphodiester bond. The fatty acids in PLs can vary in carbon group length and saturation degree. The different common polar head groups and global charges of the phospholipid molecule at neutral pH are indicated. PA, phosphatidic acid; PE, phosphatidylethanolamine; PC, phosphatidylcholine; PS, phosphatidylserine; PG, phosphatidylglycerol; CL, cardiolipin; PI, phosphatidylinositol. Taken from (Aktas et al., 2014)*

Another class of structural lipids is formed by the SLs, whose hydrophobic backbone is constituted by ceramide (Cer), consisting of a sphingoid base (such as sphingosine; Sph), which is amide-linked to a fatty acid (Figure 4.2A). The major SLs in mammalian cells is sphingomyelin (SM), which, like PC, contains a phosphocoline head, and the glycosphingolipids (GSLs), which contain mono-, di- or oligosaccharides based on glucosylceramide (GlcCer) and sometimes galactosylceramide (GalCer). These are important components in nerve cell membranes, where they have essential roles in the structure and function of myelin, the insulator that allows for rapid nerve conduction. SLs are usually the cell membrane components with the highest main phase transition

temperature (T_m), *i.e.*, the temperature at which the lipids undergo a transition from a gel (or solid-ordered, s_o) phase, with the acyl chains highly ordered and packed to a fluid phase, with low order and packing (l_d phase) (Marquês *et al.*, 2015). Therefore, SLs hold large responsibility for the lateral segregation of lipids and are important components of membrane ordered domains (Figure 4.3). The fact that they have high T_m values means that at room temperature, at inner human body temperature (37 °C), or at the optimal growth temperature of many microorganisms (e.g., 30 °C for *Saccharomyces cerevisiae*), if isolated, they could exist in a gel or S_o phase, rather than in the fluid state usually attributed to biological membranes.

The SLs are fluidized by sterols (cholesterol, in mammalian cell membranes; Figure 4.2B), another class of lipids constituents of eukaryotic membranes. Sterols contain a tetra-ring hydrophobic core based on the cyclopentane-*per*-hydro-phenantrene motif, which can be further extended with an aliphatic chain, and bearing only a hydroxyl group as the polar part (Bloch, 1957). The preferential interaction between high Tm SLs and cholesterol is of the utmost importance, as it allows the formation of specialized microdomains, the so-called 'lipid rafts' (Figures 4.2C and 4.3) (Korade & Kenworthy, 2008; Brown & Galea, 2010; de Almeida & Joly, 2014). These domains are in a state resembling a liquid-ordered (l_o) phase, with an acyl chain order similar to the gel phase, but lateral diffusion on the same order of magnitude as the l_d phase (thereby, also considered fluid) (Bastos *et al.*, 2012). Moreover, they are usually defined as small, highly dynamic and transient plasma membrane entities, serving as platform for various cellular processes such as signal transduction and transport (Pike, 2006; Lingwood et al., 2009; Lingwood & Simons, 2010; Sonnino & Prinetti, 2010; Simons & Sampaio, 2011). Although these lateral assemblies can arise solely due to lipid-lipid interactions, in cell membranes lipid-protein and protein-protein interactions also play a vital role in the formation, properties and function of these domains (Castro *et al.*, 2007; Smith, 2012; Barrera *et al.*, 2013; Escribá & Nicolson, 2014).

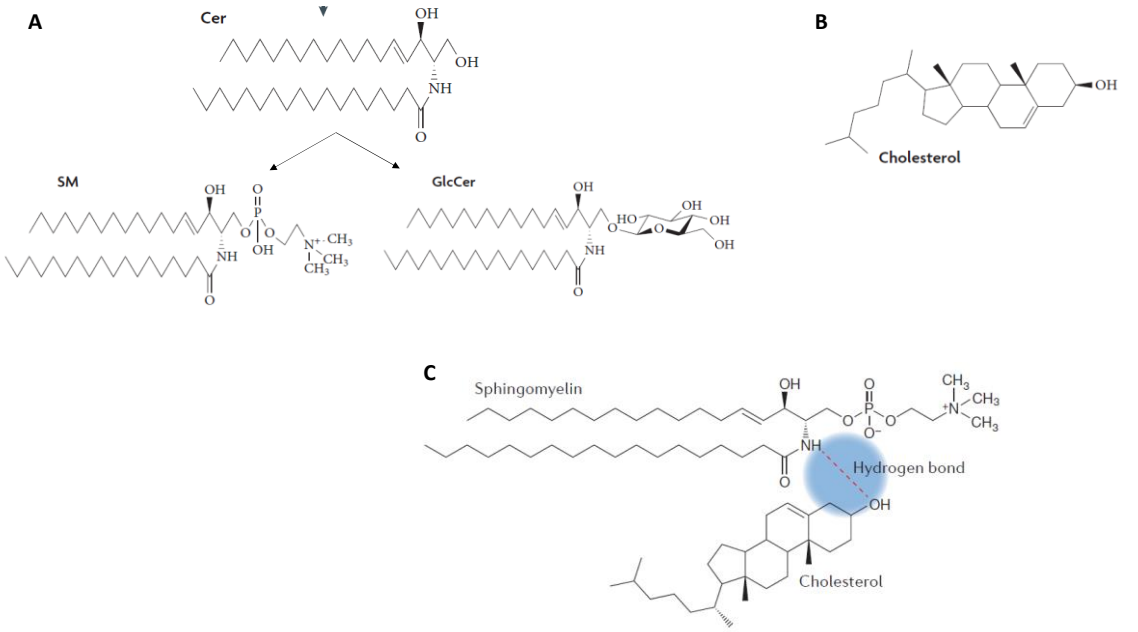

Figure 4.2- ***Main constituents of the lipid rafts****. A) The phosphosphingolipid sphingomyelin (SM) and the glycosphingolipid glucosylceramide (GlcCer) have a ceramide (Cer) backbone, consisting of a sphingoid base (such as sphingosine; Sph), which is amide-linked to a fatty acid. SM contains a phosphocoline headgroup, and in GlcCer the sugar residue attached to ceramide is glucose. B) cholesterol, the sterol of mammalian cell membranes. Adapted from (Van Meer et al., 2008) C) Defining feature of lipid raft formation. The preferential interaction between sphingolipids and sterols is due to the saturation of sphingolipid hydrophobic tails, but also to hydrogen bonding between these lipid species. The amide of the sphingolipid backbone can both donate and accept a hydrogen bond, and these hydrogen bonds are within the interfacial region of the membrane, in which the relative scarcity of water increases the stability of these bonds. Adapted from (Sezgin et al., 2017).*

4.2 Membrane Probes sensitive to different lipid domains

The study of lipid microdomains requires the use of noninvasive, highly sensitive techniques with minimal perturbation of cellular integrity and function. Fluorescence spectroscopy is extensively used for monitoring membrane heterogeneity, due to its intrinsic sensitivity, suitable time scale, and minimum perturbation (Pucadyil & Chattopadhyay, 2004; Mukherjee et al., 2007). Thus, fluorescence techniques are suitable for this task, by providing direct information on molecular interactions and dynamic events involving biomolecules. As most lipids do not display intrinsic fluorescence, one needs to label the bilayer with an extrinsic fluorophore (membrane probe). Several fluorescence properties of membrane probes can be determined - spectral shifts, fluorescence lifetimes, and fluorescence anisotropy -, which enables us to retrieve information about the physical properties of the membranes, such as order, charge distribution, polarity, and hydration. There are, in general, no probes that label

exclusively a certain type of domain. Therefore, the fluorescence signal is most of the time a composition of the fluorescence from the probe incorporated in different types of domains (Bastos *et al.*, 2012).

Membrane probes include fluorescent molecules reminiscent of natural lipids. In the present study, I have used 1,6- diphenyl-1,3,6-hexatriene (DPH) and *trans*-parinaric acid (*t*-Pna), two of the most commonly used membrane probes in fluorescence spectroscopy studies (Figure 4.3). The former distributes evenly among most membrane domains, thus giving an indication of the average or global order of the lipid bilayer (Lentz & Burgess, 1989). The partitioning property of DPH is particularly advantageous since it reports the phase-averaged rotational properties of fatty acyl chains without bias toward a particular type of membrane domain. The latter partitions preferentially into gel domains, where it displays increased fluorescence quantum yield (Sklar *et al.*, 1977), thus being especially sensitive to changes in the amount and composition of those ordered domains (de Almeida *et al.*, 2009). The strong preference for such domains makes it possible to detect gel domains even when these constitute less than 5% of the membrane (Castro *et al.*, 2009; Marquês *et al.*, 2015). The probe *t*-PnA presents the additional benefit of displaying a long lifetime component in its fluorescence intensity decay that is characteristic of the type of ordered domains being detected, namely gel or s_o (if clearly above 30 ns) or l_o (below 30 ns) domains (Reyes Mateo *et al.*, 1993*a*, 1993*b*; Castro *et al.*, 2009). Both pertain to a very important class of membrane probes because they align parallel to the acyl chains of phospholipids/sphingolipids in lipid bilayers and their fluorophore locates at the hydrophobic core of the bilayer. Therefore, their fluorescence properties reflect very faithfully direct information on acyl chain packing (Bastos *et al.*, 2012). In addition, the labeling of membranes with these probes renders a low background noise, given their strong and fast partition into the membranes, and low quantum yield in water. Another important feature is their cylindric shape, resulting in minimal perturbation in the system. Thus, the results can be interpreted without taking into consideration biophysical complexities on the lipid-water interface/lipid headgroup region or interactions with extra membrane molecules or domains of membrane proteins (Bastos *et al.*, 2012). The concomitant application of DPH and *t*-Pna can be used to obtain an unbiased or quantitative description of the lipid domains behavior (de Almeida *et al.*, 2009; Castro *et al.*, 2009; Aresta-Branco *et al.*, 2011; Bastos *et al.*, 2012). However, these probes cannot

be used in fluorescence microscopy due to absorption and emission mostly in the UV spectral region and photobleaching (Bastos *et al.*, 2012).

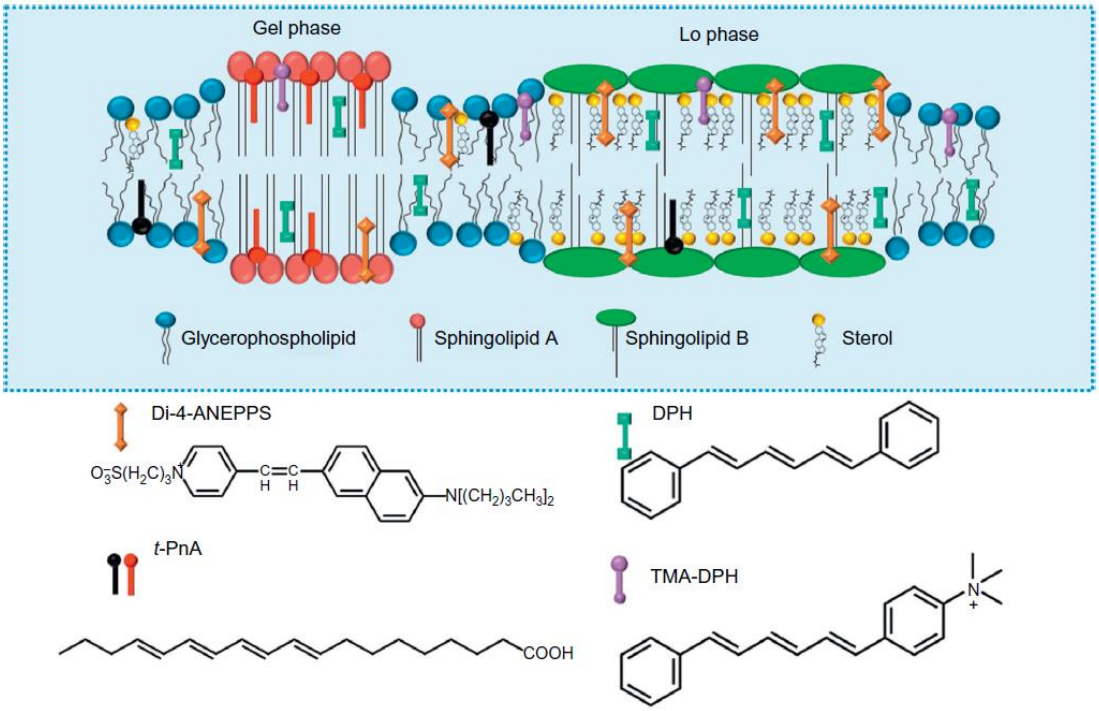

Figure 4.3- ***Schematic depiction of a lipid bilayer exhibiting different lipid phases—Ld, Lo, and gel****. The predicted location of fluorescent probes, such as di-4-ANEPPS, 1,6-diphenyl-1,3,5-hexatriene (DPH), trans-parinaric acid (t-Pna), and 1-(4-trimethylammoniumphenyl)-6-phenyl-1,3,5-hexatriene (TMA-DPH), in the different lamellar lipid phases is also depicted. The polar headgroups of sphingolipids are represented in red and green (types A and B), and that of phospholipids in blue. Sterols (Lo-forming) are represented by a ring system. Di-4-ANEPPS presents sensitivity to polarity and hydration patterns in the headgroup region, and membrane dipole potential; partition and fluorescence quantum yield favourable to sterol-rich domains; DPH reports the global order of the membrane in the hydrophobic core; t-PnA reports acyl chain packing, has preferential partition for gel phases (red t-PnA), but can be found also in Lo and Ld phases where it presents intermediate and lower quantum yield, respectively (black t-PnA); TMA-DPH, similar to DPH, reports the global order of the membrane, but is anchored at the membrane surface by the TMA group and is more sensitive to hydration. In the present work, I have only used t-Pna and DPH. Taken from (Marquês et al., 2015).*

4.3 Fluorescence spectroscopy – principles and types of measurements

Fluorescence spectroscopy is extensively used in the study of biological membranes, mostly due to its intrinsic sensitivity, suitable time scale, and minimum perturbation, as explained above (Pucadyil & Chattopadhyay, 2004; Mukherjee et al., 2007). By assessing the fluorescence properties of the molecular probes located within the membrane, it allows the study of a vast variety of physical parameters: fluidity; structural ordering;

lipid – protein interactions; location of proteins; lateral organization (in the membrane plane); membrane potentials and molecular mobility (Valeur & Berberan-Santos, 2012).

The fundamentals of fluorescence can be illustrated in a Jablonski energy diagram (Jabłoński 1935), more recently baptized as Perrin- Jabłoński (Valeur & Berberan-Santos, 2012). Schematically, this diagram shows different energetic states of a chromophore after absorption of a photon, where transitions between them are depicted with arrows (Figure 4.4).

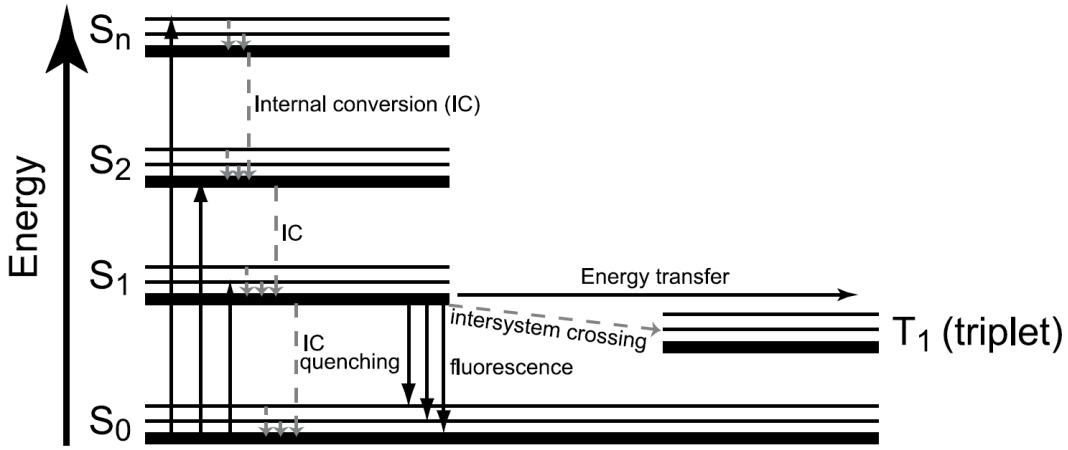

*Figure 4.4- **The Jablonski energy diagram**. Light absorption and emission are represented by vertical, black arrows. Vibrational relaxation, internal conversion and intersystem crossing are indicated by light gray dashed arrows. Taken from (Laptenok, 2009).*

Absorption of a photon by a fluorophore leads to the transition of an electron from the ground state, a singlet for most common organic chromophores (S_0) to an excited state (S_n). The excitation then rapidly (10^{-13} s) relaxes non-radiatively to the lowest excited state (S_1) via vibrational relaxation and internal conversion (IC). From S_1 the fluorophore can then relax to S_0 in several ways: non-radiatively by IC, by intersystem crossing forming a triplet state, by quenching, by energy transfer to another fluorophore (FRET) or by fluorescence (emission of a photon).

Fluorescence measurements can be broadly classified into two types: steady-state and time-resolved. Steady-state measurements, the most common, are those performed with constant illumination and observation. The sample is illuminated with a continuous beam of light, and the intensity or emission spectrum is recorded. The combination of a constant

flow of photons, with a nanosecond timescale of fluorescence, results in a constant (steady-state) concentration of excited fluorophore.

The second type of measurement is time-resolved, which is used for measuring fluorescence intensity decays or anisotropy decays. For these measurements the sample is exposed to a pulse of light, where the pulse width is typically shorter than the decay time of the sample. This intensity decay is recorded with a high-speed detection system that permits the intensity or anisotropy to be measured on the nanosecond timescale. A steady state observation is simply an average of the time-resolved phenomena over the intensity decay of the sample (Lakowicz, 2006). It should also be stressed that time-resolved techniques have the advantage of not evaluating the total intensity, so they are much less biased by the known problems associated to steady-state data such as light scattering, or error in probe concentration (de Almeida *et al.*, 2009).

4.3.1 Steady-state fluorescence anisotropy. Into the rigidity of biological membranes derived from rotational dynamics of excited molecular probes

Fluorescence anisotropy ($\langle r \rangle$) measurements provide information on the size and shape of proteins or the rigidity of various molecular environments. Anisotropy measurements are based on the principle of photoselective excitation of fluorophores by polarized light. Fluorophores preferentially absorb photons whose electric vectors are aligned parallel to the transition moment of the fluorophore. Upon excitation with polarized light, one selectively excites those fluorophore molecules whose absorption transition dipole is parallel to the electric vector of the excitation. Fluorophores absorb light along a particular direction with respect to the molecular axes. For example, DPH only absorbs light polarized along its long axis.

Several phenomena can decrease the measured anisotropy to values lower than the maximum theoretical values. The most common cause is rotational diffusion. Such diffusion occurs during the lifetime of the excited state and displaces the emission dipole of the fluorophore. Measurement of this parameter provides information about the relative angular displacement of the fluorophore between the times of absorption and emission.

The extent to which a fluorophore rotates during the excited-state lifetime determines its polarization or anisotropy, which can be defined by

$$\langle r \rangle = \frac{(I_{VV} - G \times I_{VH})}{(I_{VV} + 2 \times G \times I_{VH})} \qquad \textit{(Equation 4.1)},$$

where the different intensities, *I*, are the vertical and horizontal components of fluorescence emission in steady-state with vertical (I_{VV} and I_{VH}, respectively) and horizontal (I_{HV} and I_{HH}, respectively) excitation relatively to the emission axis. G factor is used to correct the different sensitivity of the detector for the vertical and horizontal polarization.

In fluid solution most fluorophores rotate extensively in 50 to 100 picoseconds. Hence, the molecules can rotate many times during the 1–10 nanoseconds excited-state lifetime, and the orientation of the polarized emission is randomized. For this reason, fluorophores in non-viscous solution typically display anisotropies near zero. The effects of rotational diffusion can be decreased if the fluorophore is bound to a macromolecule. Thus, measurements of fluorescence anisotropy will be sensitive to any factor that affects the rate of rotational diffusion. The rotational rates of fluorophores in cell membranes also occur on the nanoscale timescale, and the anisotropy values are thus sensitive to membrane composition (Lakowicz, 2006). That said, if the fluorophore is confined to a rigid environment it will not freely rotate, yielding higher values of anisotropy (typically > 0.3). Conversely, if the fluorophore is contained in a more fluid medium, where it can rotate more freely, emitted light will not exhibit a preferential polarization orientation. In this case, one will obtain lower values of anisotropy.

4.3.1.1 Technical instrumentation used in steady-state fluorescence anisotropy

To perform fluorescence anisotropy measurements, one needs to use a spectrofluorometer device which must be equipped with polarizers, as exemplified in Figure 4.5. Briefly, xenon arc lamps are the light source generally used due to their high intensity at all wavelengths ranging upward from 250 nm. These lamps produce excitation light that follows an optical pathway where monochromators motorize/select both the excitation and emission wavelengths. The excitation monochromator, for instance, contains two gratings, which decreases stray light, that is, light with wavelengths different from the

chosen one. In fluorescence anisotropy measurements, the light that is not reflected by the beam splitter passes through a polarizer before reaching the sample chamber. The light emitted by the sample in a direction perpendicular to the incident beam may encounter an emission polarizer prior to a subsequent emission wavelength sieve in the emission monochromator. Finally, the fluorescence is detected with a photomultiplier tube and quantified with the appropriate electronic devices. The output is usually presented in graphical form and stored digitally.

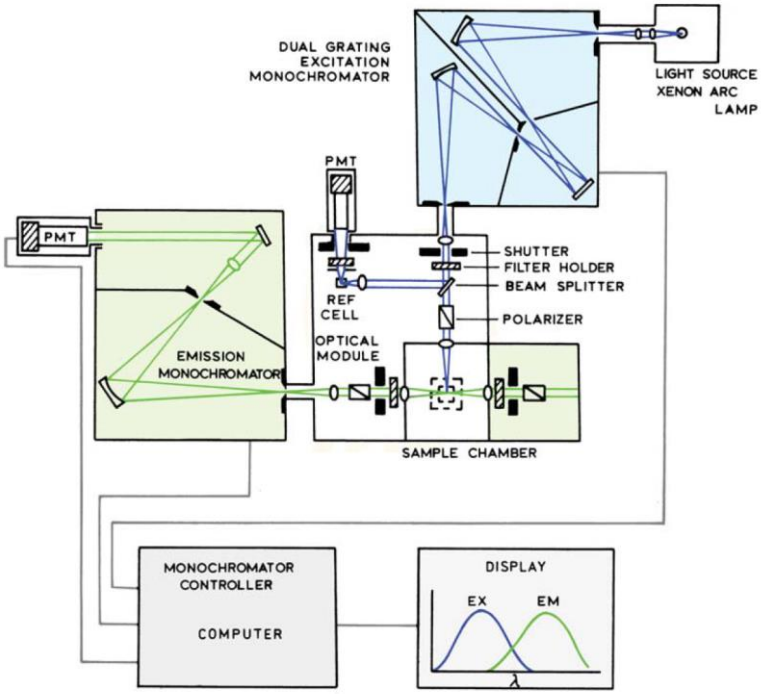

Figure 4.5- ***Schematic representation of the optical pathway in a conventional fluorometer****. Taken from (Lakowicz, 2006)*

4.3.2 Time-resolved fluorescence intensity decays. Into the organization of biological membranes

Time-resolved fluorescence spectroscopy, in particular the determination of fluorescence lifetimes, is a technique often used in membrane biophysics that allows to retrieve crucial information about the organization of the membrane, namely the presence of certain types of lipid domains, the packing of the acyl chains or the extent of water penetration (de Almeida *et al.*, 2009).

Time-resolved fluorescence gives information on the kinetics of fluorescence emission and excited-state lifetimes, that is, the average time the fluorophore spends in the excited state attained after light absorption and prior to fluorescence emission or deactivation by other processes. Fluorescence lifetimes, usually in the order of nanoseconds, are sensitive to biomolecule dynamics, solvent relaxation, and presence of other molecules (concentration and diffusion coefficient) that decrease the excited-state lifetime (Bastos *et al.*, 2012).

Since the emission probability decreases with time after excitation, a fluorescence intensity decay is obtained. The simplest kinetics of fluorescence emission is a first order law (exponential decay) and the fluorescence (or excited-state) lifetime is the reverse of the decay rate constant. However, in most cases, the fluorescence decay is more complex and is usually described by a sum of exponentials,

$$I(t) = \sum_{i=1}^{n} \alpha_i e^{(-t/\tau_i)} \qquad \textit{(Equation 4.2)},$$

where α_i and τ_i are the normalized amplitude and lifetime of component i, respectively. More specifically, α_i is a pre-exponential factor representing the fractional contribution to the time-resolved decay of the component with a lifetime τ_i, such that $\sum_i \alpha_i = 1$. Multicomponent decays are indications of heterogeneity and, at the same time, give information on the biophysical properties and relative abundance of the lipid domains that are responsible for the appearance of each lifetime. Thus, when resolution of multiple exponentials is possible, the lifetime components together with their amplitudes contain information on the type and relative abundance of domains (de Almeida *et al.*, 2009; Bastos *et al.*, 2012).

Sometimes, due to the unclear physical meaning of each exponential used in the fit to the experimental decay curve, it is useful to describe the fluorescence kinetics through a parameter named mean or average fluorescence lifetime (the true mean lifetime of the excited state since it is weighted by the intensity of each component), given by

$$\langle \tau \rangle = \frac{\sum_i \alpha_i {\tau^2}_i}{\sum_i \alpha_i \tau_i} \qquad \textit{(Equation4.3)}$$

In some cases, where there is a dependence of the quantum yield with the interaction under studied, the determination of the quantum yield-weighted lifetime $(\bar{\tau})$ (also named as amplitude-weighted average fluorescence lifetime) becomes more significant. This parameter can be determined as follows

$(\bar{\tau}) = \sum_i \alpha_i \tau_i$ *(Equation 4.4)*

4.3.2.1 Technical instrumentation used in time-resolved fluorescence intensity decays

Time-resolved experiments are often performed through direct measurements in the time domain, in which a short pulse of light excites the sample, and the subsequent fluorescence emission is recorded as a function of time. This is generally achieved using time-correlated single photon counting (TCSPC), which uses electronics to detect single-photon events at a detector. By repeating many start-stop signals, a histogram of single-photon counts in discrete time channels is obtained (O'Connor & Phillips, 1984; Lakowicz, 2006; Wahl, 2014). The technique of TCSPC consists in exciting the sample and detecting the arrival time of the first emitted photon. Therefore, this technique is also called single photon timing (SPT) (de Almeida *et al.*, 2009). In the experiments of this thesis, a nanoLED, which emits light pulses of short duration (70 ps) and a repetition rate up to 1 MHz, was used as the light source.

If the condition for detecting a single photon after excitation pulse is fulfilled, *i.e.*, only one fluorescence photon per excitation pulse is detected and there are no photons coming from the sample during the "dead time" of the setup, the probability of detecting a photon in channel *i* is proportional to the fluorescence intensity at delay time *i*, meaning that the histogram of photon arrival times is proportional to the fluorescence intensity decay (Figure 4.6) (Laptenok, 2009).

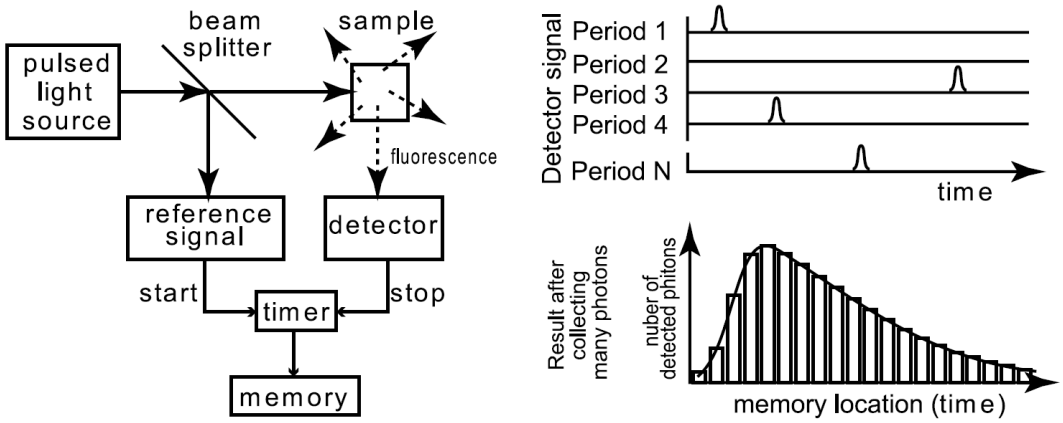

*Figure 4.6- **Time-correlated single photon counting (TCSPC) principle**. The arrival time of the first photon after the excitation pulse is measured and stored in the memory. The histogram of the arrivals times of photons represents the fluorescence intensity versus time curve. Taken from (Laptenok, 2009).*

4.4 Materials and Methods

4.4.1 Chemicals

1-Palmitoyl-2-oleoyl-*sn*-glycero-3-phosphocholine (POPC), 1,2-Dipalmitoyl-*sn*-glycero-3-phosphoethanolamine (DPPE) and N-palmitoyl-sphingomyelin (PSM) were purchased from Avanti Polar Lipids (Alabaster, AL); cholesterol was purchased from Sigma (St. Louis, MO). Ludox (colloidal silica diluted to 50 weight % in water) was purchased from Sigma. *Trans*-parinaric acid (*t*-PnA) was purchased from Santa Cruz Biotechnology (Santa Cruz, CA, USA), and 1,6-diphenyl-1,3,5-hexatriene (DPH) from Invitrogen (Madrid, Spain). Solvents for lipid and probe stock solutions were spectroscopic grade. All other reagents were of the highest purity available.

4.4.2 Plasma membrane-enriched fraction isolation

Hippocampal plasma membrane fractions were prepared as described previously (Sun *et al.*, 1988) with some modifications. Briefly, hippocampi from fed and fasted rats were homogenized in ice-cold homogenization buffer - 0.32M sucrose, 50mM Tris HCl (pH7.4), 1mM EDTA, 2mM EGTA, 1x protease inhibitor cocktail from Roche® Diagnostics -, using a glass tissue homogenizer pestle, and centrifuged for 10min at 500*g* to sediment nucleus and cell debris. The supernatant was centrifuged at 18800*g*, for 20min, to obtain a crude mitochondrial pellet. The post-mitochondrial supernatant was centrifuged at 45500*g* for 30min, which resulted in the sedimentation of a white-colored pellet. This pellet, constituted by the crude plasma membranes, was resuspended in a minimum volume of PBS buffer (in mM): K_2HPO_4, 1.8; NaH_2PO_4, 10; NaCl, 137; and KCl, 2.7 (pH 7.4), with 1x protease inhibitor cocktail. The protein concentration was determined by the bicinchoninic acid (BCA) protein assay kit (Micro BCA Pierce Thermo®) using BSA as a standard. Plasma membrane-enriched fractions were stored at 4ºC until use. All steps were performed on ice and centrifugations at 4ºC.

4.4.3 Total lipids extraction

Lipids were extracted by the method of Bligh and Dyer (Bligh & Dyer, 1959). Briefly, for each 1 ml of sample, 3.75 ml of 1:2 (v/v) chloroform-methanol ($CHCl_3$:MeOH) was added and vortexed thoroughly for 1 min. Then 1.25 ml of $CHCl_3$ was added and vortexed

thoroughly for 1 min. Finally, 1.25 ml of 1 M NaCl was added and again vortexed thoroughly for 30 sec. Samples were centrifuge at 1,000 *g* for 5 min at room temperature to give a two-phase system (aqueous top, organic bottom) and the bottom phase was recovered and dried under a mild flow of nitrogen, forming a thin layer of lipid in the bottom of the tube. Total lipid concentration was determined by gravimetry. The dried extracts were resuspended in a mixture of $CHCl_3$:MeOH (1:1).

4.4.4 Phospholipid and cholesterol quantification

An aliquot of lipid extract was transferred to a test tube and organic solvent evaporated. Concentration of phosphate (inorganic) was determined with a colorimetric reagent (ascorbic acid/ammonium heptamolybdate) subsequently to total lipid digestion by perchloric acid using Na_2HPO_4 as standard (Rouser *et al.*, 1970). Cholesterol concentration was estimated by direct treatment of the lipid extracts with a reagent composed of ferric chloride dissolved in a glacial acetic acid-sulfuric acid mixture (Zlatkis *et al.*, 1953). Both concentrations were determined spectrophotometrically, with the following wavelength (λ(nm)): 797 and 550, for phospholipids and cholesterol determination, respectively.

4.4.5 Membrane preparation for fluorescence spectroscopy measurements

DPH and *t*-Pna were added from a concentrated stock solution to membranes at a final probe concentration of 0.5 and 1mol%, respectively, with respect to total phospholipid content. Membranes containing 50 nmol of total phospholipids were suspended in 1ml of PBS buffer and used for fluorescence spectroscopy experiments. The resultant probe concentration was 0.25µM and 0.5µM for DPH and *t*-Pna, respectively. These conditions have ensured optimal fluorescence intensity with negligible membrane perturbation. Probes were incubated for 10 min, at room temperature. Probe concentrations in stock solutions were determined spectrophotometrically using ε(DPH, 355 nm, chloroform) = 80.6 x 10^3 $M^{-1}cm^{-1}$ and ε(*t*-PnA, 299.4 nm, ethanol) = 89 x10^3 $M^{-1}cm^{-1}$ (Castro *et al.*, 2007). Blank samples were prepared the same way except that probes were omitted.

4.4.6 Fluorescence spectroscopy measurements

The fluorescence measurements were carried out on a Spex Fluorolog 3-22/Tau 3 spectrofluorometer equipped with double grating monochromators in both excitation and emission light paths from Horiba Jobin Yvon at 23ºC, using 1cm path length quartz cuvettes.

For steady-state measurements (450 W Xe arc lamp light source), the samples were under constant magnetic stirring, and the excitation / emission wavelengths were 358nm / 430nm for DPH and 303nm / 404 nm for t-PnA. The steady-state anisotropy (<*r*>) was calculated according to *equation 1*. An adequate blank was subtracted from each intensity reading. The set of the four intensity components for each sample, depicted in *equation 4.1*, was measured seven times.

For time-resolved measurements by the single photon counting technique, nanoLED N-320 (Horiba Jobin Yvon) was used for the excitation of t-PnA, and emission wavelength was 404 nm. The resolution of the detection system was 50 ps. The number of counts on the peak channel was 20,000. The number of channels per curve used for the analysis was ~1000. The timescale was 0.1114 ns/channel. Ludox was used as the scatter to obtain the instrumental response function. The program TRFA Data Processor v.1.4 (Scientific Software Technologies Center, Minsk, Belarus) was used for the analysis of the experimental fluorescence decays.

A sum of exponentials (*Equation 4.2*) was used to describe the fluorescence intensity decay and the mean fluorescence lifetime was calculated according to *equation 4.3*. The goodness of the fit of a given set of observed data was evaluated by the reduced $\chi 2$ ratio, the weighted residuals, and the autocorrelation function of the weighted residuals. A fit was considered acceptable when plots of the weighted residuals and the autocorrelation function showed random deviation around zero, with a minimized $\chi 2$ value not larger than 1.4. Four exponentials were required to described *t*-Pna fluorescence intensity decays. The background (obtained with the blank sample) was subtracted from the decay.

All the data represents the mean ± SEM of 4 independent samples.

4.4.7 Thin Layer Chromatography

Individual phospholipids classes and neutral lipids were separated by thin layer chromatography (TLC). Whatman silica gel-60 plates (20 × 20 cm, 250 μm, GE Healthcare, England) were heat-activated at 110°C for 1 h, and samples (with 20 μg of phospholipids) were streaked onto the plates. Phospholipids were separated using chloroform/methanol/acetic acid/acetone/water solvent system (35:25:4:14:2, Xu *et al.*, 1996), which separates all major glycerophospholipids. Phospholipids were detected by staining with Coomassie brilliant blue (Nakamura & Handa, 1984). The mixture of standard phospholipids was constituted by POPC, DPPE, PSM and cholesterol. Their concentrations in stock solutions made in chloroform were determined by gravimetry.

4.5 Influence of feeding cycle on lipid organization and composition of neuronal plasma membrane

A fractionation protocol has been applied to obtain plasma membrane-enriched fractions from rat hippocampus (Sun *et al.*, 1988), which were subsequently labeled with the molecular probes DPH and *t*-Pna. This important fractionating step allowed me to overcome expected incorporations of the fluorescence membrane probes into intracellular compartments (Aresta-Branco *et al.*, 2011; Bastos *et al.*, 2012). These two probes present different phase partitioning behavior; DPH distributes indistinctly between gel and fluid phases, whereas *t*-PnA presents a high preference for gel phase domains, being therefore an exceptional reporter of this gel phase. Consequently, by combining these two membrane probes complementary information is obtained (Castro *et al.*, 2007).

The fluorescence properties of DPH and *t*-Pna were characterized by fluorescence spectroscopy techniques, mainly steady-state anisotropy and time-resolved fluorescence intensity decay.

4.5.1 Fluorescence spectroscopy

4.5.1.1 Anisotropy measurements

Fluorescence anisotropy is correlated to the rotational diffusion of probes embedded in membranes, which is highly sensitive to the packing of lipid acyl chains. The premise that, for both probes used here, the fluorescence anisotropy is high in the gel and low in the fluid, allows for a detailed characterization of the lipid phases encountered in the PM of rat hippocampus.

To understand how the whole membrane system may respond to cellular alterations brought up by the feeding cycle, the PM-enriched fractions were labeled with DPH, a probe that is sensitive to its global properties. Its steady-state fluorescence anisotropy is a well-established parameter to report on the alterations undergone in the global order of the membrane (de Almeida *et al.*, 2003, 2005; Aresta-Branco *et al.*, 2011).

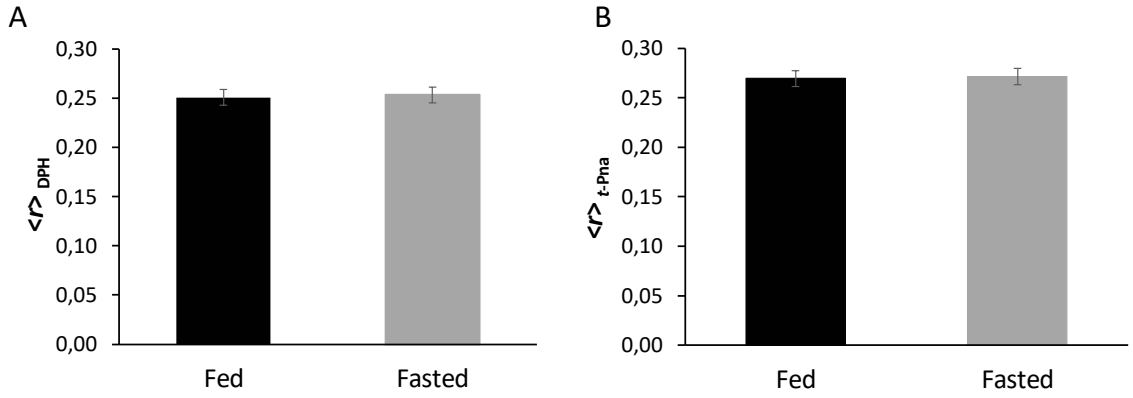

Figure 4.7- ***Feeding cycle does not influence the order of plasma membrane domains of rat hippocampus at the level of the hydrophobic core.*** *The steady-state fluorescence anisotropy of A) DPH and B) t-PnA was obtained from isolated plasma membrane of fed (black) and fasted (grey) animals. The values are the mean ± SEM of four independent experiments.*

Figure 4.7A shows that the fluorescence anisotropy of DPH is practically the same between fed and fasted membranes (0.25 in both membranes), meaning that feeding cycle does not alter the global order/fluidity of PM of rat hippocampus. This anisotropy value, consistent with another work performed in crude membranes of rat hippocampus (Schaeffer *et al.*, 2011), unveils that the PM of rat hippocampus is overall highly ordered (anisotropy of DPH higher than 0.2). The fluorescence anisotropy values measured for DPH corresponds, roughly, to the one measured for the membrane models mimicking l_o domains, composed by the 1:1:1 equimolar mixture of POPC/PSM/cholesterol, at 23ºC (de Almeida *et al.*, 2003).

On the other hand, the fluorescence anisotropy of *t*-Pna (0.27 in both membranes; Figure 7B) indicates that the PM of rat hippocampus does not contain a significant fraction of s_o domains, whose typical anisotropy values are higher than 0.3. Additionally, the fact that anisotropy of *t*-Pna is only slightly larger than that of DPH indicates that PM of rat hippocampus is mainly characterized by l_d/l_o domains. The quantum yield of *t*-PnA is moderately higher in this phase (Castro *et al.*, 2007). Feeding cycle also does not alter the anisotropy of *t*-Pna, which indicates that the lateral heterogeneity of the most ordered domains of rat hippocampus does not change whether the animals have or not been fed. Considering the values obtained, one can conclude that l_o-like domains probably predominate in the plasma membrane crude extract, as expected from the composition reported for the neuronal membrane (Ingólfsson *et al.*, 2017) (see also next section).

4.5.1.2 *Fluorescence lifetime measurements*

Fluorescence lifetime distribution analysis of membrane probes represents a powerful and sensitive tool in characterizing the membrane organization and dynamics through the heterogeneity of population of the probe. The quantum yield of the probes used in this work behaves differently, *i.e.*, whereas the DPH quantum yield is weakly sensitive to the lipid phase, *t*-PnA presents quantum yield values and fluorescence lifetime components that are typical of each lipid phase. Thus, the plasma membrane of rat hippocampus was labeled with *t*-PnA, and the fluorescence decay of the probe was obtained (Figure 4.8).

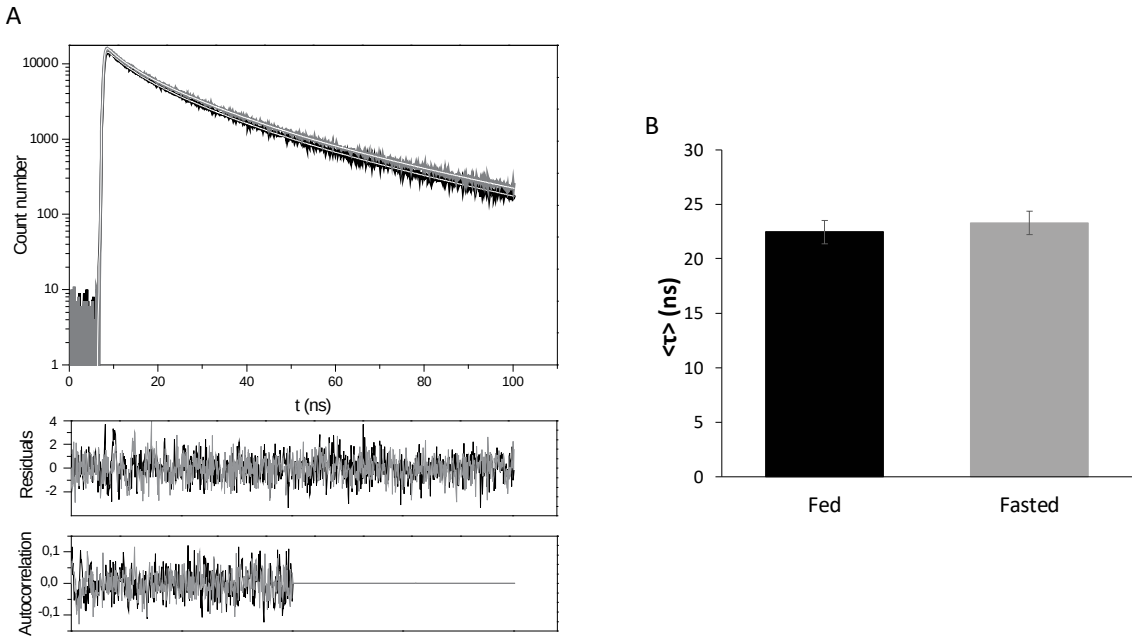

Figure 4.8- ***Feeding cycle does not alter the fluorescence lifetime of t-Pna****. A) Fluorescence intensity decay and B) mean fluorescence lifetime of t-Pna was obtained from fed (black) and fasted (grey) membranes. In A), top panel: the fluorescence intensity decay was better described by a sum of 4 exponentials (white lines, equation 4.2), and the long lifetime component indicates the presence of gel domains in the PM of rat hippocampus. Middle panel: random distribution of weighted residuals of the fitting. Bottom panel: autocorrelation of the residuals. In B), results are mean ± SEM of four independent experiments.*

The fluorescence intensity decays of *t*-Pna presented in Figure 8A disclose a similar pattern between fed and fasted membranes. A long lifetime component higher than 30ns was detected in both cases, which reveals the presence of a gel phase, *i.e.* a s_o phase (Castro *et al.*, 2009; Bastos *et al.*, 2012). This similitude is also depicted in the values obtained for the mean fluorescence lifetime of *t*-Pna, as follows: 22.5 ± 1.06 ns and 23.3 ± 1.35 ns, for fed and fasted membranes, respectively (Figure 4.8B). Again, these values are close to the ones measured in model systems with an equimolar mixture of POPC/PSM/cholesterol (de Almeida *et al.*, 2005). These results indicate that the time that

t-Pna spends in an excited state before relaxation to a fundamental state is the same in fed and fasted conditions, which means that the physical properties of the ordered domains of rat hippocampus does not undergo modifications during the feeding cycle.

The detection of multi-exponentials allows a deeper analysis on what the heterogeneity of lipid domains is concerned. *t*-PnA presents quantum yield values and fluorescence lifetime components that are typical of each lipid phase (Castro *et al.*, 2007, 2009). Hence, the relative amplitude of each component gives us an overall idea of the abundance of the lipid domains in the PM of rat hippocampus (Figure 4.9).

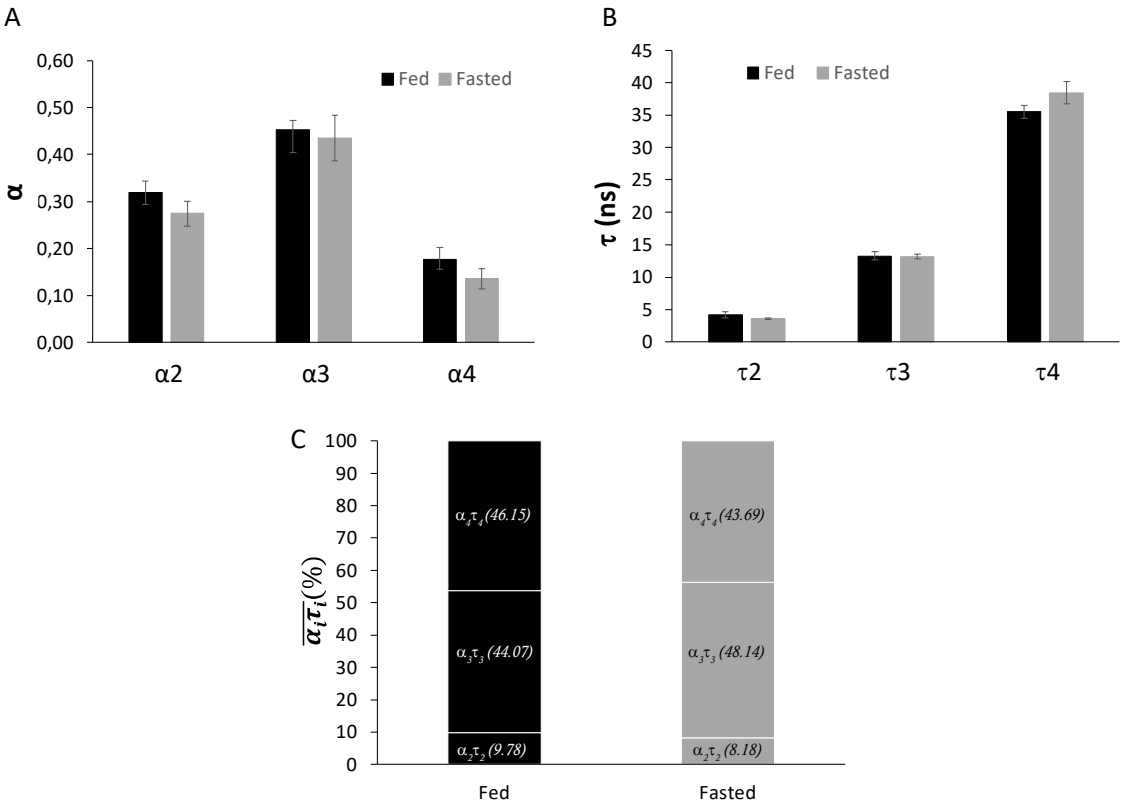

*Figure 4.9- **Analysis of the individual components constituents of the fluorescence lifetime of t-Pna.** A) Normalized amplitude and B) lifetime (ns) values of the components obtained from plasma membrane-enriched fractions of hippocampus from fed (black) and fasted (grey) animals. Values are mean ± SEM of four independent experiments. C) Fraction of the product $\alpha_i\tau_i$ weights the relative abundance of lipid domains and the preference of t-Pna for highly ordered domains. The first component was not considered here because it reflects the most fluid lipid domains, where the t-Pna presents marginal partition, and hence, negligible small values (α1<0.1 and τ1<0.05ns), similar to the instrumental response function obtained from the fluorescence intensity decay of the scatter used (Ludox)*

Accordingly, the α3 component is representative of the cholesterol-enriched l_o domains, as the correspondent fluorescence lifetime (τ3) is reminiscent of those obtained for ordered domains in mammalian cells (smaller than 21ns) (Schroeder *et al.*, 1984, 1987).

Thus, the larger contribution of α3 (45% and 43% of the total components, in fed and fasted membranes, respectively; see Figure 4.9A) is linked to the high demand of neuronal cells for l_o domains, where the specialized microdomains (or lipid rafts) are exclusively localized. In other words, these results indicate that lipid rafts are responsible for almost 50% of the total lipid domains in PM of rat hippocampus. The second most abundant lipid domain is enclosed in α2, with fluorescence lifetime values < 5ns (Figure 4.9B), characteristic of (poly)unsaturated phospholipid-enriched l_d domains. This component accounts for an overall contribution of 30% to the PM. The results concerning α2 and α3 components suggest that the PM of rat hippocampus is mainly constitutes by l_d-l_o domains, as previously indicated by the results obtained from the fluorescence anisotropy.

As far as I can tell from the literature, this is the first time that *t*-Pna is applied to label plasma membrane-enriched fractions of rat hippocampus, and, also, the first time that a long component typical of the gel phase (>30 ns) is found in plasma membrane of mammalian cells. The longer component, α4, rendered the following fluorescence lifetime values: 35.5±0.96 and 38.5 ± 1.70, for fed and fasted membranes, respectively (Figure 4.9B). This difference is not significant. This result is not quite surprising, for it is known the great contribution of sphingolipids for neuronal development, functioning, maintenance and survival (Sonnino & Prinetti, 2016; Olsen & Færgeman, 2017). Thus, the tendency of sphingolipids to coalesce in the PM into solid (gel)-like domains contributed to the detection of such long components. However, it is important to recall that these measurements were carried out at 23ºC, and thus it is possible that at 37ºC this long lifetime component is not detected. In addition, the strong preference of *t*-PnA for s_o domains (2 to 5-fold), which makes it a unique probe able to detect such kind of domains in complex biological membranes, also means that the value of α4 (roughly 15%-20%, Figure 4.9A) is a majorant of the actual fraction of such domains in the system under study.

Overall, these results report the natural lipid organization in the PM of rat hippocampus, which, apparently, do not suffer any modifications during the feeding cycle. The product $\alpha_i\tau_i$, depicted in Figure 4.9C, which weights the abundance of the components in the PM with the preference of the *t*-pna for more ordered domains, summarizes this general thought. Remarkably the proportions are evenly distributed among the fed and fasted membranes. Not surprisingly, the products $\alpha_3\tau_3$ and $\alpha_4\tau_4$ represent the larger proportions which confirms, on one hand, the large abundance of cholesterol-enriched l_o domains,

and, on the other hand, the preference of *t*-Pna for the most ordered domains (s_o) of the PM.

4.5.2 Biochemical characterization of the plasma membrane of rat hippocampus

4.5.2.1 Lipid content

The assessment of the lipid content of the plasma membrane of rat hippocampus was attained by applying a widely used lipid extraction method (Bligh & Dyer, 1959), with which I was able to extract the total lipids from the plasma membrane-enriched fractions of fed and fasted animals. Concentration of lipid phosphate was determined subsequent to total digestion by perchloric acid using Na_2HPO_4 as standard (Rouser *et al.*, 1970) and cholesterol concentration was estimated by direct treatment of the lipid extracts with a reagent composed of ferric chloride dissolved in a glacial acetic acid-sulfuric acid mixture (Zlatkis *et al.*, 1953). Subsequently, the phospholipid to cholesterol molar ratios and their relative abundance to protein concentration (previously calculated after the isolation of PM-enriched fractions) were obtained (Table 4.1).

Table 4.1- Estimation of cholesterol and phospholipid content of the PM of rat hippocampus. Values are mean ± SEM (n=4).

	Phospholipid/Protein (μmol/mg)	Cholesterol/Protein (μmol/mg)	Cholesterol/Phopholipid[a]
Fed	3.8 ± 1.07	1.4 ± 0.37	0.4 ± 0.10
Fasted	4.3 ± 1.05	2.1 ± 0.36	0.5 ±0.04

[a] Molar ratios

From the results presented in table 4.1, it is reasonable to conclude that feeding cycle did not exert any influence on the biochemical composition of the PM. All the ratios calculated did not disclose significant differences between fed and fasted conditions. This is consistent with the indication that the feeding cycle does not change the order and lateral heterogeneity (lipid domains segregation in the plane of bilayer phospholipid) of the PM of rat hippocampus, as illustrated by the anisotropy and fluorescence lifetime analyses. For example, the fact that cholesterol to phospholipid molar ratio did not show

any significant differences between fed and fasted animals is an insightful clue that the extent of the coalescence of lipids into lipid-raft domains might be the same in the PM of hippocampus from fed and fasted animals. In both metabolic conditions, the cholesterol content, normalized to the phospholipid concentration (cholesterol to phospholipid molar ratio), is roughly defined by 1mol of cholesterol to 2moles of phospholipid, which is in agreement with the proportion obtained in native membrane of bovine hippocampus (Pucadyil & Chattopadhyay, 2004; Mukherjee *et al.*, 2007; Saxena *et al.*, 2015) and with the estimation made above based on DPH fluorescence anisotropy.

The proteins are also a major component of the PM, as it is well-established that proteins possess the potential to organize membrane domains, and indeed protein– protein interactions have been regarded for several years as the main factor responsible for the stabilization of membrane domains (Prinetti *et al.*, 2009; Sonnino & Prinetti, 2010; Aktas *et al.*, 2014; Sezgin *et al.*, 2017). Nevertheless, the cooperation between protein- and lipid-driven lateral organizations is utterly important in the creation of membrane structural and functional heterogeneity, namely in the formation of specialized microdomains (commonly known as 'lipid rafts'), where specific membrane proteins are essentially located. That said, the results obtained for the content of cholesterol with respect to total protein (Table 4.1) are another suggestion that the distribution and abundance of lipid rafts encountered in the PM of rat hippocampus might be the same whether the animals have or not eaten. Furthermore, the phospholipid to protein ratio emphasizes the higher abundance of phospholipids in the PM (in relation to cholesterol and proteins) and the resistance of PM of rat hippocampus on modifying the molecular dynamics and mosaic organization during the feeding cycle.

4.5.2.2 Phospholipid composition of the PM of rat hippocampus

The phospholipid composition of the PM of rat hippocampus was also addressed by using Thin Layer Chromatography (TLC) technique. Total lipids extracted from hippocampal plasma membrane were separated with the following solvent system: chloroform–methanol–acetic acid–acetone–water, in the ratio 35:25:4:14:2 (Xu *et al.*, 1996). Phospholipids were detected by staining with Coomassie brilliant blue (Nakamura & Handa, 1984).

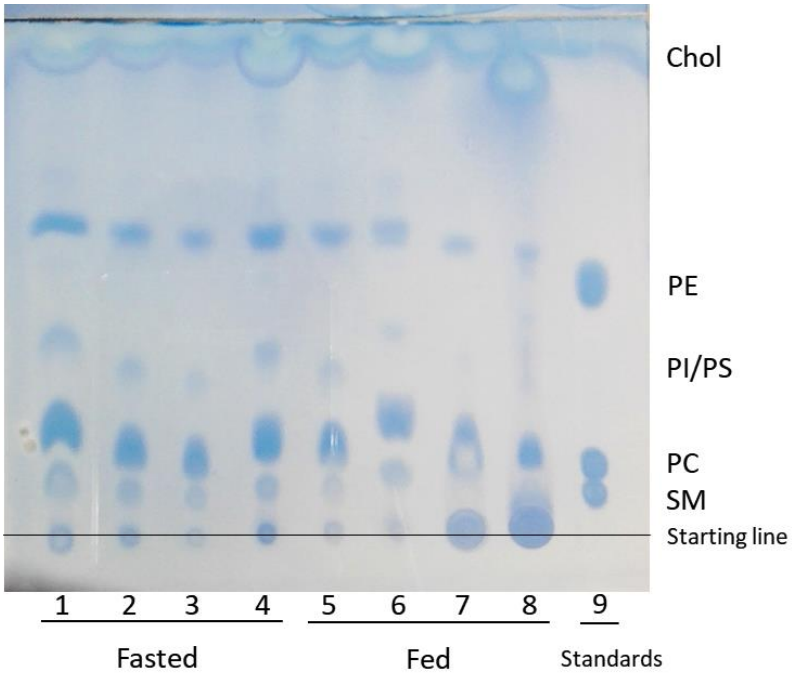

Figure 4.10- ***Separation of phospholipids constituents of the PM of rat hippocampus by one-dimensional thin layer chromatography.*** *The plate contains 8 lanes with samples from fasted (lanes 1-4) and fed (lanes 5-8) animals. 20µg of phospholipids were applied at the starting line spots. A mixture of standard phospholipids (10µg per phospholipid; SM, PC, PE and cholesterol) was applied in lane 9.*

The silica gel plate in figure 4.10 depicts the main phospholipids of the PM of rat hippocampus, being PC and PE the most predominant, followed by SM. This is in agreement with results obtained by other authors, from experiments performed with rat hippocampal membranes (Ulmann *et al.*, 2001; Murthy *et al.*, 2002). The stained spots between PE and PC might be related to the presence of PI and/or PS (Xu *et al.*, 1996). However, this identification remains elusive as I did not use any standards of these phospholipids. Regarding the cholesterol, either it was totally eluted, or the staining method was not adequate for sterol identification. The lanes 7 and 8 show smeared dots at the starting line which indicates that the application of these samples did not succeed. However, the overall qualitative comparison of the spots between fed and fasted lanes allows me to state that the feeding cycle did not have a major influence on the phospholipid composition of rat hippocampal membranes.

4.5.3 Conclusions on the influence of feeding cycle on the plasma membrane of rat hippocampus

The results disclosed by the fluorescence anisotropy of DPH indicate that fed and fasted animals have similar hippocampal global membrane order and, together with the anisotropy of *t*-Pna, suggests that the hippocampus of both is essentially constituted by l_o domains, functionally known as lipid-raft domains. These are characterized by a higher density of lipid-protein interactions, where the ion channels studied on this thesis are located (Tsui-Pierchala *et al.*, 2002; Lee, 2006; Dart, 2010; Jiang & Gonen, 2012). Furthermore, as indicated by the individual analysis of the components of fluorescence lifetime of *t*-Pna, the abundance of these lipid-raft domains is virtually the same during the feeding cycle. This might be thought as a safeguard mechanism of the neurones to the peripheral metabolic variations. Also, the relative contribution of the remaining lipid domains to the mean fluorescence lifetime of *t*-Pna is identical in fed and fasted animals.

The thesis that the feeding cycle has no influence on the dynamics of neuronal membranes is further supported by the fact that lipid content of the PM was kept unaltered whether the animals were or not fed. The phospholipid composition, as well as the ratios calculated between the phospholipid, cholesterol and protein concentrations did not change significantly between the samples extracted from the hippocampus of fed and fasted animals.

The experiments carried out cannot exclude that more subtle changes might be occurring. For example, a complete lipidomic profiling of the lipid extracts could reveal changes that could not be detected by TLC involving minor lipids involved in signaling, such as PIPs. Also, there are solvent extraction methods that might be more adequate for the full extraction of gangliosides, which could then be analyzed by TLC using solvent systems that can separate different ganglioside subtypes. On another hand, the use of other fluorophores with a preferential location at more surface regions of the membrane would relay other biophysical properties that were not assessed in this thesis, such as order and hydration of the PM at the membrane/water interface. Thus, despite that the amount and packing of lipid raft domains did not change, as indicated by the DPH and *t*-Pna results, it is not clear yet whether the feeding cycle influences or not the lipid-protein interactions, at least, at a surface level.

In summary, this chapter provides compelling evidence on the maintenance of the overall organization and dynamics of neuronal membranes during the feeding cycle.

4.6 References

Adibhatla RM & Hatcher JF (2008). Altered Lipid Metabolism in Brain Injury and Disorders. *Subcell Biochem* **49,** 241–268.

Aktas M, Danne L, MÃ¶ller P & Narberhaus F (2014). Membrane lipids in Agrobacterium tumefaciens: biosynthetic pathways and importance for pathogenesis. *Front Plant Sci* **5,** 1–13.

de Almeida RFM, Fedorov A & Prieto M (2003). Sphingomyelin/phosphatidylcholine/cholesterol phase diagram: Boundaries and composition of lipid rafts. *Biophys J* **85,** 2406–2416.

de Almeida RFM & Joly E (2014). Crystallization around solid-like nanosized docks can explain the specificity, diversity, and stability of membrane microdomains. *Front Plant Sci* **5,** 1–14.

de Almeida RFM, Loura LMS, Fedorov A & Prieto M (2005). Lipid rafts have different sizes depending on membrane composition: A time-resolved fluorescence resonance energy transfer study. *J Mol Biol* **346,** 1109–1120.

de Almeida RFM, Loura LMS & Prieto M (2009). Membrane lipid domains and rafts: current applications of fluorescence lifetime spectroscopy and imaging. *Chem Phys Lipids* **157,** 61–77.

Aresta-Branco F, Cordeiro AM, Marinho HS, Cyrne L, Antunes F & De Almeida RFM (2011). Gel domains in the plasma membrane of Saccharomyces cerevisiae: Highly ordered, ergosterol-free, and sphingolipid-enriched lipid rafts. *J Biol Chem* **286,** 5043–5054.

Bastos AEP, Scolari S, Stöckl M & De Almeida RFM (2012). Applications of fluorescence lifetime spectroscopy and imaging to lipid domains in vivo. *Methods Enzymol* **504,** 57–81.

Bligh EG & Dyer WJ (1959). A rapid method of total lipid extraction and purification. *Can J Biochem Physiol*.

Bloch K (1957). The Biological Synthesis of Cholesterol. *Vitam Horm* **15,** 119–150.

Brown AJ & Galea AM (2010). Cholesterol as an evolutionary response to living with

oxygen. *Evolution (N Y)* **64,** 2179–2183.

Castro BM, De Almeida RFM, Silva LC, Fedorov A & Prieto M (2007). Formation of ceramide/sphingomyelin gel domains in the presence of an unsaturated phospholipid: A quantitative multiprobe approach. *Biophys J* **93,** 1639–1650.

Castro BM, Silva LC, Fedorov A, de Almeida RFM & Prieto M (2009). Cholesterol-rich fluid membranes solubilize ceramide domains: Implications for the structure and dynamics of mammalian intracellular and plasma membranes. *J Biol Chem* **284,** 22978–22987.

Chavko M, Nemoto EM & Melick J a (1993). Regional lipid composition in the rat brain. *Mol Chem Neuropathol* **18,** 123–131.

Dart C (2010). Lipid microdomains and the regulation of ion channel function. *J Physiol* **588,** 3169–3178.

Elson EL, Genin GM, Fried E, Dolbow JE & Genin GM (2010). Phase separation in biological membranes: integration of theory and experiment. *Annu Rev Biophys* **39,** 207–226.

Escribá PV & Nicolson GL (2014). Membrane structure and function: Relevance of lipid and protein structures in cellular physiology, pathology and therapy. *Biochim Biophys Acta - Biomembr* **1838,** 1449–1450.

Ingólfsson HI, Carpenter TS, Bhatia H, Bremer PT, Marrink SJ & Lightstone FC (2017). Computational Lipidomics of the Neuronal Plasma Membrane. *Biophys J* **113,** 2271–2280.

Ingólfsson HI, Melo MN, Van Eerden FJ, Arnarez C, Lopez CA, Wassenaar TA, Periole X, De Vries AH, Tieleman DP & Marrink SJ (2014). Lipid organization of the plasma membrane. *J Am Chem Soc* **136,** 14554–14559.

Jiang Q-X & Gonen T (2012). The influence of lipids on voltage-gated ion channels. *Curr Opin Struct Biol* **22,** 529–536.

Lakowicz JR (2006). *Principles of Fluorescence Spectroscopy*, Third. Springer.

Laptenok SP (2009). *Global analysis of time-resolved fluorescence microspectroscopy and applications in biomolecular studies* (thesis).

Lee AG (2006). Ion channels: A paddle in oil. *Nature* **444,** 697.

Lentz BR & Burgess SW (1989). A dimerization model for the concentration dependent photophysical properties of diphenylhexatriene and its phospholipid derivatives. DPHpPC and DPHpPA. *Biophys J* **56,** 723–733.

Lingwood D, Kaiser H-J, Levental I & Simons K (2009). Lipid rafts as functional heterogeneity in cell membranes. *Biochem Soc Trans* **37,** 955–960.

Lingwood D & Simons K (2010). Lipid rafts as a membrane-organizing principle. *Science (80-)* **327,** 46–50.

Marquês JT, Antunes CAC, Santos FC & de Almeida RFM (2015). Biomembrane Organization and Function: The Decisive Role of Ordered Lipid Domains. *Adv Planar Lipid Bilayers Liposomes* **22,** 65–96.

Mattson MP (2005). Dietary Modulation of Lipid Rafts. Implications for Disease Prevention and Treatment. In *Membrane Microdomain Signaling. Lipid Rafts in Biology and Medicine*, ed. Mattson MP, pp. 191–201. Humana Press.

Mukherjee S, Kombrabail M, Krishnamoorthy G & Chattopadhyay A (2007). Dynamics and heterogeneity of bovine hippocampal membranes: Role of cholesterol and proteins. *Biochim Biophys Acta - Biomembr* **1768,** 2130–2144.

Murthy M, Hamilton J, Greiner RS, Moriguchi T, Salem N, Kim H & Differential HK (2002). Differential effects of n-3 fatty acid deficiency on phospholipid molecular species composition in the rat hippocampus. *J Lipid Res* **43,** 611–617.

Nakamura K & Handa S (1984). Coomassie brilliant blue staining of lipids on thin-layer plates. *Anal Biochem* **142,** 406–410.

O'Connor D V. & Phillips D (David) (1984). *Time-correlated single photon counting*. Academic Press.

Olsen ASB & Færgeman NJ (2017). Sphingolipids : Membrane microdomains in brain development, function and neurological diseases. *Open Biol* **7,** 170069.

Pike LJ (2009). The challenge of lipid rafts. *J Lipid Res* **50,** S323–S328.

Poveda JA, Giudici AM, Renart ML, Molina ML, Montoya E & Encinar JA (2014). Lipid modulation of ion channels through specific binding sites. *BBA - Biomembr* **1838,**

1560–1567.

Pucadyil TJ & Chattopadhyay A (2004). Exploring detergent insolubility in bovine hippocampal membranes: A critical assessment of the requirement for cholesterol. *Biochim Biophys Acta - Biomembr* **1661,** 9–17.

Quinn PJ & Wolf C (2010). An X-ray diffraction study of model membrane raft structures. *FEBS J* **277,** 4685–4698.

Reyes Mateo C, Brochon JC, Pilar Lillo M & Ulises Acuña A (1993*a*). Lipid clustering in bilayers detected by the fluorescence kinetics and anisotropy of trans-parinaric acid. *Biophys J* **65,** 2237–2247.

Reyes Mateo C, Tauc P & Brochon JC (1993*b*). Pressure effects on the physical properties of lipid bilayers detected by trans-parinaric acid fluorescence decay. *Biophys J* **65,** 2248–2260.

Rouser G, Fkeischer S & Yamamoto A (1970). Two dimensional then layer chromatographic separation of polar lipids and determination of phospholipids by phosphorus analysis of spots. *Lipids* **5,** 494–496.

Saxena R, Shrivastava S & Chattopadhyay A (2015). Cholesterol-induced changes in hippocampal membranes utilizing a phase-sensitive fluorescence probe. *Biochim Biophys Acta - Biomembr* **1848,** 1699–1705.

Schaeffer EL, Skaf HD, Novaes B de A, da Silva ER, Martins BA, Joaquim HDG & Gattaz WF (2011). Inhibition of phospholipase A 2 in rat brain modifies different membrane fluidity parameters in opposite ways. *Prog Neuro-Psychopharmacology Biol Psychiatry* **35,** 1612–1617.

Schroeder F, Goetz IE & Roberts E (1984). Membrane Anomalies in Huntington's Disease Fibroblasts. *J Neurochem*526–539.

Schroeder F, Gorka C, Williamson LS & Wood WG (1987). The influence of dolichols on fluidity of mouse synaptic plasma membranes. *BBA - Biomembr* **902,** 385–393.

Sebastião AM, Colino-Oliveira M, Assaife-Lopes N, Dias RB & Ribeiro JA (2013). Lipid rafts, synaptic transmission and plasticity: Impact in age-related neurodegenerative diseases. *Neuropharmacology* **64,** 97–107.

Sezgin E, Levental I, Mayor S & Eggeling C (2017). The mystery of membrane organization: Composition, regulation and roles of lipid rafts. *Nat Rev Mol Cell Biol* **18,** 361–374.

Simons K & Sampaio JL (2011). Membrane Organization and Lipid Rafts. *Cold Spring Harb Perspect Biol*1–18.

Sklar LA, Hudson BS, Petersen M & Diamond J (1977). Conjugated Polyene Fatty Acids on Fluorescent Probes: Spectroscopic Characterization. *Biochemistry* **16,** 813–819.

Sonnino S & Prinetti A (2010). Lipids and Membrane Lateral Organization. *Front Physiol* **1,** 1–9.

Sonnino S & Prinetti A (2016). The role of sphingolipids in neuronal plasticity of the brain. *J Neurochem* **137,** 485–488.

Sun GY, Huang HM, Kelleher JA, Stubbs EB & Sun AY (1988). Marker enzymes, phospholipids and acyl group composition of a somal plasma membrane fraction isolated from rat cerebral cortex: a comparison with microsomes and synaptic plasma membranes. *Neurochem Int* **12,** 69–77.

Tsui-Pierchala BA, Encinas M, Milbrandt J & Johnson EM (2002). Lipid rafts in neuronal signaling and function. *Trends Neurosci* **25,** 412–417.

Ulmann L, Mimouni V, Roux S, Porsolt R & Poisson JP (2001). Brain and hippocampus fatty acid composition in phospholipid classes of aged-relative cognitive deficit rats. *Prostaglandins Leukot Essent Fatty Acids* **64,** 189–195.

Valeur B & Berberan-Santos MN (2012). *Molecular Fluorescence: Principles and Applications*, Second. Wiley-VCH Verlag GmbH & Co. KGaA.

Van Meer G (2005). Cellular lipidomics. *EMBO J* **24,** 3159–3165.

Van Meer G & de Kroon AIPM (2011). Lipid map of the mammalian cell. *J Cell Sci* **124,** 5–8.

Van Meer G, Voelker DR & Feigenson GW (2008). Membrane lipids: Where they are and how they behave. *Nat Rev Mol Cell Biol* **9,** 112–124.

Wen Z & Kim HY (2004). Alterations in hippocampal phospholipid profile by prenatal exposure to ethanol. *J Neurochem* **89,** 1368–1377.

Xu G, Waki H, Kon K & Ando S (1996). Thin-Layer Chromatography of Phospholipids and Their Lyso Forms: Application to Determination of Extracts from Rat Hippocampal CA1 Region. *Microchem J* **53,** 29–33.

Zlatkis A, Zak B & Boyle AJ (1953). A new method for the direct determination of serum cholesterol. *J Lab Clin Med* **41,** 486–492.

5 Final considerations

5.1 General discussion

The function of hippocampus as a hub for energy balance is a subject of broad and current interest. This thesis further exploits this point by giving insights into the mechanisms underlying the adaptation of intrinsic neuronal membrane properties to variations of physiological metabolism, brought up by the feeding cycle.

A previous work performed on rat hippocampal CA1 neurones had suggested a marked impact of feeding cycle on the neuronal excitability (Lima *et al.*, 2012). Here, I have drawn a set of experiments to further investigate such effect and, accordingly, outline possible underlying mechanisms. Specifically, I have addressed the hypothesis of the involvement of voltage gated ion channels into the influence of feeding cycle upon neuronal activity.

The biophysical behaviour of voltage gated Na^+ and Ca^{2+} currents was analysed, given their importance in the initiation and propagation of action potentials (I_{Na}), and influence on the influx of the most widely known second messenger, Ca^{2+}, into the neurones (I_{Ca}).

The electrophysiology findings were obtained in isolated neurones. The enzymatic and mechanical digestion steps used in this methodological approach might confer an unpredictable outcome with respect to structure and shape of the neurones. In order to duly circumvent this technical idiosyncrasy, I have used neurones with identical shape and appearance (for more details, see section 3.1.4). Such procedure diminished the variability of the initial conditions. The efficacy of this visual selection was confirmed by the similarity of the mean membrane capacitance (pF) values observed between all fed (9.3 ± 0.31pF; n=72) and fasted (8.8 ± 0.4pF; n=81) neurones used in this thesis. Hence, as the feeding cycle did not influence the membrane capacitance of neurones, the physiological differences here outlined are attributed to the actual ion channels` biophysical properties. For example, the conspicuous effect of feeding cycle upon the Na^+ current density (pA/pF) reflects a real increase of the current amplitude (pA, not normalised; data not shown).

The larger Na^+ channel density and higher single-Na^+ channel conductance assigned to fed neurones are the foundations of the significant differences observed in the whole-cell

Na^+ current output. Specifically, increased current density (~1.5 fold) and larger window current (meaning more channels available to respond to activation), upon feeding, confirm that the feeding cycle alters inward flux of Na^+ ions, which, in turn, influence neuronal excitability. Furthermore, the overall change in the number of channel population due to the feeding cycle can be virtually quantified. Dividing the mean maximum conductance of whole-cell recordings by the mean unitary conductance calculated in single-channel recordings, one yields an estimate of the number of functional channels (Ogden, 1994; Sakmann & Neher, 1995; Ashcroft, 2000; Hille, 2001) present at the surface of the neurones. Following this rationale, we have obtained 1.61×10^9 and 1.38×10^9 sodium channels per cm^2 of the soma of CA1 pyramidal cells, in fed and fasted conditions, respectively.

On the other hand, the effect of feeding cycle upon the whole-cell Ca^{2+} currents was not so evident, probably because the fact that intracellular calcium concentration ($[Ca^{2+}_i]$) must be tightly regulated. Any small alteration in $[Ca^{2+}_i]$ results in a substantial neuronal physiological output given that numerous intracellular biochemical processes are modulated by Ca^{2+}. Amongst them, the processes that reinforce the synaptic performance have to be highlighted. The influence of Ca^{2+} ions upon such phenomena is well-established. Ca^{2+} modulates several preparatory steps of the synaptic processes, mainly the release of neurotransmitters into the synaptic cleft. Thus, one may state that the predominance of voltage gated Ca^{2+} channels that contribute to a major Ca^{2+} entry into the neurones will induce a major Ca^{2+}-dependent neuronal response. In this study I have showed that fed neurones do gather greater conditions to a boost of Ca^{2+} influence on neuronal activity, when compared to fasted neurones.

In conclusion, the results obtained from both currents – I_{Na} and I_{Ca} - point out to an augmented synaptic performance, after feeding, given the putative increased neuronal excitability levels, brought up by I_{Na}, and the probable potentiation of intracellular Ca^{2+}-dependent signal transduction, with respect to I_{Ca}. Together, these two observations may render optimal conditions for supporting synaptic plasticity phenomena in fed neurones. In this way one could establish a bridge between the two roles of hippocampus, either as a substrate for learning and memory and as a centre of energy homeostasis. Specifically, the results presented here endorse the role of hippocampus on regulating the start of a new meal, by the formation of meal episodic-related memories (Higgs, 2002, 2008; Henderson *et al.*, 2013; Parent, 2016*a*, 2016*b*; Hannapel *et al.*, 2017)

The observed influence of feeding cycle on the biophysical and molecular expression of voltage-gated Na^+ and Ca^{2+} channels did not have repercussions on the lipid environment of the plasma membrane. The results presented in this thesis indicate that the organization and lipid content of the plasma membrane of rat hippocampus did not endure any notorious variation during the feeding cycle. Such observation is consistent with the resemblance of the mean membrane capacitance values between fed and fasted neurones (see above). The absence of meal driven alterations on the lipid membrane environment may be regarded as a homeostatic mechanism of central nervous system neurones to preserve their biological functions regardless the peripheral metabolic state. Thus, despite the variations in the biophysical and molecular behaviour of voltage-gated Na^+ and Ca^{2+} channels imbedded in the plasma membrane, the overall organization and dynamics of neuronal membranes must be kept under strict parameters, denotating that it is tightly regulated, in order to maintain the structure and function of the neurones. In other words, neurones must have a shield mechanism to preserve their functional viability, either when the animals are fed or maintained in fasting conditions for a period of, at least, 20 hours, which corresponds to the maximum fasting time spanned in this study. The suggestion that the relative contribution of lipid-raft domains did not undergo any alteration during the feeding cycle is a highly relevant indicator of this protecting mechanism, as these domains segregate all the molecules responsible for the signaling to the interior of the cells.

Furthermore, the variation observed in the τ_{hslow} of I_{Na} is not linked to alterations in the lateral heterogeneity of the plasma membrane, as suggested in the discussion section of the voltage-gated Na^+ currents chapter. However, it must be noted that the interactions between the channels and the lipids in the vicinity of the channels were not exploited. The differences obtained in the τ_{hslow} may stem from the greater channel density, since more channels may take, on average, more time to complete the inactivation process.

Further translational perspective – implications of diet on excitability, seizure controlling and experimental design considerations

Most of the discussion throughout the thesis was held by the effect of the post prandial period upon the neuronal activity. However, this work can be viewed from a whole distinct perspective, by considering the benefits of fasting. This is a subject which is

undergoing intense study due to its impact on epidemic diseases like obesity, and subsequent consequences on neurological diseases.

Several clinical studies point to a clear influence of diet in neurological disorders, such as epilepsy and Alzheimer´s disease. For instance, fasting protocols (Intermittent fasting diet, caloric restriction diet) or diet protocols that pretend to mimic fasting metabolic states (ketogenic diet) are thought to develop beneficial effects on mitigating the frequency of epilepsy seizures (Cunnane *et al.*, 2002; Likhodii *et al.*, 2003; Papandreou *et al.*, 2006; Bough & Rho, 2007; Hartman & Vining, 2007; Rho, 2017). Such observation may be related with a constant production of ketone bodies induced by fasting (Cunnane *et al.*, 2002; Likhodii *et al.*, 2003; Mattson, 2008; McNally & Hartman, 2012; Lima *et al.*, 2014). However, the molecular mechanisms that overrule such effects are not well understood. Here, the voltage-gated Na^+ channels, widely known to play a central role in the genesis and alleviation of epilepsy (Goldin, 1999; Denac *et al.*, 2000; Eijkelkamp *et al.*, 2012; Mantegazza & Catterall, 2012; Kaplan *et al.*, 2016; Deuis *et al.*, 2017), are regarded to mediate the impact of diet and metabolism in epilepsy. Changes in the biophysics of the Na^+ channels may contribute to seizure susceptibility as they are exquisitely sensitive sites for determining neuronal excitability. Thus, increased inhibition or decreased excitability, as observed in fasted neurones, if sufficiently intense, may influence the normal functioning of the brain in addition to controlling seizures. In contrast, in fed conditions, increased sodium current amplitude, associated with depolarizing shift in the voltage dependence of inactivation and hyperpolarizing shift in the voltage dependence of activation, may result in an increase of AP firing frequency which, eventually, may fallout in an epileptic activity. In conclusion, the results showed for fasting condition may have a relationship with the present notion in which a fasting diet slows down the activity of neurones, preventing the outburst of epilepsy seizures (Likhodii *et al.*, 2003; Bough & Rho, 2007; Fond *et al.*, 2013; Longo & Mattson, 2014; Rho, 2017). Indeed, a previous report on whole-cell Na^+ currents of hippocampal CA1 neurones of chronic epileptic rats showed electrophysiology characteristics reminiscent of those reported here for fed neurones (Ketelaars *et al.*, 2001). Additionally, it is noteworthy to mention that the Na^+ channels highlighted in this report - $Na_v1.1$ and $Na_v1.2$ - have been implied in epilepsy seizure activity (Eijkelkamp *et al.*, 2012; Mantegazza & Catterall, 2012; Kaplan *et al.*, 2016; Deuis *et al.*, 2017).

These results constitute a major contribution to ameliorate the understanding of the molecular mechanisms by which fasting affects central nervous system neurones. The promotion of Na^+ channels as molecular determinants in the impact of feeding cycle on brain function is of the utmost importance because they can help to explain the underpinning molecular mechanisms of several epidemiologic studies that relate fasting with seizure control.

This thesis also infers a very practical implication on how neuroscientists should look at rat preparations as experimental models. The results outlined here raise the levels of awareness and control one should have on what the feeding-state of each experimental design may concern. The present report shows that variations in electrophysiological recordings may solely due, after all, to the fact that a given animal have eaten or not. Thus, the feeding cycle must be a condition tightly controlled in all electrophysiology experimental designs.

5.2 Future perspectives

The findings presently reported might be also translated into the influence of peripheral physiological metabolism upon cognitive processes, since hippocampus is considered central in operations related with memory and learning. It is plausible to envisage different firing patterns in hippocampus slices from fed and fasted rats, which in the long run may affect consolidation of cognitive processes such as learning and memory. Scaling out these findings into a more physiological context will enable a more robust interpretation. Thus, whole-cell current clamp recordings in hippocampal CA1 neurones within brain slices obtained from fed and fasted rats will help us to confirm and understand better the higher levels of neuronal excitability This would be done by studying the action potential shape, firing patterns and induction thresholds. Finally, synaptic current measurements in hippocampal slices will also be highly valuable to understand further if there is a potentiation of synaptic function through over feeding and, accordingly, provide functional implications of physiological metabolism.

Furthermore, to support the interpretation of the results here presented and to answer questions raised by this work, the following experiments/studies are proposed:

- Immunostaining studies (western blotting and/or immunocytochemistry) will be applied to assess the expression of other Na_v isoforms, namely $Na_v1.1$, in fed and fasted neurones.
- Voltage activated Ca^{2+} currents will be recorded from the isolated neurones using different selective blockers to confirm the nature of the currents involved in the tidal variation brought up by the feeding cycle.
- Measurements of cytosolic Ca^{2+} concentration can be used to confirm the larger entry of Ca^{2+} into the fed neurones. This can be done on single neurones by using ester-loaded with the fluorescent indicator Fura2 and ratiometric measurements.
- Study the lipid organization at the vicinity of the Na^+ channels, in order to confirm if the plasma membrane exerts any effect on the conformational rearrangements of the outer pore of the Na^+ channels. For such, it is important to apply fluorescence spectroscopy studies on fluorophores that bind to the extracellular pore of the channels, such as fluorescent and photoactivatable fluorescent derivatives of tetrodotoxin (TTX, Angelides, 1981) or fluorescently labelled derivatives of saxitoxin (STX, Ondrus *et al.*, 2012).

5.3 References

Angelides KJ (1981). Fluorescent and Photoactivatable Fluorescent Derivatives of Tetrodotoxin To Probe the Sodium Channel of Excitable Membranes. *Biochemistry* **20,** 4107–4118.

Ashcroft FM (2000). *Ion Channels and Disease*. Academic Press, Oxford, United Kingdom.

Bough KJ & Rho JM (2007). Anticonvulsant mechanisms of the ketogenic diet. *Epilepsia* **48,** 43–58.

Cunnane SC, Musa K, Ryan M a, Whiting S & Fraser DD (2002). Potential role of polyunsaturates in seizure protection achieved with the ketogenic diet. *Prostaglandins Leukot Essent Fatty Acids* **67,** 131–135.

Denac H, Mevissen M & Scholtysik G (2000). Structure, function and pharmacology of voltage-gated sodium channels. *Naunyn Schmiedebergs Arch Pharmacol* **362,** 453–479.

Deuis JR, Mueller A, Israel MR & Vetter I (2017). Neuropharmacology The pharmacology of voltage-gated sodium channel activators. *Neuropharmacology*; DOI: 10.1016/j.neuropharm.2017.04.014.

Eijkelkamp N, Linley JE, Baker MD, Minett MS, Cregg R, Werdehausen R, Rugiero F & Wood JN (2012). Neurological perspectives on voltage-gated sodium channels. *Brain* **135,** 2585–2612.

Fond G, Macgregor A, Leboyer M & Michalsen A (2013). Fasting in mood disorders: Neurobiology and effectiveness. A review of the literature. *Psychiatry Res* **209,** 253–258.

Goldin AL (1999). Diversity of mammalian voltage-gated sodium channels. *Ann N Y Acad Sci* **868,** 38–50.

Hannapel RC, Henderson YH, Nalloor R, Vazdarjanova A & Parent MB (2017). Ventral hippocampal neurones inhibit postprandial energy intake. *Hippocampus* **27,** 274–284.

Hartman AL & Vining EPG (2007). Clinical Aspects of the Ketogenic Diet. *Epilepsia* **48,**

31–42.

Henderson YO, Smith GP & Parent MB (2013). Hippocampal neurones inhibit meal onset. *Hippocampus* **23,** 100–107.

Higgs S (2002). Memory for recent eating and its influence on subsequent food intake. *Appetite* **39,** 159–166.

Higgs S (2008). Cognitive influences on food intake: The effects of manipulating memory for recent eating. *Physiol Behav* **94,** 734–739.

Hille B (2001). *Ion Channels of Excitable Membranes*, Third. Sinauer Associates, Inc.

Kaplan DI, Isom LL & Petrou S (2016). Role of Sodium Channels in Epilepsy. *Cold Spring Harb Perspect Med* **6,** a022814.

Ketelaars SOM, Gorter JA, Van Vliet EA, Lopes da Silva FH & Wadman WJ (2001). Sodium currents in isolated rat CA1 pyramidal and dentate granule neurones in the post-status epilepticus model of epilepsy. *Neuroscience* **105,** 109–120.

Likhodii SS, Serbanescu I, Cortez MA, Murphy P, Snead OC & Burnham WM (2003). Anticonvulsant properties of acetone, a brain ketone elevated by the ketogenic diet. *Ann Neurol* **54,** 219–226.

Lima PA, Costa PC, Mondragão M, Alves FM, Costa G, Hardy D, Jalil A, Ogden D & Auger. C (2012). Metabolic states induced by feeding/fasting influence insulin-induced excitability and levels of insulin receptor in hippocampal but not cerebellar neurones. In *8 th FENS Forum of Neuroscience*.

Lima P, Sampaio L & Damasceno N (2014). Neurobiochemical mechanisms of a ketogenic diet in refractory epilepsy. *Clinics* **69,** 699–705.

Longo VD & Mattson MP (2014). Fasting: Molecular Mechanisms and Clinical Applications. *Cell Metab* **19,** 181–192.

Mantegazza M & Catterall WA (2012). Voltage-gated Na channels. In *Jasper´s Basic Mechanisms of the Epilepsies*, 4th edn., pp. 67–96.

Mattson MP (2008). Dietary factors, hormesis and health. *Ageing Res Rev* **7,** 43–48.

McNally MA & Hartman AL (2012). Ketone Bodies in Epilepsy. *J Neurochem* **121,** 28–35.

Ogden D ed. (1994). *Microelectrode techniques: the Plymouth Workshop handbook*, 2nd edn. The Company of Biologists.

Ondrus AE, Lee HD, Iwanaga S, Parsons WH, Andresen BM, Moerner WE & Bois J Du (2012). Fluorescent Saxitoxins for Live Cell Imaging of Single Voltage- Gated Sodium Ion Channels beyond the Optical Diffraction Limit. *J Chem Biol* **19,** 902–912.

Papandreou D, Pavlou E, Kalimeri E & Mavromichalis I (2006). The ketogenic diet in children with epilepsy. *Br J Nutr* **95,** 5.

Parent MB (2016*a*). Dorsal Hippocampal–Dependent Episodic Memory Inhibits Eating. *Curr Dir Psychol Sci* **25,** 461–466.

Parent MB (2016*b*). Cognitive control of meal onset and meal size: Role of dorsal hippocampal-dependent episodic memory. *Physiol Behav* **162,** 112–119.

Rho JM (2017). How does the ketogenic diet induce anti-seizure effects? *Neurosci Lett* **637,** 4–10.

Sakmann B & Neher E eds. (1995). *Single-channel recording*, Second. Plenum Press, New York.

6 ANNEX I

6.1 Hippocampus – historical perspective of anatomy and circuitry

There are several reasons the hippocampus has attracted the interest of scientists (…) The hippocampus has something for everyone (Andersen et al., 2007)

Hippocampus is a complex brain structure embedded deep into the temporal lobe. The hippocampus received its name from the Italian anatomist Julius Caesar Arantius in the late 16th century (1587), who considered the three-dimensional form of the human hippocampus to be reminiscent of the seahorse. The Latin word *hippocampus* was then coined from the Greek word *hippokampos* (hippos meaning "horse" and kampos meaning "sea monster"). Its terminology has suffered continuous alterations, which resulted in a certain vagueness regarding the terminology and anatomical description of the hippocampus (Walther, 2002). Currently, it is accepted that the term hippocampus is applied for the region of the hippocampal formation that comprises the CA (*cornu ammonis*, latin for 'horn of the ram') fields (CA3, CA2, CA1), identified by the neuroanatomist Rafael Lorente de Nó (Lorente de Nó, 1934). In contrast, the term hippocampal formation is applied to a cytoarchitectonic group of distinct contiguous regions including the dentate gyrus, hippocampus, subiculum, presubiculum, parasubiculum, and entorhinal cortex. These six regions are linked, one to the next, by unique and largely unidirectional (functional) neuronal pathways.

Ramon y Cajal`s monumental effort (Ramón y Cajal, 1893), including an analysis of all portions of the hippocampal formation in several animal species, allowed him to propose a first functional circuit diagram of this region. Following his two fundamental laws – Neuron Doctrine and Dynamic Polarization - he placed arrows indicating his view of the direction of impulse flow through the hippocampal formation (Figure 6.1). Briefly, the former principle states that the nerve cell (neuron) is the structural and functional unit of nervous system circuitry, and nerve cells interact with other nerve cells by way of contact or contiguity, contrasting with the idea of direct continuity between nerve cells as stated by the Reticular Theory, held by a contemporary scientist, Camilo Golgi (1886). The second law states that information flows through a nerve cell, and thus through neural circuits, in one direction - input to the dendrites, output through the axon -, which, once

again, contradicts Golgi´s concept regarding dendrites function as being the roots of the nerve cells (Newman *et al.*, 2017).

All the studies undertaken by Ramón y Cajal came, ironically, from preparations made with Golgi's method. They ended up sharing the Nobel Prize for Physiology or Medicine in 1906; Golgi had provided the method and Cajal had given us new and penetrating insights into the structure of the brain and spinal cord.

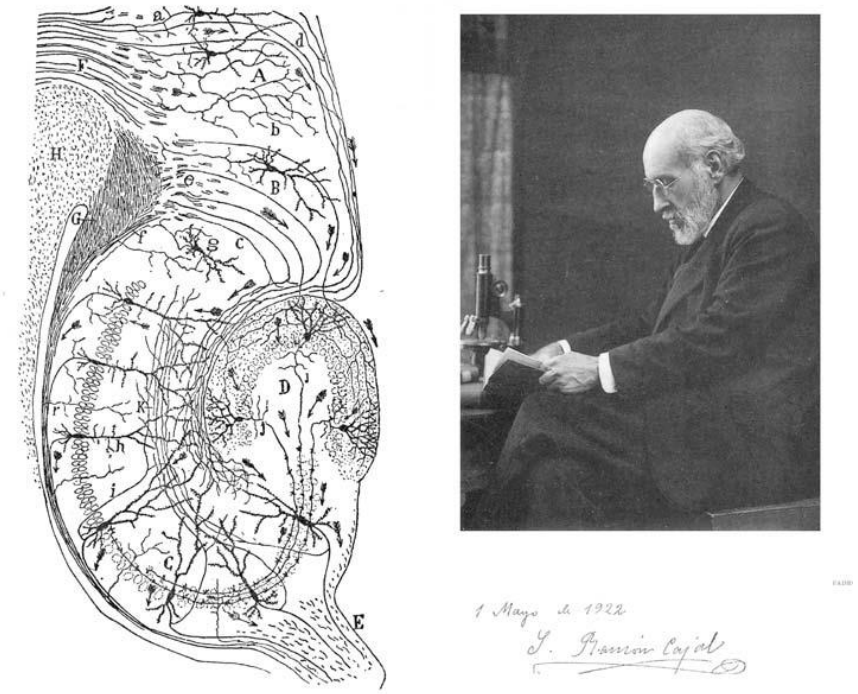

Figure 6.1- ***Santiago Ramon y Cajal and his famous drawing of the hippocampus in his 1911 book Histologie de Système Nerveux****. The arrows give his interpretation of likely impulse direction. Taken from Andersen et al., 2007*

6.1.1 Intrinsic hippocampal circuit

The flow of signals between hippocampal neurones is unidirectional, since the output of a given structure of the hippocampal formation does not flow back to the previous structure from which it received an input. That said, much of the neocortical input reaching the hippocampal formation does so through the entorhinal cortex, which can, for convenience, be considered the first step in the intrinsic hippocampal circuit (Figure 6.2).

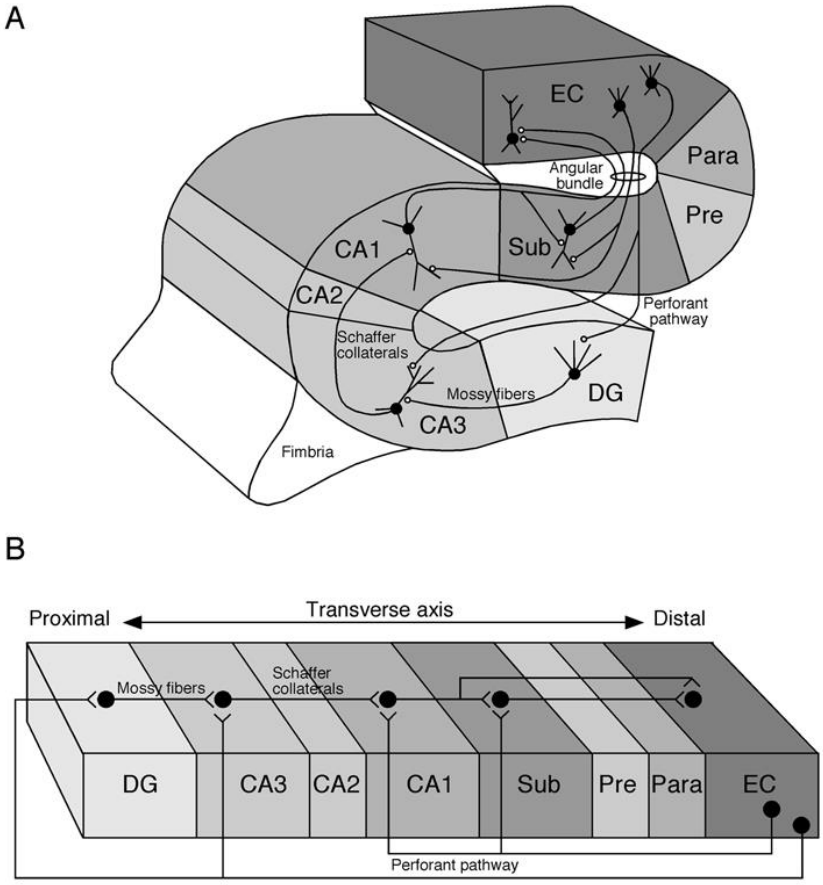

Figure 6.2- ***Lamellar or transversal circuitry of the hippocampal formation.*** *A) Neurones in layer II of the entorhinal cortex (EC) project to the dentate gyrus (DG) and the CA3 field of the hippocampus proper via the perforant pathway. Neurones in layer III of the entorhinal cortex project to the CA1 field of the hippocampus and the subiculum via the perforant and alvear pathways. The granule cells of the dentate gyrus project to the CA3 field of the hippocampus via mossy fiber projections. Pyramidal neurones in the CA3 field of the hippocampus project to CA1 via Schaffer collaterals. Pyramidal cells in CA1 project to the subiculum. Both CA1 and the subiculum project back to the deep layers of the entorhinal cortex. B. Projections along the transverse axis of the hippocampal formation; the dentate gyrus is located proximally and the entorhinal cortex distally. Taken from (Andersen et al., 2007)*

Cells in the superficial layers of the entorhinal cortex give rise to axons that project, among other destinations, to the dentate gyrus. The projections from the entorhinal cortex to the dentate gyrus form part of the major hippocampal input pathway called the *perforant path*. Although the entorhinal cortex provides the major input to the dentate gyrus, the dentate gyrus does not project back to the entorhinal cortex. Likewise, the principal cells of the dentate gyrus, the granule cells, give rise to axons called *mossy fibers* that connect with pyramidal cells of the CA3 field of the hippocampus. The CA3 cells, however, do not project back to the granule cells. The pyramidal cells of CA3, in turn, are the source of the major input to the CA1 hippocampal field (the Schaffer collateral axons). Following the pattern of its predecessors, CA1 does not project back to CA3. The CA1 field of the hippocampus then projects unidirectionally to the subiculum and to the

entorhinal cortex, closing the hippocampal processing loop that begins in the superficial layers of the entorhinal cortex and ends in its deep layers.

6.2 Rat hippocampal CA1 neurones

The rat hippocampal formation is an elongated, banana-shaped structure. The long axis of the hippocampal formation is referred to as the septotemporal (or dorsal-ventral) axis and the orthogonal axis as the transverse axis (Figure 6.3).

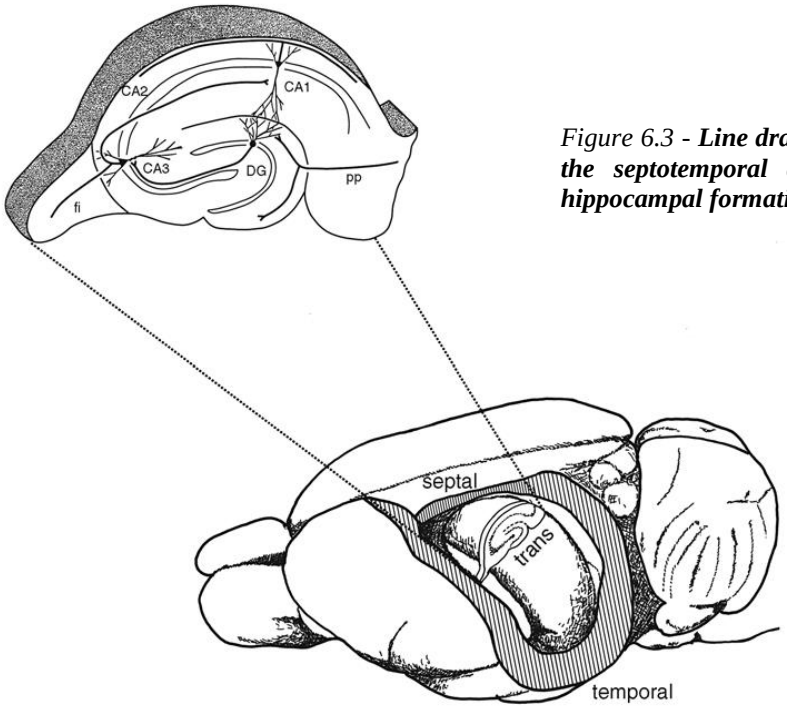

Figure 6.3 - ***Line drawing of the rat brain showing the septotemporal and transverse axes of the hippocampal formation***

The transversal axis unveils the laminar/layer organization of the hippocampus, which is generally similar for all the fields of the hippocampus. The principal cellular layer is called the pyramidal cell layer, which is tightly packed in CA1 (Figure 6.4). The narrow, relatively cell-free layer located deep to the pyramidal cell layer is called the stratum oriens. This layer contains the basal dendrites of the pyramidal cells and several classes of interneurones. The stratum radiatum is located immediately above the pyramidal cell layer in CA2 and CA1. The most superficial layer of the hippocampus is called the stratum lacunosum-moleculare.

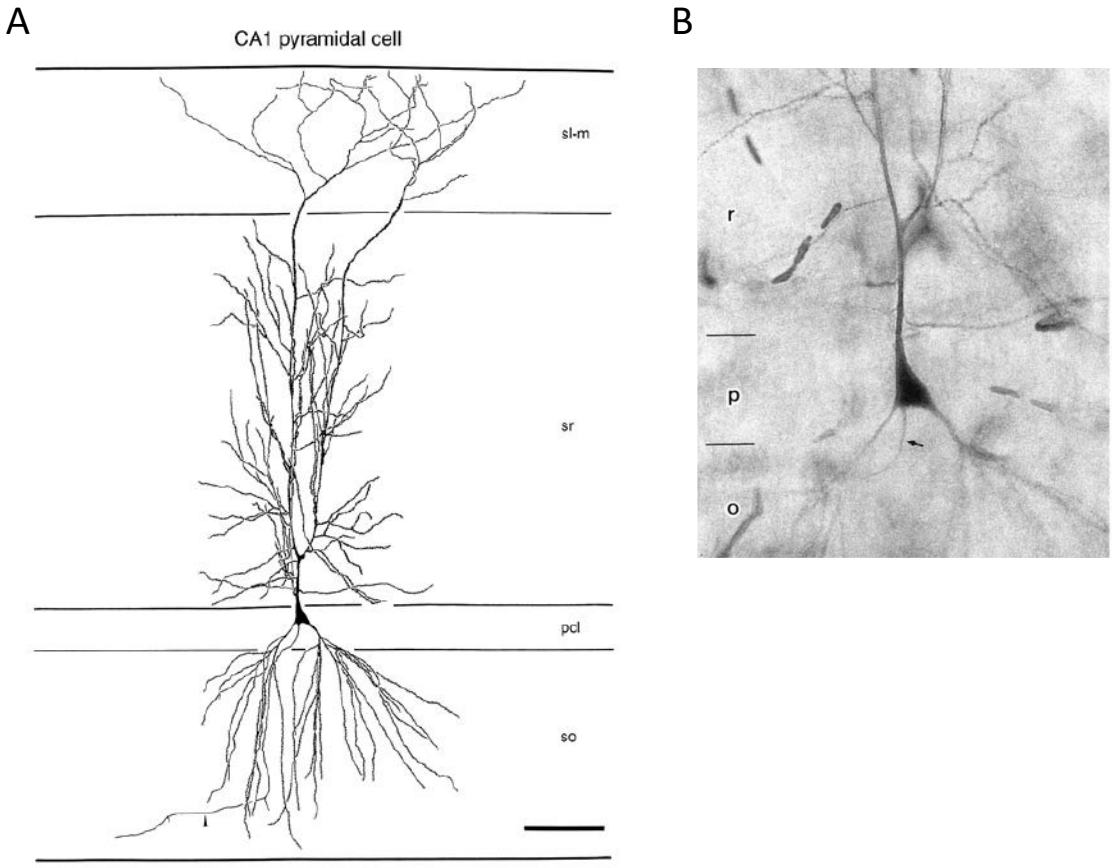

Figure 6.4- ***Anatomy of rat hippocampal CA1 neuron****. A) Camera lucida drawing of a CA1 pyramidal neuron from the midportion of the field. Note that side branches originate from the primary dendrites throughout the full extent of the stratum radiatum. Note also the curved and irregular trajectories of dendritic branches in the stratum lacunosum-moleculare. The axon of this neuron is indicated by an arrowhead. pcl, pyramidal cell layer; sl-m, stratum lacunosum-moleculare; so, stratum oriens; sr, stratum radiatum. Bar 100 µm. B) Photomicrographs of intracellularly labeled pyramidal cells in CA1 from rat hippocampus. Small arrows indicate the initial portion of the axon. Adapted from* (Ishizuka *et al.*, 1995)*.*

CA1 pyramidal cells show remarkable homogeneity of their dendritic trees. As well as being more homogeneous, they are also, on average, smaller than CA3 cells. The total dendritic length averages approximately 13.5 mm, and the average size of CA1 cell somata is about 193 μm^2 or 15 µm in diameter (Bannister & Larkman, 1995*a*, 1995*b*; Ishizuka *et al.*, 1995).

The CA1 pyramidal neuron is arguably the most studied class of neuron in the brain, and probably better understood from both structural and functional points of view than any other type of neuron in the hippocampus. There are enough reasons that justify why most of the studies have focused on the CA1 region: a) Relative ease of obtaining field potential recordings and intracellular recordings in this region; b) Schaffer collateral axons from CA3 form a homogeneous pathway that is easily activated to study synaptic transmission and plasticity; c) Studies of CA1 are more numerous than adjacent CA3 because it is

generally easier to keep cells in this region alive and healthy in slice and acutely isolated preparations; d) CA1 pyramidal neurones have been the focus of several studies of dendritic integration because of the large primary apical dendrite, from which dendritic patch-clamp recordings can be obtained routinely.

In fact, the electrophysiological studies on CA1 neurones were of the utmost importance as they have contributed to tremendous advances in understanding synaptic transmission, integration, and plasticity in the CNS. Thus, the CA1 subfield lends optimal conditions to study the effect of feeding cycle on the behaviour of ion channels present at the surface of rat hippocampal neurones.

6.3 References

Andersen P, Morris R, Amaral D, Bliss T & O`Keefe J (2007). *The Hippocampus Book*. Oxford University Press, Mew York.

Bannister N & Larkman AU (1995*a*). Dendritic Morphology of CAl Pyramidal Neurones From the Rat Hippocampus: 11. Spine Distributions. *J Comp Neurol* **360,** 161–171.

Bannister NJ & Larkman AU (1995*b*). Dendritic morphology of CA1 pyramidal neurones from the rat hippocampus: I. Branching patterns. *J Comp Neurol* **360,** 150–160.

Ishizuka N, Cowan WM & Amaral DG (1995). A quantitative analysis of the dendritic organization of pyramidal cells in the rat hippocampus. *J Comp Neurol* **362,** 17–45.

Newman EA, Araque A, Dubinsky JM, Swanson LW, King L & Himmel E (2017). *The Beautiful Brain. The Drawings of Santiago Ramón y Cajal*. Abrams.

Walther C (2002). Hippocampal terminology: Concepts, misconceptions, origins. *Endeavour* **26,** 41–44.

7 ANNEX II

7.1 Voltage clamp techniques

Much of what we know about the properties of ion channels in cell membranes has come from experiments using voltage clamp (VC). The method was first developed by Cole (Cole, K.S, 1949) and Hodgkin et al. (Hodgkin & Huxley, 1952*a*, 1952*b*) for use with the squid giant axon.

In a VC experiment, the membrane potential of a cell is controlled from an external device (the VC amplifier), with the goal of measuring the ionic currents that flow through the channels in the cell membrane at this given command potential. This requires an active compensation of the current flow across the membrane. The membrane potential is measured and compared to the command signal; the VC amplifier compensates by active charge injection the deviation to keep the error as small as possible. The quality of the current recording is mainly determined by this error signal. In summary, the method allows ion flow across a cell membrane to be measured as electric current, whilst the membrane voltage is held under experimental control with a feedback amplifier. The usefulness of the voltage clamp stems firstly from the fact that it allows the separation of membrane ionic (through open ion channels) and capacitive (charging of the membrane capacitance) currents; when the potential is held constant, there will be no capacity current and the ionic current will be the same as the total membrane current. A further advantage is that it prevents the regenerative potential response (the action potential) that is triggered by the activation of voltage-gated ion channels. Thus, it enables the currents responsible for the action potential to be investigated in a quantitative way.

Many variants of the VC technique have evolved since its advent, and voltage clamp analysis has been extended to a wide range of tissues.

This thesis encompassed VC methods that are used to measure currents from 1) whole cells or large areas of membrane containing at least a few hundred channels -macroscopic currents or whole-cell currents - and from 2) an isolated small patch of membrane containing just a few (ideally, one) ion channels – microscopic or single-channel currents.

7.1.1 Patch clamp configurations

Patch clamp recordings are the basis of modern electrophysiology, and their importance to related research fields cannot be underestimated. Patch clamp recordings are based on the use of blunt (as oppose to sharp microelectrodes used in intracellular recordings), fire polished microelectrodes that form a so-called “giga-seal” with the cell membrane. The invention of the giga-seal, and development of the various patch methods in the late 1970’s by Erwin Neher and Bert Sakmann (Neher & Sakmann, 1976) were rewarded with the Nobel Prize for Physiology or Medicine, in 1991, “for discoveries concerning the function of single ion channels in cells”. Their work revolutionized cellular biology and neuroscience and allowed the electrophysiologists to extend their knowledge on the underlying mechanisms of ion channels functioning.

Originally the term “patch clamp” referred to voltage clamp recordings of currents through individual ionic channels from an isolated patch of membrane. The principle of the technique is to electrically isolate a patch of membrane from the external solution and record current flowing into the patch. This is achieved by pressing the tip of a heat-polished pipette (with an opening of 1–3 µm, fire polished) onto a clean membrane. Once the tip of the electrode touches the cell membrane at the outer surface, a gentle negative pressure is applied to the electrode interior. This sucks the membrane tightly to the edges of the electrode tip, resulting in a very tight seal between pipette tip and membrane, with a resistance greater than 10GΩ, hence the term "giga-seal". This enables the recording of currents in the pA (10^{-12}A) or fA (10^{-15}A) range with low background noise. After giga-seal formation, it is now possible to record either currents from the entire cell using the whole-cell (WC) recording mode or single channel activity with cell- attached, inside-out or outside-out modes (Figure 7.1). WC voltage clamp and inside-out patch clamp are the configurations presently used in this thesis, whose fundamentals were fabulously described in a reference paper by Hamill, O. P. and co-workers (Hamill *et al.*, 1981). WC was applied to record Na^+ and Ca^{2+} currents, whilst inside-out patch clamp was used to record single-Na^+ channel activity.

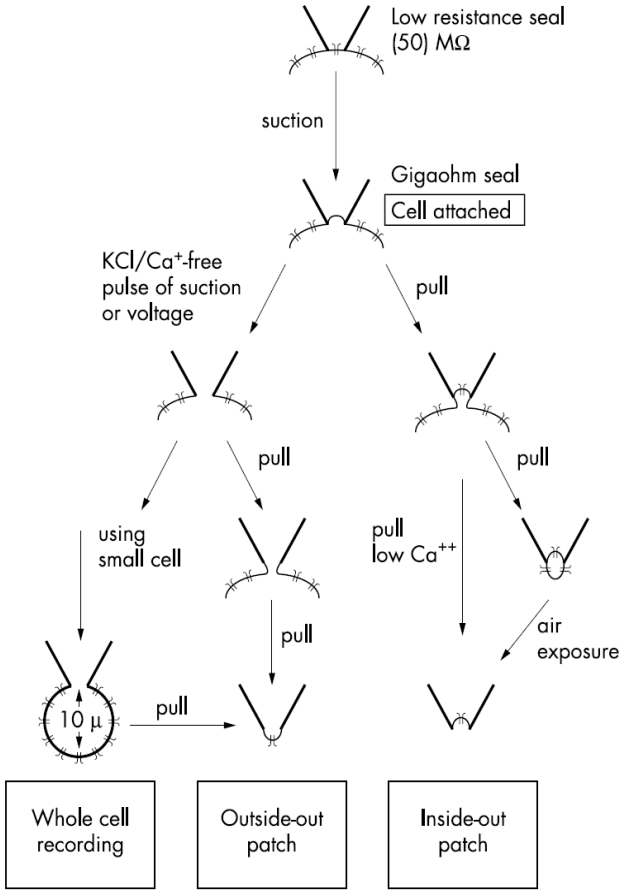

Figure 7.1- ***Schematic representation of the procedures for various recording configurations****. A fine tipped (about 0.5 to 5µm in tip diameter) glass patch electrode is used as a current monitor and the voltage in the pipette is held at a desired level. The first step in applying the technique is the formation of a high resistance seal between the patch electrode and the surface of the cell. Once the seal is established, several recording configurations are available to the investigator, and these fall into two broad categories. On the one hand, current flow through the patch of membrane under the electrode tip can be monitored, in which case single channel currents are usually recorded. Alternatively, for whole cell recording, the patch of membrane can be disrupted so that the electrode monitors current flow through the entire cell surface. Taken from (Lehmann-Horn & Jurkat-Rott, 2003)*

7.1.1.1 Whole-cell and inside-out patch clamp recordings – technical singularities and procedure

Upon formation of a giga seal (cell-attached configuration in figure 7.1), withdrawing the pipette from the cell (in a sharply upwards movement) results in an excised membrane patch with its cytoplasmic side exposed to the bath solution - *Inside-out patch configuration.* The likely formation of vesicles at the tip of the pipette upon this movement is prevented by the chelation of calcium ions in the bath solution (Hamill *et al.*, 1981). This configuration has the advantage of allowing the control of the transmembrane voltage (inverted in this case), as well as the access to the intracellular part of the channels. This is extremely important for the study of the influence of cytoplasmic constituents or second messengers on channel activity or address events that occur at the cytoplasm milieu of the channels (e.g., removal of fast inactivation by application of proteases) (Patlak & Horn, 1982; Horn & Vandenberg, 1984; Vandenberg

& Horn, 1984; Patlak, 1991). However, the lower structure stability of the excised patch (when compared to cell-attached patch), along with the loss of cytoplasmic constituents might impair the intrinsic behavior of ion channel proteins. Moreover, the signal-to-noise output is a major concern, as the currents are recorded in a pA range, instead the nA (1000-fold) obtained in WC (see Table 7.1). Hence, to attain a proper single channel recording with low noise levels, one needs to comply with a demanding setting up, whose laborious steps are described in the materials and methods section of chapter 3 (section 3.1.6).

Instead of withdrawing the patch pipette from the membrane after seal formation, application of gentle suction will disrupt the membrane patch directly under the pipette, leading to the formation of a low resistance (in the MΩ range) pathway between the cell interior and the solution in the pipette – *whole-cell (WC) configuration*. The interior of the cell and the solution of the pipette become contiguous and the currents passing through the entire cell membrane are recorded. This configuration is equivalent to intracellular recording with sharp microelectrodes and has the advantage that it can be applied to very tiny or flat cells that would be impossible to impale. However, because the cell interior is being perfused with pipette solution, this configuration has the disadvantage that certain cytosolic factors important for cellular function may be washed out.

Formation of the *WC configuration* becomes immediately apparent by the sudden appearance of large capacity transients at the beginning and end of the test pulse, which reflect the charging and discharging of the capacitance of the cell membrane. These transients can be minimized using the whole-cell capacitance (C_m) cancellation and series resistance (R_s) compensation dials on the patch-clamp amplifier. This allows a crude estimation of the cell capacitance (and hence cell size) to be made because cell membranes have a constant specific capacitance of $1\mu F/cm^2$. Smaller C_m and R_s values render better voltage clamping conditions, as the membrane reaches the steady-state voltage command potential rather faster.

Single-channel recordings, thus, have their own particularities when compared to WC. The most relevant differences are depicted in table 7.1, highlighting the conditions used in this work.

Table 7.1- Main technical differences between the two patch clamp configurations used in this study.

		Single-channel (inside-out) patch clamp	Whole-cell
Pipette	Tip diameter (µm)	1 to 2	2 to 3
	Rod length (cm)	~3	~5
	Shank Coating	Sylgard	-
	Resistance	13-25 MΩ	3-5 MΩ
	Outside/Inside diameter (mm)	1.5/0.86	1.5/1.05
	Capacitance	↓	↑
Seal resistance		>10GΩ	MΩ
Recording currents		pA (10^{-12}A); fA (10^{-15}A)	nA (10^{-9}A)

7.1.2 Principles of patch-clamp recording – technical instrumentation

The patch pipettes are mounted on a pipette holder that connects the Ag wire electrode (coated with AgCl), immersed into the pipette solution, directly to the headstage amplifier (Figure 7.2). Patch clamp amplifiers are based on a current-to-voltage (I/V) converter circuit, which transfers the pipette current into an equivalent output voltage. Therefore, they cannot measure membrane potentials directly. The key element in the patch clamp recording is the feedback amplifier in the headstage (Figure 7.2, inset).

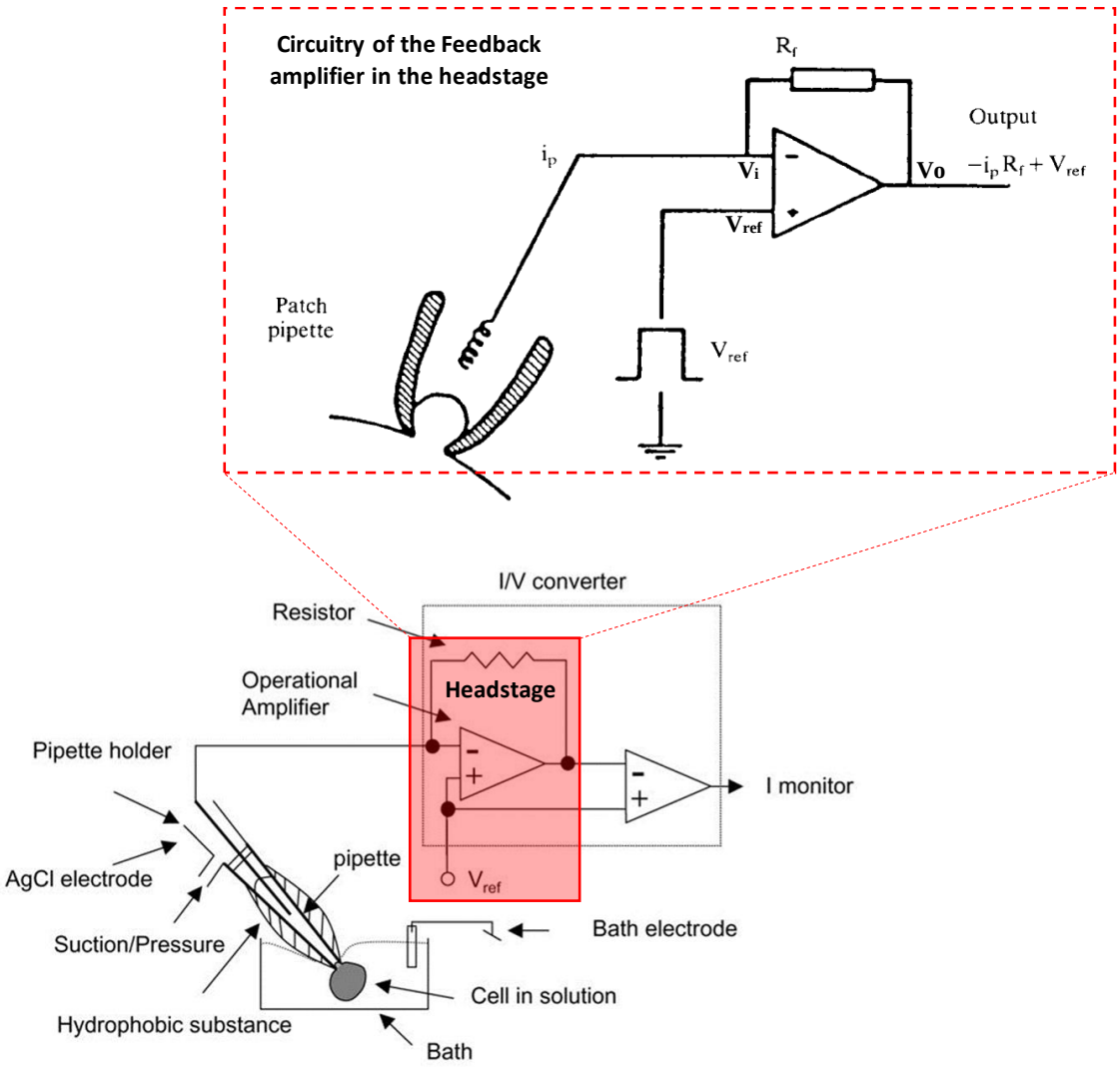

*Figure 7.2- **Patch clamping setup**. The pipette, coated with a hydrophobic substance to reduce the pipette capacitance, is attached to a pipette holder, which connects the pipette to the electronic circuitry by means of a silver chloride electrode. The inset highlights the schematic diagram of the headstage current/voltage amplifier circuitry. The gain (V_o/i_p, mV/pA) is set by the feedback resistor R_f to the input. This ensures that the input voltage Vi is kept nearly equal to the input voltage V_{ref}. Adapted from (Morgan & DeCoursey, 2007) and (Ogden & Stanfield, 1994).*

The feedback amplifier controls the membrane potential. Current flows from the output of the amplifier when the voltage of its two inputs is not equal. The amplifier receives two inputs: a positive input from a command potential output source of variable setting (V_{ref}), which is determined by the user, and a negative input from the pipette potential (V_p). When both inputs are at the same potential, the output will be zero. When a discrepancy arises between the two inputs, the amplifier strives to null this discrepancy and force V_p to equal V_{ref}. This is achieved by the amplifier passing current across the

feedback resistor, R_f, to drive the inside of the cell to the reference potential. This current supplied by the feedback amplifier is equal and opposite to the current carried by ions flowing across the membrane. The current flowing through the pipette (I_p) to clamp the cell membrane is proportional to the voltage drop (V_{out} - V_p) across the resistor, R_f, according to Ohm's law

$$-i_p R_f = V_{out} - V_{ref} \qquad \textit{(Equation 7.1)}$$

In practice, therefore, pipette current is monitored by a differential amplifier that constantly measures the difference between V_{ref} and V_{out}. This subtraction, which happens in a later stage on the circuitry, generates an output voltage that is purely proportional to the patch membrane current (recorded as opening and closures of individual channels). Thus, since the potential in the pipette is equal to V_{ref}, the patch membrane potential can be held in a steady state level or changed in stepwise fashion by changing V_{ref}. During recordings, pulses from a computer ($V_{command}$) were used to change V_{ref} in a stepwise way.

From *Equation 7.1*, it follows that the sensitivity of current measurement is inversely proportional to the size of the R_f, with a large resistor enabling measurement of smaller current amplitudes and lower background noise levels. For recording currents in the pA range, a high value feedback resistor R_f is needed (up to 50 GΩ). In the inside-out configuration presently used, another approach suitable for high-resolution recordings has been applied - the "capacitive feedback" technique (also called integrating headstage). Here, a capacitor replaces the feedback resistor and the headstage circuit becomes an integrator. This approach has a superior noise performance compared to the resistive feedback, as long as the input (stray) capacitance can be kept low (clearly below 10 pF). In the whole cell configuration, larger currents are needed (in the nA range), therefore, the feedback resistor is in the range of a few ten MΩ. Subsequently, the voltage drop across the pipette resistance cannot be ignored, and needs to be compensated electronically, by adjusting the R_s compensation dial on the electromer.

7.2 References

Hamill OP, Marty A, Neher E, Sakmann B & Sigworth FJ (1981). Improved patch-clamp techniques for high-resolution current recording from cells and cell-free membrane patches. *Pflugers Arch Eur J Physiol* **391,** 85–100.

Hodgkin AL & Huxley AF (1952*a*). A quantitative description of membrane current and its application to conduction and excitation in nerve. *J Physiol* **117,** 500–544.

Hodgkin AL & Huxley AF (1952*b*). Currents carried by sodium and potassium ions through the membrane of the giant axon of Loligo. *J Physiol* **116,** 449–472.

Hodgkin AL & Huxley AF (1952*c*). The dual effect of membrane potential on sodium cinductance in the giant axon of Loligo. *J Physiol* **116,** 497–506.

Hodgkin AL, Huxley AF & Katz B (1952). Measurement of current-voltage relations in the membrane of the giant axon of *Loligo*. *J Physiol* **116,** 424–448.

Hodgkin AL & Huxley A.F. (1952). The Components of Membrane Counductance in the Giant Axon of Loligo. *J Physiol* **116,** 473–496.

Horn R & Vandenberg CA (1984). Statistical properties of single sodium channels. *J Gen Physiol* **84,** 505–534.

Lehmann-Horn F & Jurkat-Rott K (2003). Nanotechnology for neuronal ion channels. *J Neurol Neurosurg Psychiatry* **74,** 1466–1475.

Morgan D & DeCoursey TE (2007). Analysis of electrophysiological properties and responses of neutrophils. In *Neutrophil Methods and Protocols. Methods in Molecular Biology*, ed. Quinn MT, DeLeo FR & Bokoch GM, pp. 139–175. Humana Press.

Neher E & Sakmann B (1976). Single-channel currents recorded from membrane of denervated frog muscle fibres. *Nature* **260,** 799–802.

Ogden D & Stanfield P (1994). Patch clamp techniques for single channel and whole-cell recording. In *Microelectrode techniques: the Plymouth Workshop handbook,*

Patlak J & Horn R (1982). Effect of N-bromoacetamide on single sodium channel currents in excised membrane patches. *J Gen Physiol* **79,** 333–351.

Vandenberg CA & Horn R (1984). Inactivation viewed through single sodium channels. *J Gen Physiol* **84,** 535–564.